SMALL ANGLE ELASTIC SCATTERING OF ELECTRONS BY NOBLE GAS ATOMS

René Wagenaar

55

Small Angle Elastic Scattering Of Electrons By Noble Gas Atoms

Cover design and printing by Ed van Uum:
'Electron trajectories in the field of an atom'.

Small Angle Elastic Scattering Of Electrons By Noble Gas Atoms

academisch proefschrift

ter verkrijging van de graad van doctor in de Wiskunde en Natuurwetenschappen aan de Universiteit van Amsterdam, op gezag van de Rector Magnificus, Dr. D.W. Bresters, hoogleraar in de Faculteit der Wiskunde en Natuurwetenschappen, in het openbaar te verdedigen in de Aula der Universiteit (tijdelijk Lutherse Kerk, ingang Singel 411, hoek Spui) op woensdag 15 februari 1984 des namiddags te 16.00 uur

door

René Wijnand Wagenaar
geboren te Amsterdam

Promotor : Prof.Dr. J. Los

Copromotor : Dr. F.J. de Heer

Aan

mijn ouders,

Henny,
Paula,
Carla,
Simone,
Saskia,
Amparo .....

Voorwoord

Een voorwoord is bij uitstek geschikt om potentiële lezers van enige achtergrond informatie omtrent de auteur te voorzien, alvorens zij zich wagen aan een tocht door de eigenlijke tekst. Dat die voor dit proefschrift wat ongebruikelijk lang is uitgevallen, hangt zeker samen met mijn stijl van schrijven (en praten), maar vindt zijn oorzaak ook in de aard van dit onderzoek. Immers, de grote precisie, waarmee de metingen uitgevoerd moesten worden, maakte het noodzakelijk alle relevante experimentele parameters zorgvuldig te calibreren. Dit, samen met een uitgebreide beschrijving van een nieuw type analysator, beslaat alleen al de helft van het proefschrift. Daarnaast achtte ik het instruktief om een overzicht van de bestaande theoretische modellen te geven, met de nadruk op hun eventuele tekortkomingen. Naar ik hoop, komen zij zodoende bij de presentatie van de meetresultaten minder uit de lucht vallen.

Terugblikkend moet ik konstateren dat het onderzoek niet zonder de nodige 'ups en downs' is verlopen. Het in principe eenvoudige experiment bleek in de praktijk veel moeilijker te realiseren dan aanvankelijk viel te voorzien. Het bedwingen van een deelproces in de natuur, zo hermetisch afgeschermd met een roestvrij-stalen konstruktie dat de vertwijfelde onderzoeker slechts kan gissen naar wat zich daarbinnen feitelijk afspeelt, vergt het uiterste aan geduld en inventiviteit. Meermalen wenste ik het apparaat met een spacelab missie de ruimte in te sturen, om aldaar in alle rust en vakuüm de elektronen in hun juiste koers te houden.

De beloning is evenwel groot, wanneer de natuur ten lange leste een deel van haar geheimen prijsgeeft. Helaas ben ik er door tijdnood niet in geslaagd een geheel sluitende interpretatie te vinden voor een nieuw verschijnsel in de waarnemingen. Maar het gegeven, dat dit fenomeen een voldoende basis vormt voor vervolg-onderzoek, stemt mij toch tevreden.

Dat een onderzoek als dit niet in kille afzondering wordt uitgevoerd, maar juist van alle kanten warme ondersteuning ondervindt, is een kompliment waard aan het adres van voor-

malig direkteur, Prof. Dr. J. Kistemaker. De wijze waarop hij het instituut heeft aangekleed, zowel wat instrumentarium als medewerkers betreft, valt beslist uniek te noemen. De open sfeer staat er borg voor dat je altijd snel de juiste man of vrouw vindt voor het oplossen van problemen en in feite met niemand blijvend overhoop ligt. Daar wil ik dan ook een ieder, die ik op het instituut van nabij heb gekend, voor bedanken.

Toch zou ik, zonder daarbij volledigheid na te streven, enkelen met name willen noemen. Allereerst is dat mijn promotor, Prof. Joop Los, voor wie ik gaandeweg diepe bewondering ben gaan koesteren. Met zijn scherpzinnigheid, gevoed uit een sterke fysische intuitie, wist hij mij telkens weer op het juiste spoor te zetten. Verder natuurlijk mijn groepsleider, Frits de Heer, die ondanks hardnekkige tegenslagen in de door mij gekozen aanpak bleef geloven. Jan Bannenberg, Evert de Haas en Ton Neuteboom droegen, puttend uit hun brede technische ervaring, vele waardevolle suggesties aan voor het ontwerp van de analysator. Met mijn twee naaste medewerkers, Lex de Boer en Ton van Tubergen, had ik het niet beter kunnen treffen. Lex verraste mij telkens weer met slimme technische oplossingen, terwijl Ton als student het apparaat op professionele wijze aan de komputer wist te koppelen. Dit geldt ook voor Wim Barsingerhorn, aan wie de konstruktie van de analysator was toevertrouwd. Het ogenschijnlijke gemak, waarmee hij de meest verfijnde klusjes geduldig opknapte, heeft grote indruk op mij gemaakt. Korte, maar krachtige technische steun verleende Arnold Bontekoe, terwijl Rob de Haan geruime tijd een belangrijke vinger in de elektronische pap heeft gehad.

Aan de afronding van het proefschrift hebben diskussies met Adriaan Tip in belangrijke mate bijgedragen, terwijl Frans Vitalis een onmisbare schakel vormde in de kontakten met de SARA-komputer. Ook heb ik nog kortstondig mogen profiteren van de steun van Wouter Koot, die zal trachten de komende jaren meer fysika uit dit apparaat te putten. Tenslotte heb ik volledig mogen vertrouwen op de deskundigheid van Tine van der Veer voor het typen, Hannah Smid voor de tekeningen, Frans Monterie voor het fotografische werk en Henk Sodenkamp voor het drukken. En op Roudy Grigoriou, die de

'hot line' tussen Apeldoorn en Amsterdam op de haar zo kenmerkende wijze verzorgde.

Op deze bedanklijst mogen ook zeker de heren Schiereck, Bok, Elsenaar en Meijers van Philips Data Systems niet ontbreken, voor de vrijheid die zij mij hebben verleend om het geheel tot een goed einde te brengen.

Een technisch-wetenschappelijke periode als deze mag dan een grote stempel op mijn leven hebben gedrukt, even zo belangrijk zijn de mensen geweest, die mij buiten de instituutspoort voor korte of langere tijd vergezeld hebben. Dit geldt zowel voor de vele vrienden, al dan niet verenigd in de 'filosofie-klub', als voor de diverse vriendinnen, aan wie ik dit proefschrift mede opdraag. Al wisselden de laatsten elkaar misschien wat frekwent af, één baken is altijd recht overeind gebleven, vooral bij het verzetten van het laatste lood, en wel mijn moeder. Voorwaar een unikum in een wereld, waarin opeenvolgende generaties elkaar steeds minder te vertellen hebben.

CONTENTS

The work described in this thesis is part of the research program of the Stichting voor Fundamenteel Onderzoek der Materie (Foundation for Fundamental Research on Matter) and was made possible by financial support from the Nederlandse Organisatie voor Zuiver-Wetenschappelijk Onderzoek (Netherlands Organization for the Advancement of Pure Research).

Parts of this thesis are based on the following publications:

Chapter II	: - H.J. Blaauw, R.W. Wagenaar, D.H. Barends and F.J. de Heer; J.Phys.B 13, 359 (1980). - R.W. Wagenaar and F.J. de Heer; J.Phys.B 13, 3855 (1980).
Chapter III	: R.W. Wagenaar, T. van Tubergen, A. de Boer and F.J. de Heer; to be published in J.Phys.E: Scientific Instruments.
Chapter IV	: R.W. Wagenaar, A. de Boer and F.J. de Heer; to be published in J.Phys.B: Atom.and Molec. Physics.
Chapter V	: R.W. Wagenaar and H. ter Riele; submitted for publication in Journ.of Comp.Physics.

Chapter I

General introduction

The main part of this thesis is devoted to the experimental study of elastic collisions of electrons with noble gas atoms, in particular small angle scattering.
As such, this thesis forms the conclusion of an extensive research program, which has been started about seven years ago, to test the validity of so-called forward dispersion relations for electron-atom scattering.

Historically, the term "dispersion relation" appeared first through the relation between the real part and the imaginary part of the complex index of refraction $n(\omega)$ in light optics. The real part represents the physical index of refraction $n_r(\omega)$ whereas the imaginary part is related to the absorption coefficient $\alpha(\omega)$:

$$n(\omega) = n_r(\omega) + i\,\frac{c}{2\omega}\,\alpha(\omega)\,, \tag{1.1}$$

ω being the frequency of the light. It is known from classical electromagnetic theory that $n_r(\omega)$ and $\alpha(\omega)$ are related through

$$n_r(\omega) = 1 + \frac{c}{\pi}\, P\int_0^\infty d\omega'\,\frac{\alpha(\omega')}{\omega'^2-\omega^2}\,, \tag{1.2a}$$

where $P\int$ is the principle value integral†. By formally defining $n(-\omega) = n^*(\omega)$, where the star denotes complex conjugation, one can rewrite (1.2a) as

$$\mathrm{Re}[n(\omega)-1] = \frac{1}{\pi}\, P\int_{-\infty}^{\infty} d\omega'\,\frac{\mathrm{Im}[n(\omega')-1]}{\omega'-\omega} \tag{1.2b}$$

†The principle value integral is defined as the limiting process:

$$P\int_0^\infty \frac{f(x')}{x'-a}\,dx' \equiv \lim_{\varepsilon\to 0}\left\{\int_0^{a-\varepsilon} + \int_{a+\varepsilon}^{\infty}\right\}\frac{f(x')}{x'-a}\,dx'$$

The term "dispersion relation" is clear since eq. (1.2b) concerns the frequency dependent index of refraction, which gives rise to the dispersion of light.

Crucial in our discussion will be the fact that one arrives at exactly the same relation as eq. (1.2b) by just applying Cauchy's theorem to the function

$$\frac{n(\omega') - 1}{\omega' - \omega} ,$$

along a closed contour in the complex ω' upper half-plane enclosing the pole $\omega' = \omega$. The necessary conditions for this contour integration to be justified are that $n(\omega)$ is analytic everywhere outside the real ω'-axis and that it is bounded as $|\omega'| \to \infty$. Kramers has shown that the analytic properties of $n(\omega)$ follow from the "causality-condition", in this context formulated roughly as: the medium cannot respond to the incoming light prior to the actual arrival of the light beam at its boundary surface [1,2]. In a somewhat modified form eq. (1.2b) has become known as the Kramers-Kronig dispersion relation. Thus, even without a detailed knowledge of the electromagnetic interactions involved, one can relate two - for the description of the scattering process relevant - observables with each other.

According to Titchmarch's theorem [3] a similar mathematical expression as eq. (1.2b) can be given for any function, like $n(\omega)$, which is analytic and bounded in its complex continuated variable. This theorem found wide application in elementary particle and nuclear physics, where one encountered large difficulties in revealing the specific character of the interactions in a collision. Therefore, theoreticians needed mathematical techniques which would make it possible - starting from general assumptions as to strength, range and other characteristics of the interaction - to derive relations between measurable quantities. Instead of in the index of refraction for light scattering, all information concerning the processes, which occur between two colliding (sub)atomic particles, is contained in the scattering amplitude. It is natural to investigate whether this amplitude can figure in the above sense as "dispersing function". The resulting dispersion relations have proven a valuable tool in the domain of relativistic quantum field theory [4].

Supported by this encouraging result, Gerjuoy and Krall [5] inferred that dispersion relations should also work in atomic physics. The most appropriate candidate for a first test is forward electron-atom scattering. An extra complication is formed here by the indistinguishability of the incident and atomic electrons. Electrons obey Fermi-Dirac statistics and thus the scattering amplitude decomposes in a "direct" part, where the incoming and scattered particle are the same, and an "exchange" part, where a rearrangement has been taken place between the projectile electron and one of the target atom electrons. These two amplitudes are usually denoted by f and g respectively. Both parts should obey now the above mentioned conditions with respect to analyticity, boundedness and high energy behaviour. Merely on plausibility grounds, Gerjuoy and Krall derived the following expression, which relates the real and imaginary part of the forward elastic scattering amplitude $f(E,0)$ for electron scattering from atoms in the ground state:

$$\mathrm{Re} f(E,0) = f_B - g_B(E) + \frac{1}{\pi} P \int_0^\infty \frac{\mathrm{Im} f(E',0)}{E' - E} dE' + \sum_{i=1}^{N} \frac{d_i}{|E_i| + E} . \tag{1.3}$$

This equation contains $f_B - g_B(E)$, the first Born approximation for the direct and exchange amplitude. The last term at the right-hand side accounts for the possible bound states that are formed by the electron and the neutral atom. These create singularities in the amplitude and as such contribute to the contour integral with a residue d_i at the formation threshold E_i. Given accurate wave functions for the target atom, these residues - if they are present - can be calculated, just as $f_B - g_B(E)$.

The key question as to the validity of eq. (1.3) can be tackled in principle along two lines; from the theoretical side, since the interactions involved are known, as well as from experiment.

The input from experiment becomes clear with the help of the well-known optical theorem. For, according to this theorem, the imaginary part of the scattering amplitude is given by:

$$\mathrm{Im} f(E,0) = \frac{k}{4\pi}\, \sigma_t(E), \tag{1.4}$$

where k is the wave number of the incident electron and $\sigma_t(E)$ the total cross section for scattering of electrons with energy $E = \frac{1}{2} k^2$ (in atomic units).

Then the real part can be evaluated up to its sign with the help of eq. (1.4) according to:

$$\sigma(E,0) = [\mathrm{Re} f(E,0)]^2 + [\mathrm{Im} f(E,0)]^2 \;, \tag{1.5}$$

where $\sigma(E,0)$ is the differential cross section for elastic scattering at 0°. The sign of Ref(E,0) can be fixed by theoretical considerations. Inserting eq. (1.4) in (1.3) leads to

$$\mathrm{Re} f(E,0) = f_B - g_B(E) + \frac{k}{4\pi^2}\, P \int_0^\infty \frac{\sigma_t(E')}{E' - E}\, dE' + \sum_{i=1}^{N} \frac{d_i}{|E_i| + E} \;. \tag{1.6}$$

So, by measuring total cross sections over a broad energy range, at least up to impact energies over which the first Born approximation yields the correct σ_t values, and differential elastic cross sections at angles as small as possible, relation (1.3) can be tested.

Let us first investigate whether collision theory is able to answer the key question satisfactorily.

Although the Schrödinger equation for the full electron-atom wave function is written down in a simple manner, its exact solution remains beyond one's reach even for the simplest system of an electron scattered off a hydrogen atom. Therefore, approximation methods have to be developed. Clearly, the interaction of an electron with an atom involves elastic scattering, excitation and ionization. At sufficiently high energies, where the momentum of the incoming electron is much larger than of the outer electrons of the target, it may be possible to treat these processes independently, as in the first Born approximation. In the intermediate and low energy range (i.e. $< \approx 100$ eV) however, these processes are correlated. For example, the possibility of ionization affects the cross section for elastic scattering through the unitarity relation (i.e. conservation of flux). Besides, the exchange mechanism plays an important role in this collision regime.

So, for a correct description of the elastic scattering amplitude, one has to account for coupling of the elastic channel with the inelastic channels including the continuum.

To treat this exactly is of course a formidable - not to say an impossible - task, largely exceeding the available computer capacities, but a great deal of experience has been gained now with some approximation procedures (see for instance [6]). From these we mention the close coupling method, where one calculates the coupling with only the first three to five inelastic channels exactly and the coupling with the remaining channels by replacing them with suitably chosen pseudo channels. Another is the optical model formalism, in which the projection of the full amplitude, containing all the inelastic channels and the continuum, on the ground state wave function is approximated. With the increasing size and speed of modern computers and improved programming techniques, these methods are capable now in yielding fairly accurate elastic differential cross section data over most of the angular range in this energy regime.

Yet, for our purposes, where we are interested in cross section data for small angle elastic scattering, one has to be cautious. For, the above mentioned numerical results are obtained within the partial-wave formalism, where the full scattering amplitude is given in terms of a summation over an - in principle - infinite series of orbital quantum numbers ℓ:

$$f(E,\theta) = \sum_{\ell=0}^{\infty} f_\ell(E,\theta) \qquad (1.7)$$

Here the f_ℓ are connected to the phase shifts η_ℓ according to:

$$f_\ell(E,\theta) = \frac{1}{k}\,(2\ell+1)\,e^{i\eta_\ell(k)}\sin\eta_\ell(k)\,P_\ell(\cos\theta). \qquad (1.8)$$

Usually, this summation is carried out exactly up to a certain value $\ell = N$, whereas the rest series is calculated with the effective range formula for the higher η_ℓ [7]:

$$\eta_\ell(k) \approx \frac{\pi\,\alpha_o\,k^2}{(2\ell-1)(2\ell+1)(2\ell+3)} \tag{1.9}$$

with α_o being the dipole polarizability of the target atom.

The reason for the appearance of this quantity α_o at larger ℓ values in the phase shifts becomes clear if one considers the collision within a semi-classical picture. In that case the orbital quantum number ℓ is simply related to the impact parameter b according to:

$$\ell = kb\ . \tag{1.10}$$

Although a trajectory description is not valid at low and intermediate k values (i.e. relatively large wavelengths for the projectile electron) and relation (1.10) as such loses its meaning, yet the statement that large ℓ values correspond with distant collisions, still holds. Since small angle electron scattering corresponds with distant collisions where - in the elastic case - the induced polarization plays the dominant role due to its long range, the quantity α_o enters eq. (1.9).

However, there is no clear insight yet as to how large N has to be taken as a function of the impact energy. This critically depends upon the range and strength of the effective potentials taken for the absorptive (excitation and ionization) and exchange part of the electron-atom interaction. It appears from current research [8], that these two processes contribute to terms in the series expansion of eq. (1.7) with much higher N values than previously assumed, particularly in the neighbourhood of the inelastic thresholds.

It is therefore by no way surprising that the most refined cross-section calculations still deviate from each other in the forward direction.

Despite of this "cut-off" problem, eq. (1.9) as it stands has to be amended. For it assumes the collision to take place adiabatically, i.e. the electron cloud can adjust itself instantaneously to the position of the scattering electron, leading to a static dipole polarization of the atom. Actually, the target cloud response will not be of a pure dipole character and besides it will show some dependence on the velocity of the projectile electron. So the static dipole polarizability α_o should at least be replaced by an impact energy dependent factor $\alpha(E)$, to which also higher multipoles contribute. This too has stimulated more theoretical research [9,10].

In comparison with elastic scattering, the theoretical treatment of excitation and ionization presents even larger difficulties. The still poor state of the art in calculating total cross sections reflects this clearly; for, above threshold, also accurate inelastic cross sections are needed. Only at high collision energies (i.e. $> \approx 200$ eV) most methods, of which we mention the Eikonal Born Series (E.B.S.) expansion [11] and the optical model [12], succeed in producing reliable data.

The preceding survey intentionally has been given in some detail, in order to convince the reader that from the theoretical front a reliable quantitative analysis on the validity of the forward dispersion relation cannot (yet) be expected.
Therefore, the necessary material should be supplied by experiment.

At the time the forward dispersion relation was written down, the necessary experimental data were either completely lacking or not accurate enough. At the end of the sixties Bransden and McDowell [13] started a thorough theoretical investigation on the existing data. They intended to use the dispersion relation to check their consistency. However, their study casted doubt upon the correctness of formula (1.3) as proposed by Gerjuoy and Krall. Owing to the lack of accuracy of the data, they were not able to make a decisive statement.

In the mid-seventies, some theoreticians [14,15,16,17] tried to evaluate more critically the basic assumptions Gerjuoy and Krall made with respect to their derivation of relation (1.3). They focused their study on the analyticity properties of the scattering amplitude. Even in the simplest case of electron-hydrogen scattering, their findings concerning its singularity structure are contradictory. However, they all agree that Gerjuoy and Krall were wrong in assigning the same singularity branch to the exchange amplitude as to the direct part. In particular Tip [15] could show, applying the recently developed complex dilatation formalism [18], that the exchange part is ~~not~~ necessarily regular along the negative real energy axis. Tip's conclusions have been confirmed by Amusya and Kuchiev [16] and recently also by Dumbrajs and Martinis [19], who explored the problem on the basis of relativistic dispersion theory, using Feynman diagrams.

Therefore, relation (1.3) should be supplemented at the right-hand side by a discrepancy function $\Delta(E)$, which represents the contribution of a cut along the negative real energy axis:

$$\mathrm{Re}f(E,0) = f_B - g_B(E) + \frac{1}{\pi}P\int_0^\infty \frac{\mathrm{Im}f(E',0)}{E'-E}\,dE' + \sum_{i=1}^{N} \frac{d_i}{|E_i| + E} + \Delta(E) \quad . \tag{1.11}$$

That this $\Delta(E)$ must be ascribed completely to exchange, could be confirmed by a numerical analysis, first carried out by Bransden and Hutt [20] and later refined by us [21], with the existing data on electron and positron-atom scattering. For, positrons do not exhibit any exchange-like features and indeed in that case $\Delta(E)$ appears to vanish, a result also obtained from Tip's study.

Because the location and order of additional singularities in the exchange amplitude are not yet well established, it is hard to predict the magnitude and shape of $\Delta(E)$. Only recently, Dumbrajs and Martinis [19] did a first attempt for electron-hydrogen scattering. Their results deviate substantially at intermediate energies from the values we deduced numerically.

Therefore they stress the need for a new unambiguous determination of the real part of the amplitude in that collision energy range.

We decided to carry out an experiment, in which total as well as small angle elastic differential cross sections could be measured absolutely with high accuracy, and thus check the validity of the dispersion relation.

Total cross sections were derived by measuring the attenuation of the primary beam when it passes through a collision chamber filled with gas of a well-defined density. The results of these measurements and their use in evaluating the right-hand side of relation (1.6) have been discussed in the thesis of Blaauw [22]. The experimental set-up used for this purpose, together with a few improvements in order to refine some previously obtained data, will be described in the first part of Chapter II.

Small angle elastic scattering measurements set high demands on the beam focusing in order to prevent mixing of the scattered electrons with the tails of the primary beam. Besides, the beam should be stable over the whole period needed for an angular scan. In particular at intermediate and low impact energies, this is a hard experimental task and in fact the main reason for the lack of data in this regime.

In order to explore this area, we completely modified the way in which differential scattering experiments are usually performed.

First, we installed a collision cell of adjustable length. By making this very small the collisions are confined in space such that their scattering angle becomes well-defined. In that case the set-up resembles more a crossed beam, but with the advantage of a well reproducible density. A determination of the effective interaction length for such a small cell size was necessary in order to put the data on an absolute scale. This could easily be done with the previously obtained total cross section data. The gas density profile has been simulated with a versatile computer program, which we developed starting from some basic assumptions with respect to molecular effusive flow. The comparison of these two forms the subject of the second part of Chapter II.

Secondly, a novel design of a parallel-plate analyser in combination with a multichannel particle detector was tested at impact energies where also other groups had obtained small angle data. The intensity distribution of the scattered electrons in the small angular range of interest to us, can be measured simultaneously with this set-up. Its design and principles of operation will be described extensively in Chapter III.

Chapter IV deals with the measurement procedure for differential elastic scattering and presents the absolute data we found for the noble gases. These data throw some light on both the exchange and polarization mechanism and serve as an excellent probe for the accuracy of the various theories. An interesting feature is revealed around the ionization energies for helium and neon: we observed a decrease in flux in the elastic channel towards smaller angles, when the impact energy was scanned over the respective thresholds. A speculative view will be given on the processes, which may be responsible for the appearance of this structure.

Finally, chapter V is devoted to the forward dispersion relation for electron-helium elastic scattering. With the accurately measured small angle differential and total cross section data we are able to establish firmly the shape and magnitude of the discrepancy function. A sophisticated numerical technique is applied on this function in order to extract from it more specific information about the exchange amplitude.

References

[1] See Roman P, Advanced Quantum Theory, Ch.III, Reading, Addison-Wesley (1965).

[2] Hilgevoord J, Dispersion Relations and Causal Descriptions (Thesis), North-Holland Publ.Co. (1960).

[3] Titchmarch E C, Theory of Fourier Integrals, Oxford, The Clarendon Press (1948).

[4] Goldberger M L, Introduction to the Theory and Applications of Dispersion Relations, Ch.I and II in "Dispersion relations and elementary particles", New York, Wiley and Sons (1960).

[5] Gerjuoy E and Krall N A, Phys.Rev. 119, 705 (1960) and Gerjuoy E and Krall N A, Phys.Rev. 127, 2105 (1962).

[6] Callaway J, Adv.in Phys. 29, 771 (1980) and references therein.

[7] O'Malley T F, Rosenberg L and Spruch L, Phys.Rev. 125, 1300 (1962).

[8] Van de Ree J, J.Phys.B: Atom.and Molec.Phys. 15, 2245 (1982).

[9] Truhlar D G, Rice J K, Trajmar S and Cartwright D C, Chem.Phys.Lett. 9, 299 (1971).

[10] McCarthy I E, Saha B C and Stelbovics A T, Phys.Rev. A25, 268 (1982).

[11] Byron F W and Joachain C J, J.Phys.B: Atom.and Molec.Phys. 10, 207 (1977).

[12] Byron F W and Joachain C J, Phys.Rev. A15, 128 (1977).

[13] Bransden B H and McDowell M R C, J.Phys.B: Atom.and Molec.Phys. 2, 1187 (1969) and 3, 29 (1970).

[14] Gerjuoy E and Lee C M, J.Phys.B: Atom.and Molec.Phys. 11, 1137 (1978).

[15] Tip A, J.Phys.B: Atom.and Molec.Phys. 10, L11 and L295 (1977).

[16] Kuchiev M Yu and Amusia M Ya, Phys.Lett. A66, 195 (1978).

[17] Byron F W and Joachain C J, J.Phys.B: Atom.and Molec.Phys. 11, 2533 (1978).

[18] Combes J M and Tip A, CNRS preprint (1983).

[19] Dumbrajs O and Martinis M, J.Phys.B: Atom.and Molec.Phys. 15, 961 (1982).

[20] Bransden B H and Hutt P K, J.Phys.B: Atom.and Molec.Phys. 8, 603 (1975).

[21] Wagenaar R W, FOM Report nr. 43.948 (unpublished).

[22] Blaauw H J, On the forward dispersion relation for electron-atom scattering (Thesis), Amsterdam (1979).

CHAPTER II

Total cross sections for electron scattering from noble gas atoms

Abstract

Total cross sections have been measured for electron scattering from the noble gases, claiming an accuracy of better than 5% and performed under very well defined conditions of angular and energy resolution. The apparatus yielded systematically higher data than most other experiments; the explanation must be found in a more complete screening against forward scattering in our set-up than achieved by others. Our previous measurements for the heavier noble gases were repeated in a short collision cell of adjustable length, which admitted the use of higher target pressures. Because of the influence of effusion through the cell apertures, an experimental test had to be carried out on the effective gas density as a function of the cell length. This is also of critical importance later on for putting the differential cross section measurements on an absolute scale. It appeared that the experimental values at small collision lengths could not be reproduced with an effusive molecular flow model, based on diffusive reflection from the cell walls.

1. Introduction

In the preceding introductory chapter we arrived at the conclusion that, for a reliable quantitative analysis of the forward dispersion relation for electron-atom scattering, both accurate total and differential elastic cross sections at small angles should be supplied by experiment.

With regard to total cross section measurements, a lot of experiments have been carried out in an earlier period (1925 - 1970) as one can learn from the review article of Bederson and Kieffer [1]. Generally, such an experiment consists of measuring the attenuation of the primary electron beam after passage through a collision chamber of a well-defined effective absorption length. Most of the previous experiments have been performed with the Ramsauer [2] technique, where the electron beam is energy selected with the aid of a magnetic field perpendicular to the orbit plane. Although Ramsauer's design is basically simple and elegant, it is difficult to control the spatial extension of the electron beam in such an arrangement. An unknown fraction of the scattered electrons may thus be registered in the detector; in particular at high impact energies this "scattering-in" effect can cause a considerable reduction in the measured absorption. Only a few decades later Golden and Bandel [3] and recently Dalba et al. [4] could largely remove this serious shortcoming.

In their review Bederson and Kieffer [1] ended up with the conclusion that, for instance in the case of helium, the existing data had an accuracy of at most 25% in the energy range up to 30 eV, whereas at higher energies the consistency was even worse. Therefore we (Blaauw [5]) designed an apparatus, with which these data could be measured absolutely in the energy range of 20 - 750 eV. The noble gases and some diatomic molecules were used as targets. The results of these measurements, together with a description of the apparatus, have been published in three separate articles: Blaauw et al. [6] for He and N_2, Wagenaar and de Heer [7] for Ne, Ar, Kr and Xe and van Wingerden et al. [8] for H_2. At about the same time around 1976 as we initiated the present study, also other groups started experiments to obtain accurate data. They needed these as calibration standards for other measurements, for energy transfer calculations in the upper atmosphere or plasmas, or to compare with positron-atom collision studies. Except Dalba et al. [4], all these groups applied, just as we did, quite different techniques compared with Ramsauer's early design. At low energies (up to 12 eV) Milloy and Crompton [9] carried out a diffusion experiment with a swarm technique, yielding momentum transfer cross sections, which could then be transformed into total cross sections with high accuracy. For the low and intermediate energy range Kennerly and Bonham [10] developed a nice technique. They recorded a time of flight spectrum with a pulsed electron beam, from which total cross sections could be derived simultaneously for all impact energies below 50 eV. Kauppila and coworkers [11,12,13,14] performed both accurate total cross section measurements for electrons as well as for positrons over the broad energy range of a few eV up to $\approx$500 eV in order to reveal typical energy dependent differences between these two projectiles. Their machine employs a longitudinal magnetic field for impact energy selection in combination with a retarding field element as particle detector.

For helium, neon and molecular hydrogen we found - in the overlapping energy ranges - agreement with these recent data, amply within the combined error bars, typically 5 - 10%. As a result, a much more satisfactory situation does exist now; the attained accuracy was largely sufficient for calculating the principle value integral in the dispersion relation (1.6), as one can learn from Blaauw [5]. The data confirmed the excellency of the various recently refined theoretical calculations of total cross sections below the inelastic threshold for these gases. From these we mention the matrix variational method of Nesbet [15] and the R-matrix calculations of Fon et al. [16]. However, the various theoretical results at high impact energies (i.e. $> \approx 100$ eV) - most of them based on the second Born approximation [17,18] or the optical model [19] - are less accurate; they converge only slowly to the experimental data with increasing impact energy.

For argon, krypton and xenon some deviation was found from the results of Kauppila's group [13]. This discrepancy could be ascribed for the most part to the imperfect screening against small angle scattering in their set-up. After correction for this, we still disagreed significantly with them at impact energies below ≈ 70 eV. Therefore we had to look for a possible systematic error in our measurements. The only possible one could be the uncertainty in the calibration of the pressure sensing head, which becomes critical at low target pressures. Since the scattering cross sections for the heavier noble gases are much larger than for helium and neon, in particular at the lower impact energies, and large absorption rations where multiple collisions become important have to be avoided, only small target pressures could be admitted in the 42 mm collision cell which we used for the published measurements. We decided to remeasure these cross sections with the collision chamber of adjustable length, which we needed for the differential scattering measurements. Its short length (2 - 10 mm) enabled us to apply larger pressures, typically in the order of 1 Pa, and thus made the baratron reading less sensitive to possible zero-shifts or calibration errors. It appeared that we indeed had to modify some of the former total cross section data [7] for these gases below 70 eV. On the other hand, the previous data for He, Ne, N_2 and H_2 could all be reproduced within 2 - 4%.

Having established definitive total cross section data, we could use them as calibration standards for the determination of the interaction length of the adjustable collision chamber. For, as this cell is shortened, the density and profile of the target gas will be influenced more and more by the effusive flow of the atoms and molecules through the entrance and exit orifices in the cell. These apertures are needed in order to let the primary and scattered beam pass. Since we wanted to measure absolute differential cross sections with the cell adjusted to 2 mm, the effective product of density and collision length should be known exactly.

Besides the determination of the effective absorption length, we were also interested in the density profile itself. Since this is hard to assess experimentally, we set up a versatile computer simulation. The program is constructed along the same principles as suggested by Mathur et al. [29] to calculate the steady state condition for effusive molecular flow. All kinds of combinations for the dimensions of the cell, its length and the orifice diameters could be used as input. Besides the density profile, it also gave the effective interaction length, which could be compared with the values we found experimentally. As such it served as a check on the correctness of the simulated profile.

The scheme of this chapter is as follows. Section 2 deals with a description of the apparatus as used for the total cross section measurements. Therein we discuss in detail the scattering geometry, and the electron gun, since it has been used without essential modifications for the differential measurements, too. Construction details of the collision cell with adjustable length will also be given. In section 3 we treat the experimental procedure for obtaining total cross sections, both with the original set-up, consisting of the 42 mm long collision chamber with the retarding field analyser as beam detector, as well as with the adjustable cell in combination with a small Faraday cage behind it as current collector. Section 4 presents the revised total cross section data for Ar, Kr and Xe, together with a discussion of the results obtained by other groups. Section 5 deals with the exact experimental determination of the product of collision length and effective gas density for the shorter cell. These findings will then be compared with the values we found from our computer simulation.

2. Apparatus for total cross section measurements

2.1. General description

The experiment is basically a linearization of the Ramsauer technique; unlike this technique, there is no magnetic field present. This modification enables one to fix the scattering geometry unambiguously, so the angular resolution can be defined exactly. Moreover, this set-up permits differential scattering measurements. We shall treat the original set-up first; the insertion of the adjustable collision chamber puts only minor modifications on the present discussion. These will be considered in section 2.4.

A schematic drawing of the apparatus is shown in figure 1.

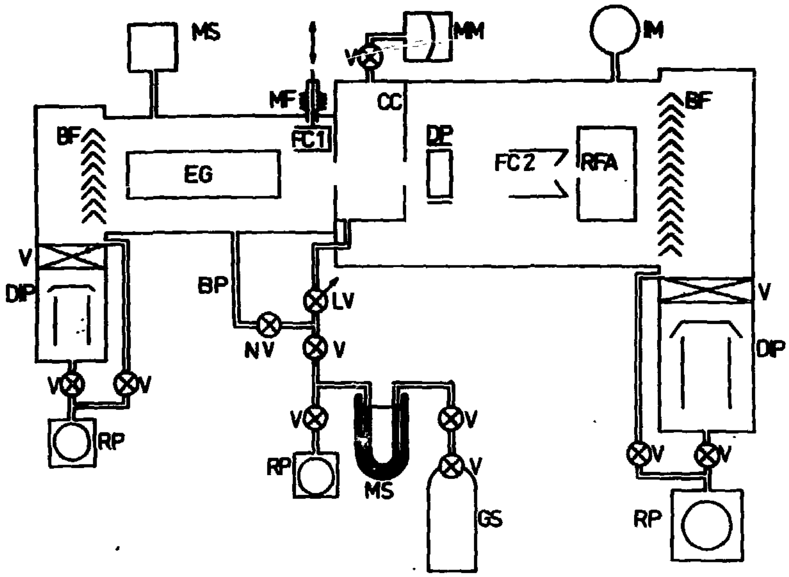

FIGURE 1

Basic scheme of the apparatus.
(Beam system) EG : electron gun, CC : collision chamber, DP : deflection plates, RFA : retarding field analyser, FC 1 and 2 : Faraday cups;
(Vacuum system) V : valve, LV : piezoelectric leak valve, RP : roots pump, DIP : oil diffusion pump, MS : molecular sieve, BF : liquid air cooled baffle, TM : thermocouple manometer, IM : ionization manometer, MM : membrane manometer, MS : mass spectrometer, GS : gas supply, BP : by-pass, NV : needle-valve.

An electron gun (EG) produces a highly parallel beam with impact energies variable between 20 and 800 eV and a thermal energy spread of 0.35 eV. This beam is led through a collision cell (CC) of length 42 mm and diameter 80 mm with entrance and exit orifices of Ø 1 mm. The detection takes place in a retarding field analyser (RFA) at 100 mm behind the centre of the collision chamber or by a Faraday cup (FC2) just in front of the analyser. This Faraday cup has a small hole in its back to let the beam pass through in the case of measurements with the analyser. Deflection plates behind the collision chamber ensure optimal collection in both detection modes. To control the variation of the electron beam properties during the measurements another Faraday cup (FC1) just in front of the cell can be moved downwards to intercept the primary beam. The cups are connected with Keithley 610 A current meters, which are read out digitally. Under vacuum conditions we have complete transmission of the electrons through the collision chamber.

After shielding the earth's magnetic field with two concentric mu-metal cylinders around the gun and analyser, the residual field is maximally 2 mG along the axis and 0.5 mG perpendicular to it.

The vacuum system has been designed in such a way, that (i) scattering taking place outside the absorption cell and (ii) scattering by other atoms or molecules than those of the target gas does not influence the signal more than a few tenths of a percent. The collision cell constitutes the separation between two pumping systems which are equal in construction. With oil diffusion pumps (2000 l/s at the analyser side and 700 l/s at the gun side) in this differential pumping set-up the background at the analyser side was less than 10^{-6} Pa and on the gun side less than 10^{-5} Pa. We found a pressure drop over the exit aperture of the collision cell of about 5000. The target gas is admitted to the cell through a piezoelectric precision leak valve and its pressure measured with a membrane manometer. The gas inlet system, as well as the gun and analyser are bakable to about 150°. Contamination of the admitted gas was checked by comparing the impurity concentrations with a mass spectrometer before and during inlet of gas.

By means of a needle valve (NV2) in the electron gun region we can simulate the same pressure and composition as there will be by flow through the orifices of the collision chamber when we lead gas into it. In this way we avoid variations of the primary beam during the measurements, caused by the sensitivity of the indirectly heated oxide cathode for pressure changes; in particular for H_2 this effect can produce serious errors (mainly by water formation at the cathode).

2.2. Scattering geometry

The scattering geometry is defined by the aperture of RFA (Ø 1 mm) or by FC2 (Ø 5 mm). This leads to a well defined solid angle of the analyser/collector: as seen from the centre of the collision chamber these values are $7.85 * 10^{-5}$ sr for the RFA and $3 * 10^{-3}$ sr for FC2.

To illustrate the advantage concerning the angular resolution, we shall analyse the relation between the total cross section and the attenuation of the beam in somewhat more detail. Basically this relation is the Lambert-Beer law:

$$\sigma_{tot} = (NL)^{-1} \ln(I_o/I_c) \tag{2.1}$$

where N stands for the gas density in the cell, L is the effective length of the electron path through the gas and I_o/I_c is the ratio of the beam intensity in front of and behind the absorption cell respectively. However, eq. (2.1) represents the ideal case, in which the beam is infinitesimally narrow and the solid angle of the detector is zero. Of course, this situation is not feasible in practice and small angle scattering must be incorporated. In the same way as eq. (2.1) is derived, one finds:

$$\ln(I_o/I_c) = NL\sigma_{tot} - N \int_o^L dx \int_o^{\Delta\Omega(x)} \frac{d\sigma}{d\Omega} d\Omega \ . \tag{2.2}$$

Here $\Delta\Omega(x)$ is the solid angle of the detector as seen by a scattering event taking place at position x on the beam axis.

The factor ($d\sigma/d\Omega$) represents (depending on the kind of detector) the elastic or elastic plus inelastic differential cross section. In many previous experiments (see Bederson and Kieffer [1]) lack of sufficient attention to this effect has led to signals in the detector which were too large, in particular at the higher impact energies where the scattering is peaked more in the forward direction. Using eq. (2.1), this resulted in total cross sections which were too low. It is therefore essential to create experimental conditions, under which the second term on the right-hand side of eq. (2.2) is kept small with respect to the first term.

For intermediate and high electron energies (i.e. $> \approx 35$ eV) we used the retarding field analyser (RFA) with its small solid angle; at low energies (i.e. $< \approx 40$ eV) FC2 was used with its relatively large solid angle, because under vacuum conditions in the collision chamber we were not able to tune the primary beam completely into the 1 mm Ø entrance aperture of the analyser at these energies. Fortunately, the scattering pattern turns out to be such that in both modes of operation the second term is relatively small. In the case of measurements with the RFA at higher energies, this can be demonstrated with a qualitative estimate of the magnitude of the integral expression in eq. (2.2) according to:

$$\int_0^L dx \int_0^{\Delta\Omega(x)} \frac{d\sigma}{d\Omega}\, d\Omega < L\ \Delta\Omega \left(\frac{d\sigma}{d\Omega}\right)_{elastic} (\theta = 0°)\ , \qquad (2.3)$$

where $\Delta\Omega$ stands for the solid angle subtended by the detector entrance aperture with respect to the centre of the collision cell. The cross sections at zero angle can be obtained by extrapolating the optical model calculations of Joachain et al. [19] and of McCarthy et al. [20]. The results of this procedure in the case of argon are given in Table 1, where we derive a maximum relative contribution of 0.05%. The other gases yield about the same small numbers.

However, at lower energies such an estimate is very difficult to perform, especially for small angle inelastic scattering, so the magnitude of the correction term in the case of measurements with FC2 as the detector had to be investigated

TABLE 1. The energy dependence of the correction term with the RFA for Ar.

Energy (eV)	σ_{tot} † (a_0^2)	$\frac{d\sigma}{d\Omega}$ $(\theta \simeq 0)_{elastic}$ (a_0^2 sr^{-1})	correction (relative) $\frac{d\sigma}{d\Omega}\Delta\Omega/\sigma_{tot}$ (%)
100	29.6	$\simeq$90	0.02
200	21.3	$\simeq$85	0.03
300	17.5	$\simeq$80	0.04
400	14.9	$\simeq$75	0.05

†See table 5.

experimentally. Over a suitable energy range we measured the attenuated beam intensity at each data point with the RFA as well as with FC2. It was shown that both modes yielded the same results within the statistical errors of 1% for all the noble gases under study when $E_0 < 35$ eV. Consequently, below this energy we may safely neglect the correction term even if we use FC2.

2.3. Electron optics

2.3.1. Electron gun

Generally, an optical system can be specified by the way the entrance window and pupil are imaged, which is governed by the law of Helmholtz-Lagrange in the case of paraxial rays. The exit pupil and window fix the diameter and divergence of the beam in the target space. In our case, where we require a parallel beam flow between collision chamber and analyser, the electron gun has been designed in such a way that its entrance pupil is imaged in the centre of the collision cell and its entrance window in the analyser aperture, both with a diameter of about 0.5 mm.

It is essential that electrons with large radial velocity components are removed from the beam for two reasons: (a) to fulfil the requirement on the divergence of the final beam and (b) to keep chromatic aberrations small at low beam energies.

Therefore we chose a gun concept developed by Harting and Burrows [21] using a Pierce extraction system. For a detailed quantitative description of the optical system used, we refer to Blaauw [5]. Figure 2 shows the gun with additional lenses and the potentials applied are given in table 2. All the lens data used in the design are from the tables of Harting and Read [22].

The Pierce extraction system and the field-free region just behind the anode (1 and 2 in figure 2) act as a negative lens (lens 1) with the important property that electrons arriving at the anode under equal angles with respect to the optical axis, seem to originate from a virtual ring-shaped object in the focal plane of this lens. With the aid of a three aperture lens 2 this object is projected on a small diaphragm (50 μm), the so-called stripper, with magnification 6. In this way electrons which are transmitted through the stripper are angle selected. The stripper and the image of the anode can be recognized as the entrance pupil and window respectively with regard to the lens configuration behind the stripper. To keep the divergence of the beam small at the anode region, the cathode-anode spacing must not be too short (4 mm in our case) and therefore a rather large anode voltage (see table 2) is necessary to provide a sufficient extraction field. This means that the electrons have to be strongly decelerated behind the stripper for low impact energies. To avoid the use of a very thick lens and thereby aberrations, the deceleration is done in two steps, firstly by a two cylinder lens 3 with a voltage ratio of 6 : 1, and secondly by a three cylinder lens 4. Lens 4 is used as a zoom lens resulting in a fixed position of the anode image in the analyser aperture. The stripper lies in the first focal plane of lens 3 in order to keep the angles of the electron trajectories within manageable limits. In its turn, lens 4 images the stripper in its second focal plane, which shifts only weakly (10 - 15 mm) in the collision cell as one adjusts the zoomlens over the impact energy range. Another nice property of this zoomlens is that the magnification of the anode image varies only slightly for the range of potentials we apply. These two features guarantee that the conditions imposed on the final beam are fulfilled.

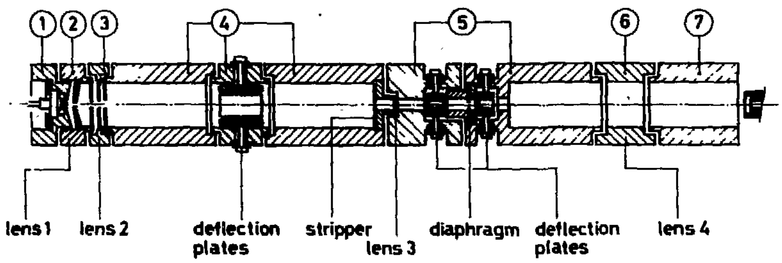

FIGURE 2

Cross section of the electron gun (diaphragms are not to scale). The numbers refer to the elements mentioned in table 2.

TABLE 2. List of applied voltages to the gun with respect to the cathode (1).

case	Number of the electrodes						
	1	2	3	4	5	6	7
a	0	250	700	250	42	to be adjusted †	15 < V' < 300
b	0	250	900	900	150	to be adjusted †	100 < V' < 1000

† According to the tables of Harting and Read [22].

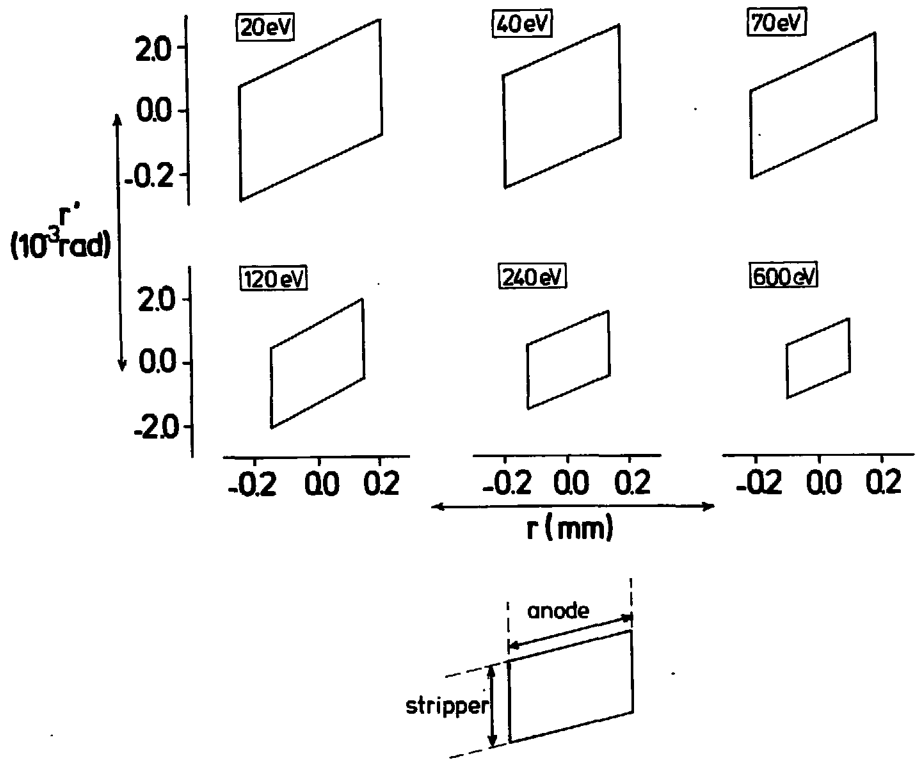

FIGURE 3

Phase space digrams, showing the beam characteristics at the analyser. The area of the parallellogram represents all possible combinations of r-position and angle for beam trajectories in the final image. The area becomes smaller with increasing impact energy, in accordance with Helmholtz-Lagranges' law. The size of the stripper influences only the beam angle, whereas the anode acts both upon the range of angles and final beam width.

A nice illustration of the overall performance of this gun design can be given with the help of the so-called transfer matrix formalism [23]. This method is directly connected with Liouvilles' theorem, which states that the density of particles in phase space (six-dimensional, three coordinates giving the position, the remaining three the momentum of each particle) is a preserved quantity, when subject to conservative forces. For an axial symmetric beam of electrons four coordinates can be eliminated, leaving only (r,p_r) as dependent coordinates, or better $(r,\ r' = p_r/p_z)$, where r' is the angle between the particles' momentum vector and the optical axis. Liouvilles' theorem can then be used by tracing some characteristic trajectories originating from the anode to the final image. For paraxial rays the transformation from $(r(z_1),\ r'(z_1))$ to $(r(z_2), r'(z_2))$ is linear and can thus be given by a matrix. Figure 3 shows the resulting phase diagrams at the analyser entrance aperture, for the anode and stripper dimensions of Ø 0.1 and 0.05 mm respectively. The area of each diagram is a direct measure for the beam quality, which becomes worse at lower impact energies. It also clearly illustrates the operation of the angle selection step: the stripper diaphragm only affects the divergence of the final beam, whereas the anode aperture affects both the final spot size as well as the divergence.

2.3.2. *Analyser*

The electrons are detected in a simple retarding field analyser, which is shown in figure 4. Kessler and Lindner [24] developed the principles on which this analyser type is based, which can be applied if the transverse energy of the incoming electrons is very small compared to their total kinetic energy.

The unscattered beam is decelerated to (almost) zero potential and passes through a small aperture (Ø 2 mm) in the retarding plate. After this retarding plate the electrons are brought back to their original energy and a three cylinder

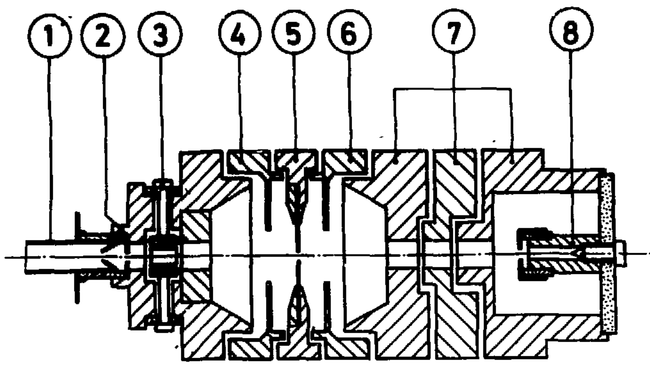

FIGURE 4

Vertical cross section of the retarding field analyser. 1, Faraday cup used to monitor the beam; 2, entrance aperture of the analyser; 3, deflection plates; 4,6 middle element of the Soa system; 5, retarding plate; 7, lens to focus the beam into: 8, Faraday cup.

lens behind the filter lens focuses the beam with a fixed energy in the Faraday cup. The energy resolution depends on the size of the entrance aperture and amounts 0.05% in our case: largely sufficient for removing inelastic scattered electrons from the attenuated beam over the whole impact energy range.

2.4. Adjustable collision cell

In order to perform differential scattering measurements, a short collision length is needed. The inevitable angular spread $\Delta\theta$ around the true scattering angle θ from separate points along the axis of the collision cell as seen from the analyser can be made small in this way. For small angles θ - taking the primary beam as infinitesimally narrow - the approximate relation holds:

$$\frac{\Delta\theta}{\theta} \approx \frac{L}{D} , \tag{2.4}$$

and this amounts at most 1% in our case with an interaction length L = 2 mm and distance D = 200 mm between cell and detector.

We constructed a cell, whose length could be adjusted from 0.2 - 10 mm by means of a rack-and-pinion system, as shown in figure 5. The main purpose to make its length variable was to have an experimental check of the length dependence on the target gas density. With this information we could use the cell for remeasuring total cross sections, thereby applying larger gas densities than with the former 42 mm collision chamber.

The cell is formed by the spacing between two molybdenum plates, the entrance plate with a diameter of 30 mm (and aperture ∅ 1 mm) and the exit plate of ∅ 68 mm (and aperture ∅ 2 mm). Both apertures have been drilled in a knife-edge shape towards the outer surface of the plates, in order to approximate infinitesimally narrow cell boundaries; otherwise, the apertures will establish short tubes of limited conducti-

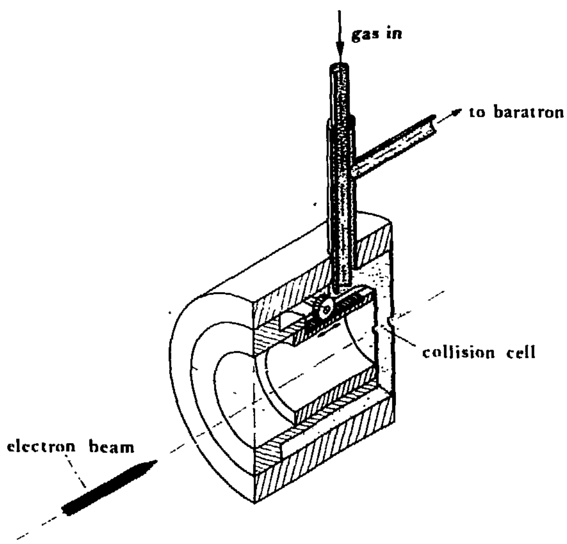

FIGURE 5

Construction details of the adjustable collision cell.

vity. The gas inlet consists of a narrow (i.d. = 3 mm) tube, which has been telescoped into an outer tube of i.d. = 8 mm. The gas flows into an annular space around the collision cell; through the outer tube it reaches the baratron sensing head. Apart from the thermal transpiration factor (see next section) no pressure drop will exist between the baratron and this annular space.

The retarding field analyser is replaced by the newly developed parallel plate analyser system, whose detailed description is deferred to the next chapter. A narrow (1 mm Ø) Faraday cage could be moved up and down pneumatically in front of the analysers entrance slit. Its function is the same as that of FC2 (see figure 1) in that it collects the attenuated beam current. This current is fed into the input terminal of a Keithley 610 meter; the meter delivers an output voltage proportional to the input current, which in its turn is fed into a microcomputer controlled ADC to ensure accurate current readout. The use of this narrow cup is allowed according to the criteria as formulated in section 2.2 (the subtended solid angle amounts $3 * 10^{-4}$ sr). The analyser with channelplate position sensitive detection enables us to check for a complete collection of the electron beam in the cup.

3. Experimental procedure and error discussion

3.1. Experimental procedure

The experimental procedure is based on the relation between the current attenuation and the total cross section as given by eq. (2.1). The procedure to measure the attenuation is actually the same for both the fixed (42 mm) and the variable collision cell. Firstly, the electron optics are optimally adjusted, secondly, the current I_c in the RFA or Faraday cage behind the cell is measured and thirdly, the cup in front of the collision chamber is moved downwards to intercept and measure the primary beam I_o. The total cross section is then derived by comparing the ratio (I_c/I_o) with and without gas in the collision chamber according to:

$$(I_c/I_o)_{gas}/(I_c/I_o)_{vac} = \exp(-NL\sigma_{tot}) . \quad (2.5)$$

In order to obtain reliable data, it is further necessary to determine L and N very accurately.

At the typical pressures we apply (less than 5 Pa) the density N is directly related to the gas pressure P_c in the collision cell:

$$N = 7.24 \times 10^{22} \frac{P_c}{T_c} \quad (2.6)$$

where the temperature T_c of the gas is in K, the target gas pressure in units of Pa (= 7.5 m Torr) and its density in m^{-3}. The baratron sensing head with which this pressure is measured, is kept at the elevated temperature of 322 K, a facility supplied by the manufacturer to protect the membrane housing against thermal fluctuations. This means however, that by thermal transpiration there exists a small pressure drop over the tube which connects the baratron with the gas cell at low pressures. It has been generally accepted that, if the mean free path length of the gas molecules is much larger than the diameter of the orifice or tube connection between the region at high (T_h) and low (T_c) temperature, the relation is valid as formulated by Knudsen [25] for this pressure drop:

$$D = (P_c/P_h) = T_c/T_h)^{\frac{1}{2}} . \quad (2.7)$$

At higher pressures, where the mean free path length becomes smaller than the specific dimensions of the apparatus, the collisions between the molecules themselves dominate, which results in the disappearance of the pressure drop. So, there exists a 'transition region' where the value of D as given by eq. (2.7) reaches unity asymptotically with increasing pressure. Measurements performed to investigate this effect more critically yielded different D values, all larger than the Knudsen limit [26,27,28]. It appeared that this D value depends on the specific dimensions of the connecting elements and tubes between the pressure gauge and gas cell. Therefore, it was necessary to measure the effect in our apparatus itself.

We connected a second baratron, symmetrically with respect to the first, with the collision chamber. Four combinations were checked: both manometers at room temperature, both at 322 K, and one at room temperature with the other at 322 K. No difference in pressure reading was found in the case of equal temperatures, which justifies the assumption of the absence of an unknown pressure drop over the tube connections. On the other hand, figure 6 shows the results for D as a function of the pressure of the target gas, when the baratrons were kept at unequal temperatures.

The onset of the transition region lies above 2 Pa for all the three gases helium, neon, and krypton. The low pressure limit value of D is significantly higher in comparison to what is to be expected from eq. (2.7), here 0.980 ± 0.005 vs. 0.955, thus confirming the findings of other experimentalists [26, 27,28]. By the inaccuracy of at least 0.3% for the low pressure data it is not legitimate to consider the differences in D between the various gases as real.

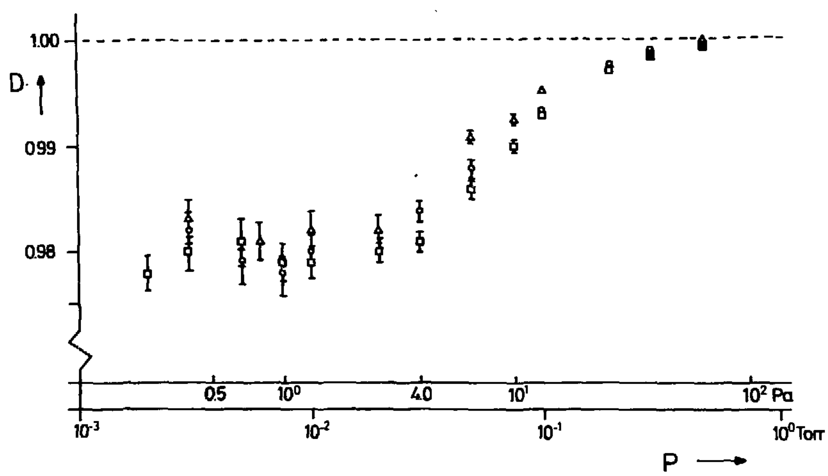

FIGURE 6

Dependence of the thermal transpiration ratio (D) on the pressure for helium (□), neon (O) and krypton (Δ).

Having established the correct relation between the local pressure in the baratron head and the collision cell region, we are left with the problem to determine the effective absorption length. At the typical pressures we apply, the mean free path length of the target gas atom is generally much larger than the dimensions of the collision cell, as can be seen from table 3 (data taken from Dushman [40]).

TABLE 3. Mean free path length L_{free} in mm for various gases at 0.5 Pa and 300 K.

Gas	H_2	He	Ne	Ar	Kr	Xe
L_{free}	24.8	39.3	27.9	14.1	10.9	8.0

One thus deals with effusive molecular flow through the entrance and exit apertures, where the gas will possess large density gradients. As such, the product (NL) in the exponent of eq. (2.5) has to be replaced by:

$$(NL)_{eff} = \int_S^D n(z)\,dz \tag{2.8}$$

This definite integral, with limits from particle beam source (S) to detector (D), accounts for the nonuniform distribution n(z) of scattering gas along the beam path. It is more convenient to define a correction factor α such that:

$$\int_S^D n(z)\,dz \equiv \alpha NL, \tag{2.9}$$

where N is the density as measured with the baratron (corrected for thermal transpiration) and L the geometrical length of the collision cell. Several approaches for calculating α are available in the literature, but the results strongly deviate from each other. For example, Mathur et al. [29] derived values for α smaller than unity for geometrical arrangements equal to our cell. His model predicts α, which is a function of the particular dimensions of the cell, to be very close to unity for large ratios of L over the orifice diameters. On the other hand, many experimentalists appear to be supporters of the model of Toburen et al. [30]. They argue that the density distribution outside the collision chamber remains the same as inside to a distance equal to the radius of the orifice and then falls off as the reverse square of the distance from the orifices. This results in an effective absorption length of $L_{eff} = L + d_1 + d_2$, where d_1 and d_2 are the diameters of the orifices, thus an α larger than unity. None of these models has been sufficiently verified by experiment. Therefore, we replaced the former cell of L = 42 mm by a shorter one of 14 mm, keeping the orifice diameters constant, and measured the total cross section for electron-helium scattering at impact energy of 60 eV. According to the approach by Mathur et al. [29] we had to expect only a slight decrease for the measured cross section (in the order of a few tenths of a percent), but Toburen's model predicted an increase in the order of 5%. The results of our test are shown in figure 7(a), where it can be seen that there is agreement with Mathur; therefore we are justified in applying the correction factor $\alpha = 1.00$ to the measurements with L = 42 mm.

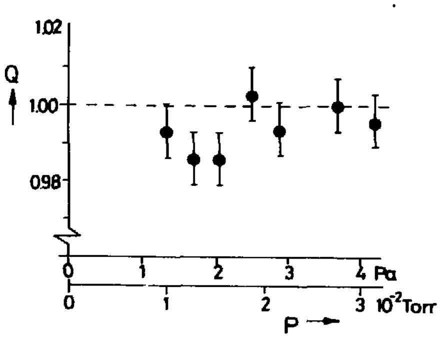

FIGURE 7(a)

The ratio Q of the total cross section measured with L = 42 mm and L = 14 mm for helium at 60 eV.

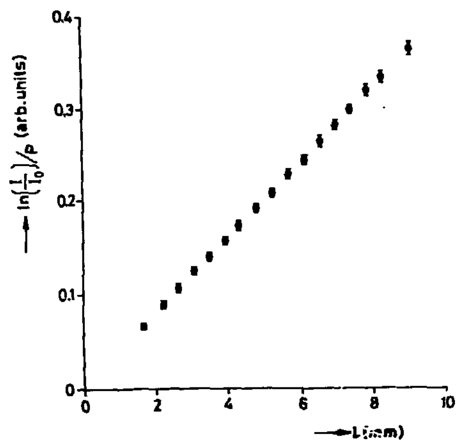

FIGURE 7(b)

Logarithm of the absorption ratio (see eq. (2.10)) divided by the pressure as a function of the short cell length; the points are averages of the values found at various krypton pressures. For $L > \approx 4$ mm all points follow a straight line, which crosses the X-axis at $L = 0$.

With respect to the new collision cell, adjustable from 2 - 10 mm, the situation is more critical. When this cell is made shorter, one enters a regime where, according to Mathur, α decreases substantially. We submitted the cell to a two-fold test. First we investigated the range of L, where α is still essentially equal to unity. In figure 7(b) the logarithm of the absorption ratio has been plotted as a function of the cell length. The points are averages of the values found at various pressures; it clearly demonstrates a linear behaviour for L values larger than $\approx 4 - 5$ mm, which means an $\alpha \approx 1.0$. With this cell adjusted to 4.5 mm, we repeated the total cross section measurements as performed previously with $L = 42$ mm.

Hereafter, we monitored the scattering intensities at the channelplate detector (to be described in the next chapter) as a function of L, where L could be reduced to almost zero. Since the number of scattered electrons is directly proportional to the target gas density N, this test presented a sensitive probe for determining α. For the differential scattering measurements, where L has been adjusted to 2 mm, the knowledge of $\alpha(L)$ is of crucial importance. The results of this test, together with values for α derived from a computer model, will be discussed in section 5.

Having established all the parameters involved and substituted eq. (2.6) and (2.7) in (2.5) finally leads to the following expression for the derivation of the total cross section:

$$\sigma_{tot} = -0.5 \frac{(T_c T_m)^{\frac{1}{2}}}{P_m L} \ln[(I_c/I_o)_{gas}/(I_c/I_o)_{vac}] \qquad (2.10)$$

where σ_{tot} is in a_o^2, T_c and T_m the temperatures in K in the gas cell and baratron head respectively, P_m the pressure in Pa in the baratron and L the cell length in cm.

The independence of σ_{tot} of the gas pressure and beam current was established for each gas at some sample impact energies.

The energy of the electron beam was calibrated by measuring the position on the energy scale of the pronounced 19.3 eV resonance for electron-helium scattering.

3.2. Error discussion

The only statistical errors of significance are the reading errors of the baratron due to pressure fluctuations; these are estimated to give an overall error of 1%.

On the other hand, we are faced with the following systematical error sources:

(a) the uncertainty in the interaction length, which amounts at most 1 - 2%;

(b) the calibration of the membrane manometer: the manufacturer guarantees an accuracy of 2.0% for a pressure of 0.13 Pa, 0.2% for 1.3 Pa and so on. As discussed earlier, only above ≈ 1 Pa this calibration appeared to be reliable; the use of the adjustable cell permitted us to stay safely above this under limit.

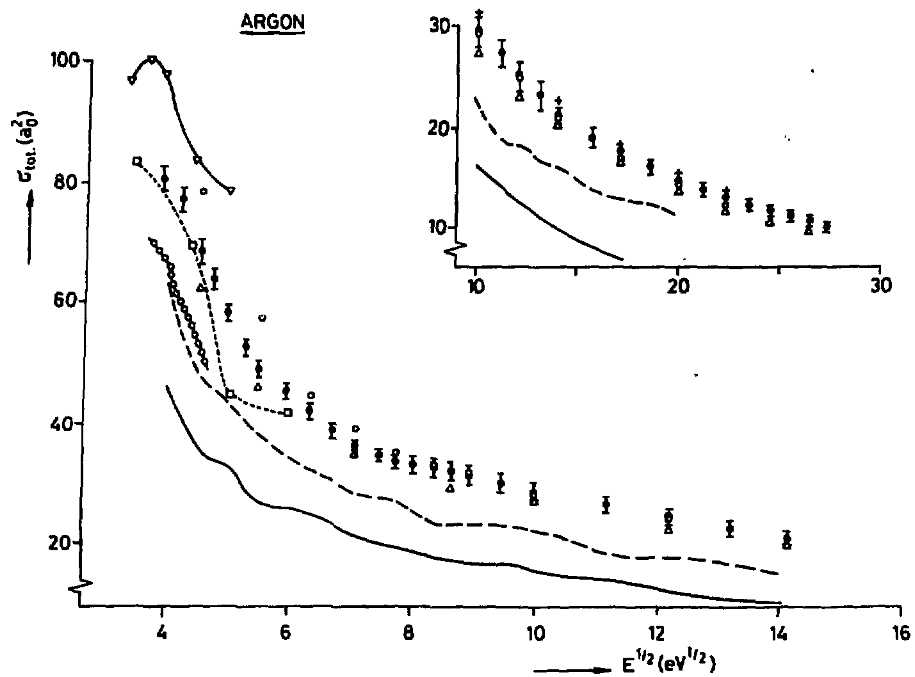

<u>FIGURE 8</u>

Total cross sections for electron scattering on argon. Present results, ▼; Kauppila et al., Δ; Golden and Bandel, -o-o-; Aberth et al., -∇-∇-; Ramsauer, ...□...□...; Normand, -----; Brode, ———; semi-empirical, de Heer et al., o; optical model, Byron and Joachain, +.

(c) the linearity of the current meter connected with a digital read-out unit: better than 0.5%.

(d) the energy definition: the uncertainty in this was estimated to be 0.3 eV; its influence on the accuracy depends on the energy and target gas.

Table 4 gives a summary of the errors, where we distinguish between two impact energy regimes.

TABLE 4. Survey of the experimental errors

Error source	Error estimation (1%)
- Statistical	$\lesssim 1$
- Systematical	
(a) interaction length	$\lesssim 1.5$
(b) baratron calibration	$\lesssim 0.5$
(c) linearity current meters	$\lesssim 0.5$
(d) energy definition,	
. for impact energies above ≈ 50 eV	$\lesssim 0.5$
. " " " below ≈ 50 eV	$\lesssim 1.5$
- Total error	
. below ≈ 50 eV	$\lesssim 5$
. above ≈ 50 eV	$\lesssim 4$

4. Results and discussion

4.1. Electron-argon total cross sections

The present results are shown in table 5 and figure 8. For reasons of clarity we included within parentheses the previously reported data [7], so far as we had to correct their values significantly. With the thus revised data set we now find overlap within 5% with Kauppila's [12] results below 50 eV. The 7 - 10% deviation at higher impact energies can be removed if incomplete screening against electrons scattered over small angles is taken into account. For, the cut-off angle in their apparatus was on the average 6°, whereas this amounted in our

TABLE 5. Total cross sections for electron-argon scattering in units of a_0^2.

E(eV)	Experiment								Semi empiri-cal	Theory	
	This work†	K	G,B	A	N	Bru	Bro	R	H et al.	OM I	OM II
15	79.32(82.76)	77.0	68.06	98.0		73.14		78.67			
17.5	76.72(79.42)		60.60			64.64		71.35			
20	68.75(73.70)	61.9	50.06	83.5	48.7	59.68	35.5	63.02	78.27		
22.5	62.55(67.02)				46.6	52.47	34.3				
25	56.81(60.52)			78.5	44.4	49.09	33.0	47.71			
27.5	51.33(54.95)					47.31					
30	48.76(50.72)	46.2			38.6	45.26	28.6	41.82	58.32		
35	44.83(46.41)				35.8	40.22	26.6	37.61			
40	41.94(53.40)				32.8	36.35	25.3		45.57		
45	38.27(39.92)				31.0	34.84	23.7				
50	36.65(37.30)	35.5			28.7		21.9		39.82		
55	35.16(35.53)				28.3		20.8				
60	34.55				27.7		19.7	23.45	36.60		
65	34.10										
70	33.23				24.2		18.3		34.66		
75	32.49	29.9									
80	31.80				24.2		17.6		32.15		
90	30.62				23.2		17.0		30.49		
100	29.60	27.4			22.7		16.2	18.03	29.56	31.5	33.3
125	27.35				18.9		14.6				
150	25.13	22.7			18.1		12.6		24.75		
175	23.03				16.6		11.1				
200	21.33	20.0			16.1		9.7		21.36	22.6	23.0
250	18.92				14.4		7.9				
300	17.47	16.4			12.9		6.7		16.81	18.3	18.2
350	16.09				12.1						
400	14.91	13.7			10.9				14.27	15.6	15.4
450	13.92										
500	13.08	11.7							12.51	13.7	13.4
550	12.35										
600	11.71	10.5									
650	11.15										
700	10.62	9.52									
750	10.13										

† : values within parentheses have been superseded [7]

K : Kauppila et al. [12]

G,B: Golden and Bandel [3]

A : Aberth et al. [31]

N : Normand [34]

Bro: Brode [35]

Bru: Brüche [33]

R : Ramsauer [2]

H : de Heer et al. [36]

OM : Optical model, Byron and Joachain [19].

set-up only 0.3°. With the optical model calculations of Byron and Joachain [19] they estimated the contribution of the integral expression in eq. (2.2) to be about 9% above 100 eV.

The remark of Aberth et al. [31] that in their crossed-beam recoil experiment electrons can be reflected back into the scattering region, causing their data to be 10 - 20% too high, is confirmed by our measurements.

The 10 - 15% lower results of Golden and Bandel [3] are rather surprising, since they carefully modified Ramsauer's early design and gave an overall error estimation of about 3%. However, a critical reconsideration of the error involved in the pressure determination led Salop and Nakano [32] to an estimation of about 10% with which Golden and Bandel's data could have been shifted.

For completeness we included the old measurements of Ramsauer [2], Bruche [33], Normand [34] and Brode [35], all performed in the twenties. These data are substantially too low, justifying as such the suspicion with respect to the first Ramsauer type of apparatuses.

De Heer et al. [36] constructed semi-empirical data from an analysis of experimental and theoretical total cross sections on excitation, ionization and elastic scattering and of differential cross sections for elastic and inleastic scattering. Above 70 eV their results are in good agreement with ours, better than 5%, but at lower energies the difference is larger.

The optical model calculations of Byron and Joachain [19], as far as series I is concerned, come close to our data.

4.2. Electron-krypton and xenon total cross sections

For electrons incident on krypton and xenon our results are in reasonable agreement with the semi-empirical data of de Heer et al. [36] above 100 eV. For Kr the difference varies from 2% at 100 eV to 7% at 500 eV, whereas for Xe it goes from 14% at 100 eV down to 10% at 500 eV; at lower

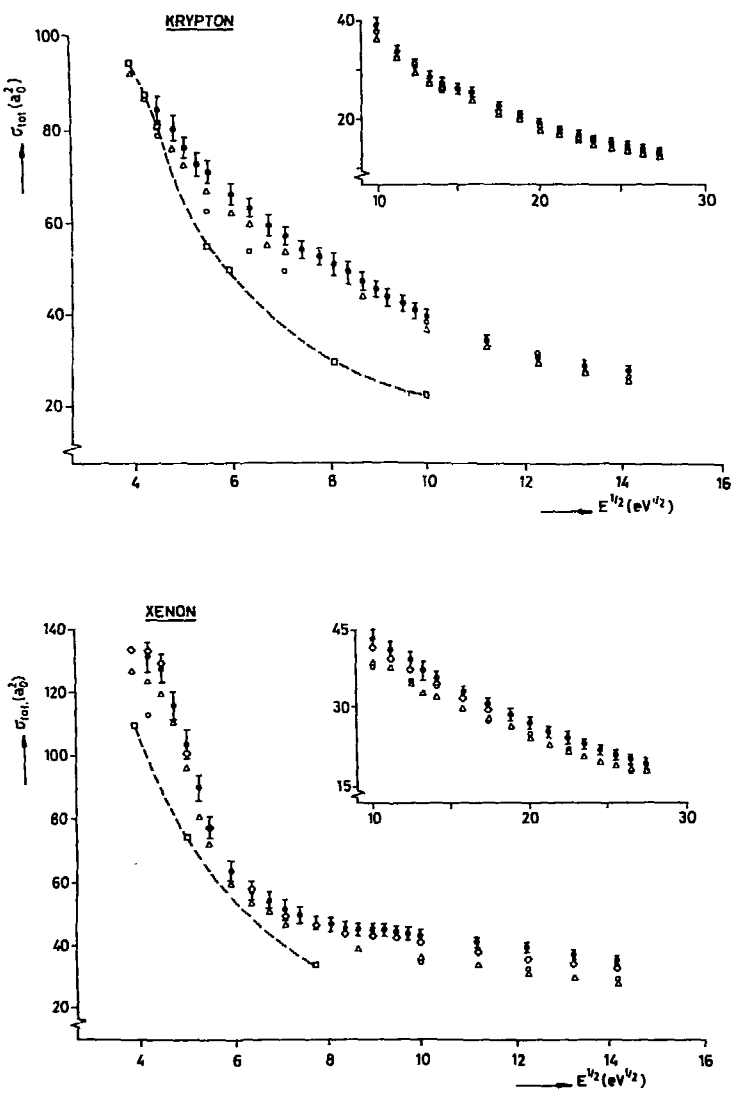

FIGURE 9

(a) Total cross sections for electron scattering on krypton. Present results, ⧳; Dababneh et al., Δ ; Ramsauer, □...□ ; semi-empirical, de Heer et al., o.

(b) Total cross sections on xenon. The same legend as under (a), with ◇ , Nickel et al.

energies these differences are larger. It has to be noted that their estimates for the total excitation cross section for Kr and Xe are - by lack of sufficient experimental and theoretical data - based on a scaling law and that below 100 eV the total elastic contribution mainly depends on one data set only. Therefore they suggested that it would be useful to have a second set of experimental data to compare within the energy range from about 20 to 100 eV. Dababneh et al. [13] extended the work of Kauppila et al. [12] on total scattering of positrons and electrons to Kr and Xe over the whole energy range from 0.35 - 750 eV. Comparison with our first data [7] showed their results to be lower everywhere, for Kr 15% at 22.5 eV to 7% at 750 eV, whereas for xenon the differences have a nearly constant value of 12%. Using the optical model results of McCarthy et al. [20] for the differential elastic and total inelastic cross sections, they estimated that their krypton (xenon) data could be 2 (4)%, 4 (8)%, 13 (16)% and 16 (18)% low at 20, 100, 500 and 750 eV respectively. These corrections for small-angle scattering would slightly improve the absolute value comparisons, but disrupt the good agreement that exists in the relative shapes of their results and ours above 50 eV. Still we thought it worthwhile to repeat some measurements with the adjustable collision cell as mentioned in the previous section. It appeared that above 70 eV no correction was needed, whereas at energies below 70 eV we had to lower our previous results, ranging for krypton (xenon) from 3 (2)% at 70 eV to 6 (5)% at 20 eV. The results are given in table 6 and figure 9. We should note here that Dababneh's estimated small angle corrections are probably too pessimistic, since these also contain contributions from inelastic scattering, whereas their retarding field discriminates near 100% against electrons which have transferred some of their energy during the collision. Anyhow, for krypton the agreement between our revised data and those of Dababneh is better than 5% over the whole overlapping energy range. The xenon results now come close together below 50 eV, and also between 50 and 200 eV when the small angle correction is taken into account, but at the higher energies this correction leads to a difference up to 7% at 750 eV.

TABLE 6. Total cross sections for electron-krypton and -xenon scattering in units of a_o^2.

E(eV)	krypton: experiment: this work*	krypton: experiment: D	krypton: semi emp.: H	xenon: experiment: this work*	xenon: experiment: D	xenon: experiment: Ni	xenon: semi-emp.: H	xenon: semi-emp.: Ha
15		91.9			126.8	132.1		127.0
17.5		86.8		(137.3)	123.9	131.1		
20	84.67	81.1	78.57	123.83(133.0)	119.6	127.7	110.2	118.9
22.5	79.93(87.16)	75.6		114.92(123.5)	110.9			
25	74.48(81.28)	71.8		102.56(110.1)	96.1	98.9		
27.5	70.82(76.50)	68.47		87.60(94.73)	81.5			
30	68.45(72.63	66.70	62.22	74.45(79.85)	71.99	74.2		70.7
35	63.77(66.94)	61.36		61.08(64.95)	59.81			
40	59.42(62.99)	58.85	53.28	55.95(58.62)	53.45	56.1		
45	56.86(59.90)	53.96		53.27(55.64)	50.74			
50	54.23(56.71)	53.03	48.72	50.83(53.10)	46.81	49.8		46.4
55	52.65(54.27)			49.16(50.27)				
60	51.35(52.33)			47.55(48.25)		47.1	36.85	
65	50.56			46.90				
70	48.76			46.19		45.2		
75	46.85	42.27		45.92	41.59			
80	45.04			45.63		44.1		
85	43.39			45.15				
90	41.83			44.63		43.3		
95	40.38			44.07				
100	39.04	37.02	38.25	43.51	38.66	42.5	38.10	38.2
125	33.92	33.41		41.44	37.19	39.7		
150	30.68	30.52	31.01	39.40	34.91	37.9	35.51	
175	28.88	27.66		37.61	33.16			
200	27.68	26.38	26.06	36.02	32.48	35.4	34.24	33.9
250	25.32	23.34		33.27	30.02	32.8		
300	22.81	21.31	21.77	30.95	28.09	30.5	27.80	28.9
350	20.80	19.77		28.93	26.06			
400	19.25	18.10	18.69	27.32	24.70		25.56	
450	18.12	16.96		25.83	22.92			
500	17.12	15.96	16.06	24.53	21.92		22.36	22.8
550	16.26	14.96		23.40	20.70			
600	15.54	14.31		22.38	19.24			
650	14.90	13.49		21.45	18.38			
700	14.29	12.92		20.56	18.45		18.40	
750	13.67	12.56		19.68	17.38			

* values within parentheses have been superseded [7]

D : Dababneh et al. [13]

H : de Heer et al. [36]

Ni : Nickel et al. [37]

Ha : Hayashi [38].

This remaining discrepancy points at a systematical error involved in Debabneh's xenon data. Just recently, Nickel et al. of the group of Trajmar [37] (and private communication) remeasured total cross sections for a whole series of noble gases and simple molecules. The basic features of their apparatus - of the same linear absorption type as our design - are a low cut-off angle (<≈1°) for small angle elastic scattered electrons and a complete screening against inelastic scattering at the final current collecting Faraday cage; they claim an overall accuracy of 2%. The similarity in set-up and angular resolution provides a sensitive test for the correctness of both ours and Nickel's data. Indeed, their xenon results appeared to confirm our data within 2% over the whole energy range of overlap; in particular between 100 and 300 eV the agreement is excellent. Nickel's data put even more weight in the balance, since they confirmed all ours, Kauppila's and Kennerly's results on helium and neon within 1 - 2%. So, we may definitely state that the cross sections Dababneh found for xenon above ≈ 50 eV are in error.

The semi-empirical data of de Heer et al. [30] clearly deviate from the results of all experimental groups below ≈ 100 eV. Very recently, Hayashi [38] redetermined total excitation cross sections σ_{exc} for electron-xenon scattering by carrying out the following profound procedure. First, he selected recommended values of elastic momentum transfer and ionization cross sections. Secondly, he applied a scaling law to Eggarter's [39] σ_{exc} data for argon, which were about twice the values of de Heer et al. in the energy range of 20 - 50 eV; the resulting σ_{exc} data for xenon merged with de Heer's data first at 300 eV. From the thus constructed data he was able to derive values for the Townsend ionization coefficient α, which are rather sensitive to the chosen σ_{exc}. Comparing these values for α with those obtained from swarm experiments showed agreement only if Eggarter's σ_{exc} data had been used as input, clearly demonstrating that the values for σ_{exc} as recommended by de Heer were too low. Summing up all contributions to the total cross section now yields values much more in accordance with the experimental data below 100 eV, as can be seen from table 6.

4.3. Conclusions

Total cross section measurements have been presented for electron scattering from Ar, Kr and Xe, claiming an accuracy of better than 5% and performed under very well defined conditions of angular and energy resolution. Our apparatus yielded systematically higher data than most other experiments; the explanation must be found in a more complete compensation for forward scattering in our set-up than achieved by others. Indeed, for argon and krypton good agreement is found with the recent data of Kauppila and coworkers if their suggested correction for this effect is taken into account. Particular care had to be taken at the lower impact energies in the precise determination of the target gas pressure for krypton and xenon; with a shorter collision cell we could refine our previous measurements. The confidence in our xenon data has just recently been strengthened by the measurements of Trajmar and coworkers, who chose for the same scattering geometry as we did.

5. Effective gas density in short scattering chambers

In this section we shall investigate the influence of apertures in short cylindrically shaped collision chambers on the scattering gas density distribution $n(z)$. In section 3.1 we introduced a factor α, which accounts for the nonuniformity of $n(z)$ along the beam axis due to the effusive gas flow through the apertures as (eq. (2.9)):

$$\int_S^D n(z)dz = \alpha NL,$$

and suggested that its value will become smaller than unity when the actual cell length is shortened. A simple geometrical picture, figure 10, shows, that in our case, where the exit aperture is twice as large as the entrance aperture, the lower integration limit S lies at exactly a distance L in front of the collision cell.

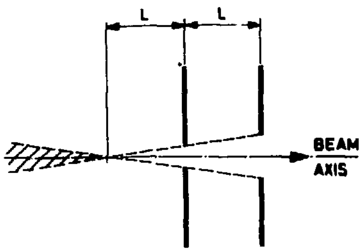

FIGURE 10

Shadow cone in front of the collision cell due to unequal size in entrance and exit aperture. The cone indicates the area into which no molecule can effuse.

It is our purpose here to compare the results for α obtained from a computer simulation with those we found experimentally. The latter were obtained by counting the number of scattered electrons in a fixed angular range as a function of L, thereby keeping a constant density N as measured by the baratron. This procedure was justified, since L was always at least an order of magnitude smaller than the distance between cell and channelplate detector (cf. eq. (2.4)). We shall first discuss the computer model, in particular the assumptions on which it is based. The model is basically the same as proposed by Mathur et al. [29], but we extended it to our cell configuration with apertures of unequal diameter.

Consider the case of a rarefied gas, confined in a cylindrically shaped volume, where gas phase collisions are practically negligible compared to molecular impacts on the walls, and where the walls reflect molecules diffusively according to the cosine law. The first condition is generally satisfied since mean free paths are usually long compared to chamber dimensions (see table 3). Compliance with the second condition is more difficult to establish with general confidence, but at room temperature and below, the reflection mechanism may be considered to involve an intermediate step of temporary adsorption on the walls and subsequent evaporation whereby the memory of the incident direction is lost, giving a cosine distribution. The contribution to the local number

(a)

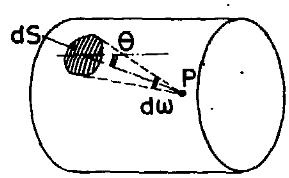

FIGURE 11(a)

Showing the solid angle which is subtended at a point P inside the cell by a wall surface element dS.

(b)

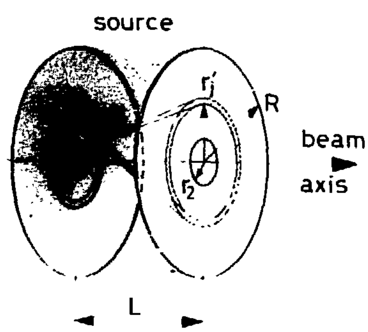

FIGURE 11(b)

Geometry and notation used to evaluate the incident flux on a flat ring of radius r_i' due to reflection from a flat ring of radius r_j' at the opposite cell wall. A steady state flow of gas from the annular source region is assumed throughout the calculations.

density near a point P in the body of a gas by molecules diffusively reflected from a surface element dS on a wall is:

$$dn_p = n_s (d\omega/4\pi) \cos\theta, \tag{2.11}$$

where $d\omega$ is the solid angle subtended at P by the surface element in question and n_s the effective equilibrium gas density at which the element appears to reflect, shown in figure 11a. The factor $\cos\theta$ accounts for the diffusive reflection where the angle θ is defined with respect to the normal on the wall surface. The total number density at P is found by integrating the above equation over all of the walls and, if present, source regions exposed to P:

$$n_p = 1/1\pi \int n_s \cos\theta \, d\omega. \tag{2.12}$$

The following parameters fix the cell geometry: L is the length of the cell, r_1 and r_2 the radii of the entrance and exit aperture respectively and R the cell wall radius. The walls are assumed to be of negligible thickness (i.e. the apertures are of knife-edge shape). Further, let the cylindrical walls be divided into c_1 respectively c_2 circular rings of equal width, as in figure 11(b).

Now the procedure to calculate the steady-state conditions in such cells involves the following basic steps:

(i) Choose start values for the apparent equilibrium gas number densities n_i characteristic of the intensities of diffuse reflection from each of the various rings. These densities are taken constant in each ring element.

(ii) Calculate the total flux of molecules, Γ_i, incident on each ring element from the opposite wall and the cylindrical 'source' region.

(iii) Replace the trial values of n_i with those obtained by requiring the rates of reflection from the surface elements to be equal to the rates of molecular incidence on them:

$$\tfrac{1}{4} n_i \bar{v} = \Gamma_i, \tag{2.13}$$

where $\bar{v}$ is the average molecular speed and Γ_i the number of incident molecules per unit surface and time.

(iv) The process is continued by iteration until suitable convergence is achieved for Γ_i and n_i.

As reasonable starting values we did choose for n_i in the ring nearest to the apertures $N(1.-\Delta\Omega_{frac})$, where N is the source density and $\Delta\Omega_{frac}$ the fractional solid angle subtended at a point on such a ring by the opposite aperture; the initial gradient was taken to be linear between source and this ring. The source density was kept constant during the whole iteration process; this is a realistic approach to our actual cell construction, since the gas flows from a large bulk volume, where its density N is measured, into the space between the entrance and exit plate (see figure 5). The partial flux $\Delta\Gamma_{ij}$ of molecules to an element dS of ring i reflected from ring j on the opposite wall reads (eq. (8) of [29]):

$$\Delta\Gamma_{ij} = n_j \frac{\bar{v}}{4} \cdot \tfrac{1}{2} \left(\frac{r^2 - L^2 - r_i'^2}{[(L^2 + r_i'^2 + r^2)^2 - 4r_i'^2 r^2]^{\frac{1}{2}}} \right)_{r = r_j'}^{r = r_{j+1}'} \quad (2.14a)$$

and for the flux Γ_S directly from the source region one can write (eq. (7) of [29]):

$$\Gamma_S = N \frac{\bar{v}}{4} \cdot \tfrac{1}{2} \left(1. - \frac{R^2 - r_i'^2 - L^2}{[(R^2 - r_i'^2)^2 + 2L^2(R^2 + r_i'^2) + L^4]^{\frac{1}{2}}} \right) \quad (2.14b)$$

The total incident flux Γ_i at r_i' is then given by:

$$\Gamma_i = \sum_{j=1}^{c_2} \Delta\Gamma_{ij} + \Gamma_s \quad (2.15)$$

After obtaining these fluxes, eq. (2.13) is used to determine new values of the effective radiative densities at the walls, and a next iteration loop can be started until the convergence is satisfactory. Figure 12 shows a typical density gradient along the walls for our cell geometry with L = 2 mm, obtained after 21 iterations with 60 rings. The densities in opposite rings become clearly different from each other in the neighbourhood of the apertures, since these are unequal in size.

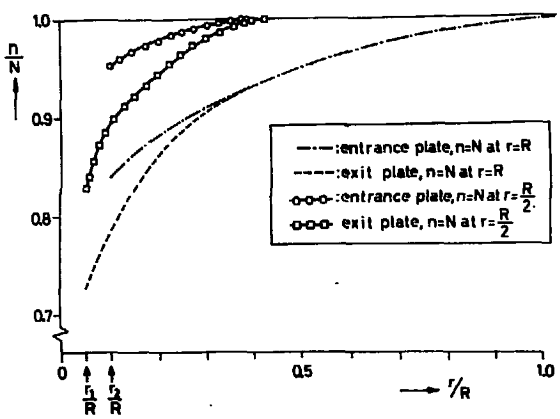

FIGURE 12

Density gradients along the circular cell walls due to effusing of the gas through the apertures, shown for two different cell plate radii R. The displayed densities have been normalized on the source density N for a cell length L = 2 mm and aperture radii $r_1/r_2 = 0.5$ (indicated by arrows).

Having determined the effective densities at the walls, it is now a simple matter with the help of eq. (2.12) to calculate the equilibrium density in each point inside and outside the cell. Figure 13 shows the non-uniform density distribution n(z) along the cell axis, normalized on N for three cell lengths and three values of r_1/r_2, as calculated by the above model.

The significant asymmetry in the profile is a direct consequence of the unequal aperture sizes. One clearly sees the reduction in density along the beam axis with decreasing cell length, which will result in a smaller α. Besides, the contribution from the lob of effusing gas outside the exit aperture to the integral in eq. (2.9) will become increasingly important at small L. Consequently, the gain in confinement of the gas by reducing L will be got lost for a great part by this streaming out effect: an inherent feature of gas cell configurations, which can be circumvented by using atomic beams.

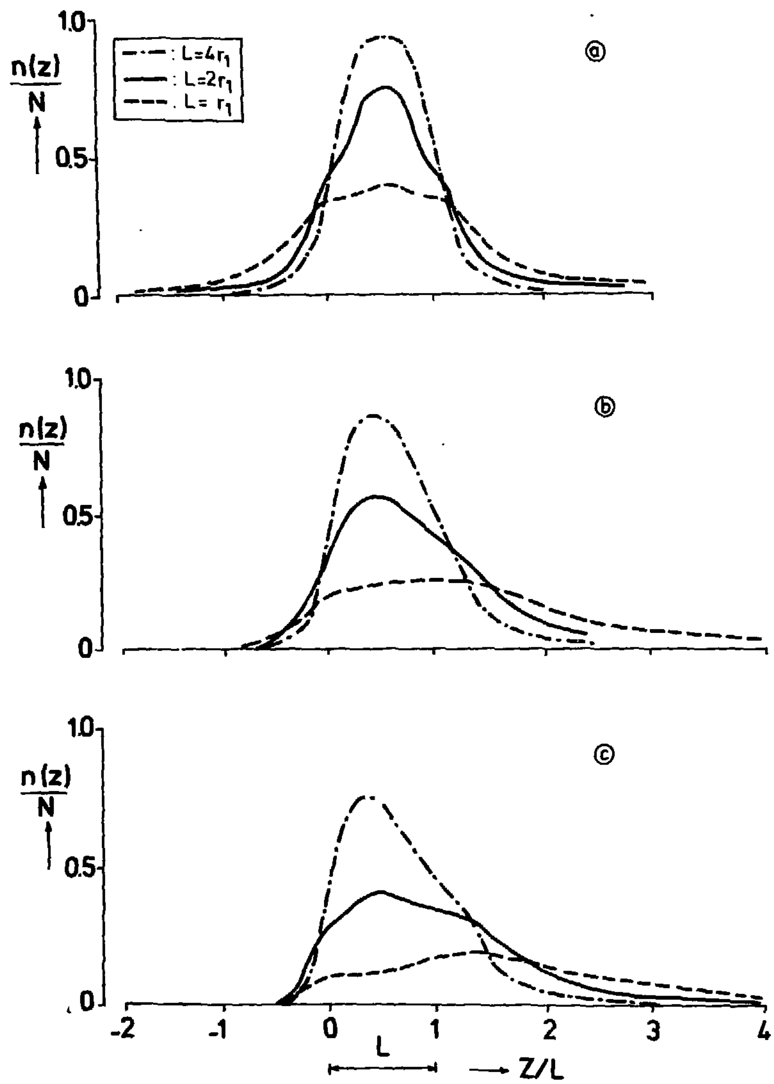

FIGURE 13

Non-uniform gas density distribution along the beam(z) axis at three different cell lengths L. The distribution is smeared out when L is made shorter; besides its peak value decreases substantially. Three ratios for r_2/r_1 have been used: (a) $r_2/r_1 = 1$, (b) $r_2/r_1 = 2$ and (c) $r_2/r_1 = 3$.

TABLE 7. Calculated values for α at various ratios of the cell length L over the entrance aperture radius r_1; three different exit aperture radii have been considered.

L/r_1	0.5	1.0	1.5	2.0	3.0	4.0	6.0
$\alpha(r_2 = r_1)$	0.45	0.58 (0.61)	0.69	0.79 (0.80)	0.88 (0.89)	0.93 (0.93)	0.97
$\alpha(r_2 = 2r_1)$	0.29	0.44	0.56	0.66	0.76	0.86	0.93
$\alpha(r_2 = 3r_1)$	0.24	0.38	0.49	0.58	0.70	0.80	0.88

Table 7 contains the calculated values for α as a function of L at three ratios of r_1/r_2; in all cases we fixed $R/r_1 = 20$. Within parentheses we have added the values of Mathur [29], calculated for $r_1/r_2 = 1.0$.

The values for α at $r_1/r_2 = 0.5$ are shown in figure 14(a) together with the experimental results. The experiment yields significantly higher α values than those derived from the computer model; already at $L = 2.5$ mm we found $(1.00 - \alpha_{exp}) < \approx 0.01$. Noteworthy here is the fact that the experimental check Mathur performed on his calculated data also resulted in higher values than his model predicted. He attributed this deviation to the finite thickness of the cell plates; as such, the apertures would present extra channels with corresponding small conductivities. Whereas this might be the case for the cell he used, our results on the other hand exclude such a mechanical cause. For, as can be seen from figure 14(b), our data at $L > 2.5$ mm lie on a straight line, which, when extrapolated down to signal $S = 0$, definitely crosses the axis at $L = 0$.

So, in order to find the cause for the observed discrepancy, we have to examine the basic assumptions in the model more critically. With respect to the mean free path length, table 3 shows that these are at the shortest cell lengths over a magnitude larger than L; yet, we checked α at various pressures, ranging from 0.1 - 3 Pa. No dependence for α on this parameter was found, so this could be ruled out as the possible cause. As said before, the assumption on diffuse reflection is not directly amenable to experimental tests.

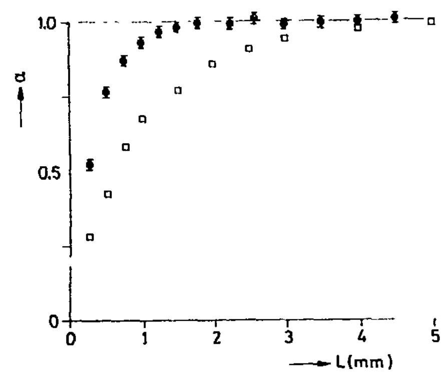

FIGURE 14(a)

Calculated values for the correction factor α from the computer model (□) and numbers derived from experiment (⧳). The entrance and exit aperture diameters in our cell were 1.0 and 2.0 mm respectively. Clearly, the model calculations are incapable of matching the experimental values.

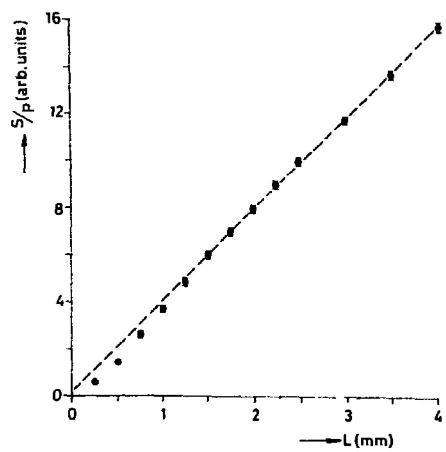

FIGURE 14(b)

Plot of the number of scattered electrons S as a function of the cell length L, taken at various argon pressures. First at $L <\approx 2.5$ mm a density drop sets in, resulting in $\alpha < 1.0$. Above $L \approx 2.5$ mm all points lie on a straight line which crosses the X-axis at $L = 0$.

One way would be heating or cooling the cell. Another approach should consist of building in the model other reflection distributions; this requires a whole research project on itself with matching experimental tests on different cell geometries, which lies outside the scope of the present study. An indication might be that the measured values for α could be simulated by our model, when one assumes the density drop along the walls taking place first in rings at 3 - 5 times the aperture radius from the beam axis (see figure 12). Such a local density drop will indeed occur, if a significant part of the molecules does not reflect diffusively, but instead specularly. Monte-Carlo calculations should be most appropriate for a numerical test; unfortunately, we had not yet the occasion to perform these.

Another, physically more appealing, argument can be put forward, if one considers in figure 12 the steep density drop along the walls towards the apertures more critically. Since noble gas target atoms are only weakly bound at the wall surface during a collision, part of them will "creep" over the surface before actually evaporating back into the vacuum. As such, a two-dimensional gas layer is attached to the wall; the density gradient will work as a pump on it and consequently a small diffusion current is set going as to raise the gradient. The net result is that part of the incoming flux Γ_i of eq. (2.13) will be pumped towards the apertures instead of being diffusively reflected. However, we were not able to put this speculative view on a more quantitative basis.

Although our model was incapable of matching α exactly on experiment, its predicted relative density distribution does not suffer from this deficiency. As such, figure 13 serves as a reliable figure of merit; in particular it shows that for $L = 2$ mm over 75% of the target gas is confined in the cell.

Two main conclusions can be drawn from the preceding analysis. First, the gas density drop is not as drastically as one would expect on the basis of simple gas dynamics with diffusive reflection from surrounding walls. Further research, with the emphasis on surface layer diffusion, is necessary in order to provide widely applicable model calculations.

The second is that the generally adopted standard of considering the effective absorption length as the actual cell augmented with the sum of the aperture diameters lacks any justification. Only if thick cell walls or high pressures are used, it will indeed approach the real situation.

References

[1] Bederson B and Kieffer L J, Rev.Mod.Phys. 43, 601 (1971).

[2] Ramsauer C, Ann.Phys. 64, 513 (1921) and 66, 546 (1921).

[3] Golden D E and Bandel H W, Phys.Rev. 138, A14 (1965).

[4] Dalba G, Fornasini P, Lazizzera I, Ranieri G and Zecca A, J.Phys.B: Atom.and Molec.Phys. 12, 3787 (1979).

[5] Blaauw H J, On the forward dispersion relation for electron-atom scattering (thesis), Amsterdam (1979).

[6] Blaauw H J, Wagenaar R W, Barends D H and de Heer F J, J.Phys.B: Atom.and Molec.Phys. 13, 359 (1980).

[7] Wagenaar R W and de Heer F J, J.Phys.B: Atom.and Molec.Phys. 13, 3855 (1980).

[8] Van Wingerden B, Wagenaar R W and de Heer F J, J.Phys.B: Atom.and Molec.Phys. 13, 3481 (1980).

[9] Milloy H B and Crompton R W, Phys.Rev.A 15, 1847 (1977).

[10] Kennerly R E and Bonham R A, Phys.Rev.A 17, 1844 (1978).

[11] Kauppila W E, Stein T S, Jesion G, Dababneh M S and Pol V, Rev.Sci. Instr. 48, 822 (1977).

[12] Kauppila W E, Stein T S, Smart J H, Jesion G, Dababneh M S and Pol V, Phys.Rev.A 17, 1600 (1978) and Phys.Rev.A 24, 725 (1981).

[13] Dababneh M S, Hsieh Y F, Kauppila W E, Pol V and Stein T S, Phys.Rev. A 26, 1252 (1982).
Dababneh M S, Kauppila W E, Downing J P, Laperriere F, Pol V, Smart J H and Stein T S, Phys.Rev.A 22, 1872 (1980).

[14] Hoffman K R, Dababneh M S, Hsieh Y F, Kauppila W E, Pol V, Smart J H and Stein T S, Phys.Rev.A 25, 1393 (1982).

[15] Nesbet R K, Phys.Rev.A 20, 58 (1979).

[16] Fon W C, Berrington K A and Hibbert A, J.Phys.B: Atom.and Molec.Phys. 14, 307 (1981).

[17] Dewangen D P and Walters H R J, J.Phys.B: Atom.and Molec.Phys. 10, 637 (1977).

[18] Byron F W, Phys.Rev.A 17, 170 (1978).
[19] Byron F W and Joachain C J, Phys.Rev.A 15, 178 (1977) and J.Phys.B: Atom.and Molec.Phys. 10, 207 (1977).
[20] McCarthy I E, Noble C J, Phillips B A and Turnbull A D, Phys.Rev.A 15, 2173 (1977).
[21] Harting E and Burrows K M, Rev.Sci.Instr. 41, 97 (1970).
[22] Harting E and Read F H, Electrostatic lenses, Elsevier Publ.Co. (1976).
[23] DiChio D, Natali S V and Kuyatt C E, Rev.Sci.Instr. 45, 559 (1974).
[24] Kessler J and Lindner H, Z.Angew.Phys. 18, 7 (1964).
[25] Knudsen M, Ann.Phys.Lpz. 31, 205 (1910).
[26] Edmonds T and Hobson J P, J.Vac.Sci.Technol. 2, 192 (1965).
[27] Bromberg J P, J.Vac.Sci.Technol. 6, 801 (1969).
[28] Baldwin G C and Gaerttner M R, J.Vac.Sci.Technol. 10, 215 (1973).
[29] Mathur B P, Field J E and Colgate S O, Phys.Rev.A 11, 830 (1975) and Mathur B D and Colgate S O, Phys.Rev.A 6, 1266 (1972).
[30] Toburen C H, Nakai M.Y. and Langley R A, Phys.Rev.A 171, 114 (1968).
[31] Aberth W, Sunshine G and Bederson B, Proc.3rd ICPEAC (Amsterdam), Abstracts p.53 (1964).
[32] Salop A and Nakano H H, Phys.Rev.A 2, 127 (1970).
[33] Brüche E, Lilienthal D and Schrodter K, Ann.Phys. 84, 279 (1927).
[34] Normand C E, Phys.Rev. 35, 1217 (1930).
[35] Brode R B, Phys.Rev. 25, 636 (1925).
[36] de Heer F J, Jansen R H J and van der Kaay W, J.Phys.B: Atom.and Molec.Phys. 12, 979 (1979).
[37] Nickel J, Imre K, Register D F and Trajmar S, Book of Abstracts XIIIth ICPEAC, Berlin, p.93 (1983).
[38] Hayashi M, J.Phys.D: Appl.Phys. 16, 581 (1983).
[39] Eggarter E, J.Chem.Phys. 62, 833 (1975).
[40] Dushman S, Scientific foundations of vacuum technique 2nd ed., Wiley and Sons, p.32 (1962).

CHAPTER III

A parallel plate electrostatic energy analyser for the simultaneous measurement of doubly differential cross sections for small angle electron scattering

Abstract

A novel type of parallel plate electrostatic energy analyser is described with position sensitive detection of the particles leaving the exit slit of the analyser, different positions corresponding to different scattering angles. The angular distribution of the scattered electrons in a 10° angular range around the direction of the primary beam can be measured simultaneously with energy resolution $\Delta E/E = 0.0125$ and angular resolution 0.1°. The energy resolution can easily be enhanced up to a factor of five by retarding the scattered particles before entering the analyser. A spherically shaped electrode system has been developed for this purpose, which retards the particles without in principle distorting their trajectories.

The use of microchannelplates as detector yields an improvement in measurement efficiency with at least a factor of 10^2 with respect to the traditional angular scan technique. Extension to a two-dimensional readout is possible, resulting in a simultaneous detection of an energy-loss spectrum. In that case a final gain in efficiency of 10^4 or even more is attainable.

1. Introduction

In many kinds of electron scattering experiments one is interested in the variation of the angular distribution of the scattered electrons as a function of their energy loss in the collision. Usually, an electrostatic energy analyser with a small acceptance aperture is used for this purpose and a mechanical scan is made over the angular range of interest. However, this scheme is rather slow because every angle and pass energy has to be set and measured separately.

In the past, several attempts have been made to improve this inefficient way of detection. Geiger et al. [1] modified a Möllenstedt type of analyser in which only elastically scattered electrons are transmitted in a very small (<10 mrad) angular range around the primary beam axis. These were then simultaneously recorded on a photographic plate. This principle can only be applied in the high keV energy range. Pauty et al. [2] used a parallel plate analyser in combination with an electronic camera for the analysis of emitted photo-electrons, where both the energy spectrum and the angular distribution were recorded on a photographic plate in a single measurement. The electrons were preaccelerated before entering the analyser through a rectangular slit. This however resulted in a complicated transfer function.

Since recently [3,4] microchannelplates have proven their reliability in particle detection, a powerful high-resolution technique for real time analysis has become available. Instead of developing a photographic emulsion after a certain exposure time, now a spectrum can be built up and made visible continuously during the measurement itself. It is this feature which does research groups in many fields of spectroscopy switch over to channelplate detectors [5,6,7,8].

Our apparatus was developed primarily for the measurement of small angle elastic scattering of electrons by atoms and molecules at low and intermediate collision energies (i.e. between 15 eV and 4 keV) in order to study the polarization of the target during passage of the projectile electrons. Tiny structural features upon the large forward polarization peak, if there are any, should be resolvable. For this purpose a parallel plate electrostatic energy analyser has been constructed in such a way, that the angle of the scattered electrons with respect to the primary beam axis remains unperturbed during energy dispersion. After leaving the curved exit slit the electrons are simultaneously detected by a chevron mounted channelplate system.

Since we are at first concerned with elastic scattering only, the analyser was set such as to transmit only these electrons through the exit slit. We could therefore confine ourselves to a one-dimensional readout of the detector. However, with an enlarged exit plane of the analyser and extended detection electronics, simultaneous doubly differential cross-section measurements are possible.

This chapter has been divided as follows. In section 2 we give a summary of the experimental set-up, thereby indicating somewhat in detail the way the primary beam is focused. The analyser is extensively described in section 3. Section 4 deals with the position sensitive detector and the necessary read-out electronics. In section 5 the performance of the system is discussed. The design and optical properties of a concentric spherical electrode system, by which the scattered electrons can be retarded before they enter the analyser, will be considered in section 6. Using retardation, the fixed resolving power of the instrument suffices even at high impact energies for the discrimination between elastic and inelastic scattering. Finally, in section 7 we shall shortly discuss some results where argon has been used as target gas, and compare them with data as found by others previously.

2. Apparatus

2.1. Experimental set-up

The complete apparatus is shown schematically in figure 1. A narrow ($\emptyset \leq 0.75$ mm), parallel beam of electrons with energy E_o ranging from 15 eV to 4 keV, is produced by an electron gun, as described in the previous chapter (see also Blaauw et al.

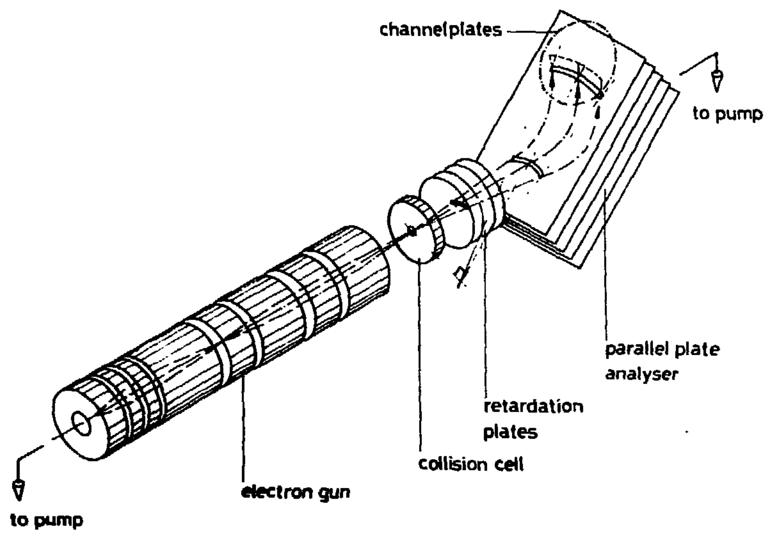

FIGURE 1

Schematic view of the apparatus for small angle electron scattering.

[9]). Only the voltages on the final two lens elements of this gun have to be adjusted for scanning the beam energy. Since we are interested in elastic scattering, a narrow energy spread of the beam is not required, so the typical thermal energy distribution of 0.3 eV from the emitting filament can be admitted. The beam is led through a static gas collision chamber, where a Ø 0.7 mm diaphragm just in front of it avoids scattering of the beam electrons off the edges of the cell aperture. This would otherwise blur the distribution of electrons scattered from the target gas. The cell has been made short (2 mm) in order to concentrate the collision essentially to one point. From this centre the electrons travel a distance of 70 mm before entering the analyser through a curved slit, which is part of a circle.

In front of the analyser a system of five spherically shaped electrodes can be mounted, concentric with respect to the collision centre. With these a nearly spherical symmetric field can be produced, by which the scattered electrons are retarded without in principle deforming their trajectories.

A small Faraday cage which can be moved up and down pneumatically, is used to intercept and monitor the unscattered part of the primary beam in front of the entrance slit.

The analyser disperses the scattered electrons according to their energy and consequently only a small energy band is transmitted. The electrons leave the analyser again through a curved slit and impinge upon the front plate of the channelplate detector.

Gun and analyser are shielded against magnetic fields by a pair of concentric mu-metal cylinders.

2.2. Scattering geometry

In order to attain a high angular resolution, the beam must be focused to a small spot on the detector. The last lens of the gun, a three cylinder asymmetric zoomlens, performs this task. All electrons scattered out of the beam at an angle θ will be focused then in a narrow ring around the primary beam spot.

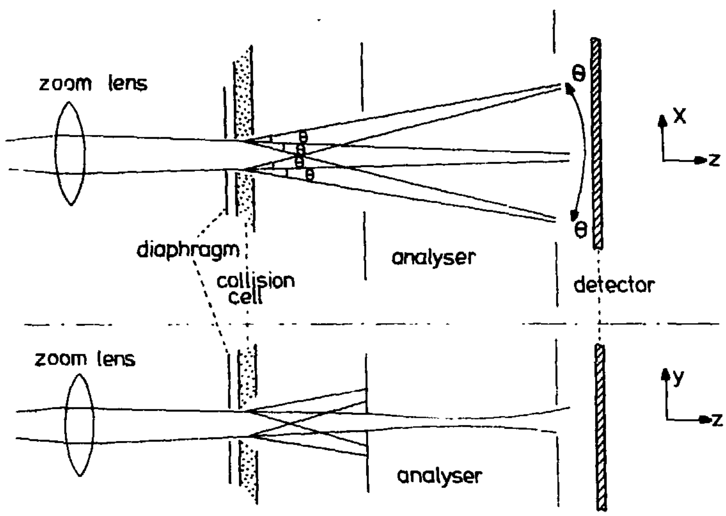

FIGURE 2

Schematic drawing of the scattering geometry as used in the present set-up. The XZ-plane along the analyser slits (fig. 2a) contains the scattering information, whereas perpendicular to the slits in the YZ-plane energy dispersion takes place (fig. 2b).

Clearly, the insertion of an analyser in between the scattering cell and detector will inevitably affect this focusing condition. However, it is not necessary to image the whole 2π azimuth onto the detector; a small fraction of it will suffice. So, if one could design an analyser, which does not change the angle of the trajectories of those electrons it accepts, still a high angular resolution is possible. A parallel plate analyser with a narrow entrance slit is well suited for this purpose, as will be shown in the following section.

Figures 2a and b show the scattering geometry. The XZ-plane is taken along the analyser slits and contains the unperturbed angular information, whereas in the YZ-plane perpendicular to the slits the scattered particles are dispersed according to their energy. The resulting angular and energy resolution will be discussed in section (3.3).

3. The analyser

3.1. Principles of operation

Basically, the electrostatic analysers of this type consist of two parallel plates separated by a distance d, with a retarding potential $(V_2 - V_1)$ between them, see figure 3. By inserting guard electrodes between the upper and bottom plate, the electric field can be made sufficiently uniform. In that case focusing takes only place in a plane perpendicular to the plates.

It is easily derived [10,11] that the distance L traversed by particles originating from the point O with energy E_o is given by:

$$L = (h_1 + h_2)\ \cot\alpha\ + 2d\ \frac{E_o}{V_2 - V_1}\ \sin\ 2\alpha \tag{3.1}$$

First-order focusing in α takes place if

$$(h_1 + h_2) = 4d\ \frac{E_o}{V_2 - V_1}\ \cos\ 2\alpha\ \sin^2\alpha \tag{3.2}$$

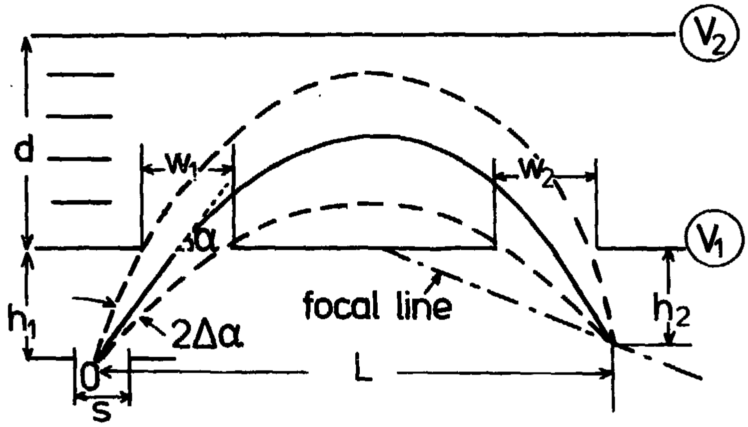

FIGURE 3

Principle of a parallel plate analyser.

The most widely used version of this type of analyser is the one where α is $\frac{\pi}{4}$ and $(h_1 + h_2) = 0$, so from eq. (3.1) L is given by

$$L = 2d \frac{E_o}{V_2 - V_1} \tag{3.3}$$

The entrance slit w_1 is then imaged with unit magnification on the exit slit. Green and Proca [12,13] showed that for $\alpha = \frac{\pi}{6}$ second order focusing is obtained, which allows the acceptance of large opening angles $\Delta\alpha$. The image points of particles emanating from 0 with different energies are located along a focal line outside the analyser in that case, whereas the source width s is magnified with a factor of 1.5. The horizontal distance L is then given by

$$L = \frac{3}{2}\sqrt{3}\ d \frac{E_o}{V_2 - V_1} \tag{3.4}$$

Eq. (3.3) and (3.4) show a simple linear relationship between L and the particles' energy E_o. The energy resolution of the instrument reflects this property:

$$\frac{\Delta E_o}{E_o} = \frac{w_1 + w_2}{L} \qquad \text{for } \alpha = \frac{\pi}{4} , \qquad (3.5a)$$

$$\frac{\Delta E_o}{E_o} = \frac{3s}{2L} \qquad \text{for } \alpha = \frac{\pi}{6} . \qquad (3.5b)$$

One would be inclined to judge the $\frac{\pi}{6}$ configuration superior for all applications, but actually three reasons led us to the choice of just the simpler $\frac{\pi}{4}$ angle of incidence.

The first is that especially at lower energies, i.e. $<$ 100 eV, it is difficult to focus an electron beam to a spot size less than say 0.75 mm. Since s in eq. (3.5b) represents the projection of this spot on the analyser plane, its image on the focal line will be three times larger than the actual beam size for a $\frac{\pi}{6}$ angle of incidence and thus forms a serious limitation to the energy resolution. On the other hand, one is rather free in the choice of $w_1 + w_2$, which restricts in the $\frac{\pi}{4}$ case the final resolution.

Secondly, since we are interested in the scattering angle too, it is essential to keep w_1 small to avoid the scattering angle to vary over the slit width, otherwise deconvolution of the final spectrum gets complicated. So $\Delta\alpha$ will be small and there is no gain in second order focusing.

Finally, in the $\frac{\pi}{6}$ case one has to focus the primary beam to a point in front of the analyser. Due to its divergence the beam will spread on its way through the analyser in the non-dispersive direction, where no focusing occurs. So its spot size at the detector will be out of focus along the line where the scattering angles are resolved. Consequently, the angular resolution will be severely reduced compared with the $\frac{\pi}{4}$ configuration.

In our application we make use of the one-dimensional energy dispersion property of the analyser, so the velocity component of the electrons perpendicular to the electric field

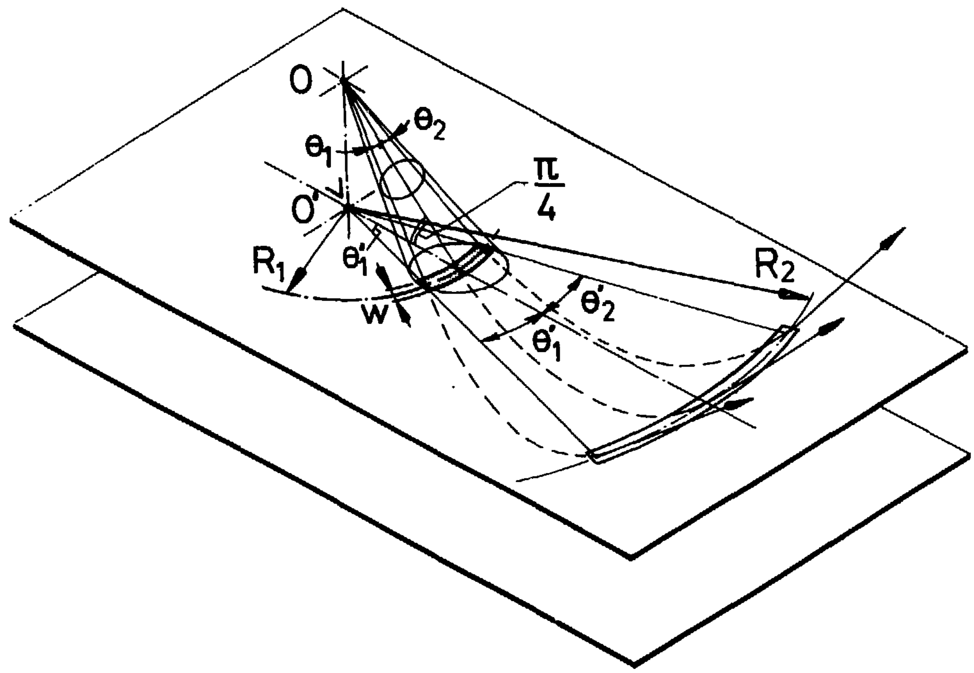

FIGURE 4

Detailed sketch of the scattering geometry, showing the trajectories of those scattered electrons, which are transmitted through the analyser.

is left unchanged during passage from entrance to exit slit. This makes a simultaneous measurement possible of the energy and angle of scattering of an electron coming from 0.

Figure 4 shows the scattering geometry in more detail.

The processes under study will result in cylindrically symmetric scattering cones around the primary beam axis with the polar angle $\theta_{1,2}$ as the relevant parameter. Only small sections of these cones will be transmitted through the entrance slit.

The question now remains as to the choice of the geometrical form of the analyser slits in order to disentangle the angular information from the energy dispersion. From eq. (3.1) it is clear that any electron entering the analyser under an angle α with respect to the plates will traverse a parabolic path, the length of which only depends on the kinetic energy of the electron. It can be seen from figure 4 that if the entrance slit is curved as a circle segment around the projection 0' of the scattering centre 0 on the analyser, this slit will transmit only those electrons, which lie on the surface of a cone with 0 as top and 00' as axis. The paths of the primary beam and scattered electrons can be visualized as lying in the leaves of a half-opened book with its back along 00'. So, independent of their angle of scattering θ, all these electrons enter the analyser under $\frac{\pi}{4}$ and leave it again under the same angle $\frac{\pi}{4}$ along a circle segment with radius R_2 and 0' as centre.

In this way the whole scattering process is fixed by its two-dimensional projection on the analyser front plate. One can easily derive the following relation for the projection θ' of the true scattering angle θ:

$$\theta' = 2 \sin^{-1} \sqrt{2} \sin \frac{\theta}{2} \approx \sqrt{2}\theta \qquad \text{for small } \theta \qquad (3.6)$$

As a result, the scattering angles are distributed along concentric circles, the radii of which are determined by the ratio of the energy of the particle over the electric field between the analyser plates.

If the exit slit width is taken larger than the entrance width w_1, it will fully transmit the elastic signal. The solid angle, under which a scattered electron sees the analyser is determined in that case by w_1 only. A direct consequence of the curved slit geometry is that the solid angle subtended by the entrance slit appears to be equal for all angles of scattering in the small transmitted angular range (i.e. $-10° < \theta < 10°$). Indeed, from figure 4 it is clear that the projection ΔA of part of the slit, in the interval $\Delta\theta'$, onto a sphere with 0 as centre and distance D to the slit as radius, is independent of the particular value of θ':

$$\Delta A = \tfrac{1}{2}\sqrt{2}\ \ w_1\ \ \tfrac{1}{2}\sqrt{2}\ \ D\ \Delta\theta'\ . \tag{3.7}$$

This yields for the solid angle $\Delta\Omega$ the simple result:

$$\Delta\Omega = \frac{\Delta A}{D^2} = \frac{\frac{1}{2}\ w_1\ \ \Delta\theta'}{D} \tag{3.8}$$

Thus no correction factors are needed for the effective solid

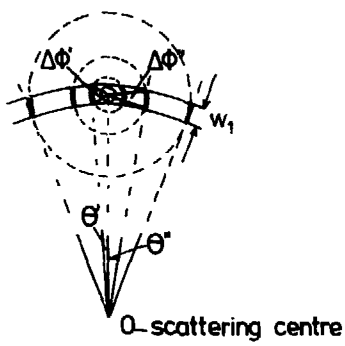

FIGURE 5

Simple drawing, showing the variation of the scattering cone azimuth $\Delta\phi$ over the entrance slit width as a function of the scattering angle θ.

angle as a function of the scattering angle, which can be quite an elaborate task to determine in other experimental arrangements, particularly for small angles [14].

The latter statement is only true if the intersections of the scattering cones with the entrance slit width form straight lines. From figure 5 it can be seen that these are always curved, but the curvature may be neglected at already rather small scattering angles. Indeed, with an entrance slit width of 1 mm one finds a deviation from a straight line of less than 1% at angles $> 1.5°$. For smaller angles narrower slits are necessary.

3.2. Construction

For two reasons we choose for a compact design (160 * 110 * 45 mm): i) especially for low energy electrons, the path lengths before reaching the analyser should not be too long in order to minimize the influence of stray fields, and ii) the scattering pattern should not spread out too much, otherwise the exit slit cannot be covered with commercially available channelplates.

Construction details are given in figure 6. The analyser front is part of an aluminum block (A), through which two large openings (B, 40 * 16 mm and C, 80 * 25 mm) have been milled. The entrance and exit slits were spark eroded in 0.2 mm thin molybdenum plates, which are screwed at the inside over these holes. The distance from centre to centre of these slits is 80 mm. The analyser back plate (D) is held fixed, together with four equally spaced guard plates, on ceramic rods. These plates, all of molybdenum, are 0.5 mm thick. The gap distance between front and back plate is 25 mm. A 1 mm hole in the back plate enables a careful alignment with a laser beam.

All parts which the electrons can hit have been coated with aquadac to avoid local accumulation of charge.

The whole block is mounted on a ceramic base plate (E), so it can be set off ground potential, necessary if retardation is used.

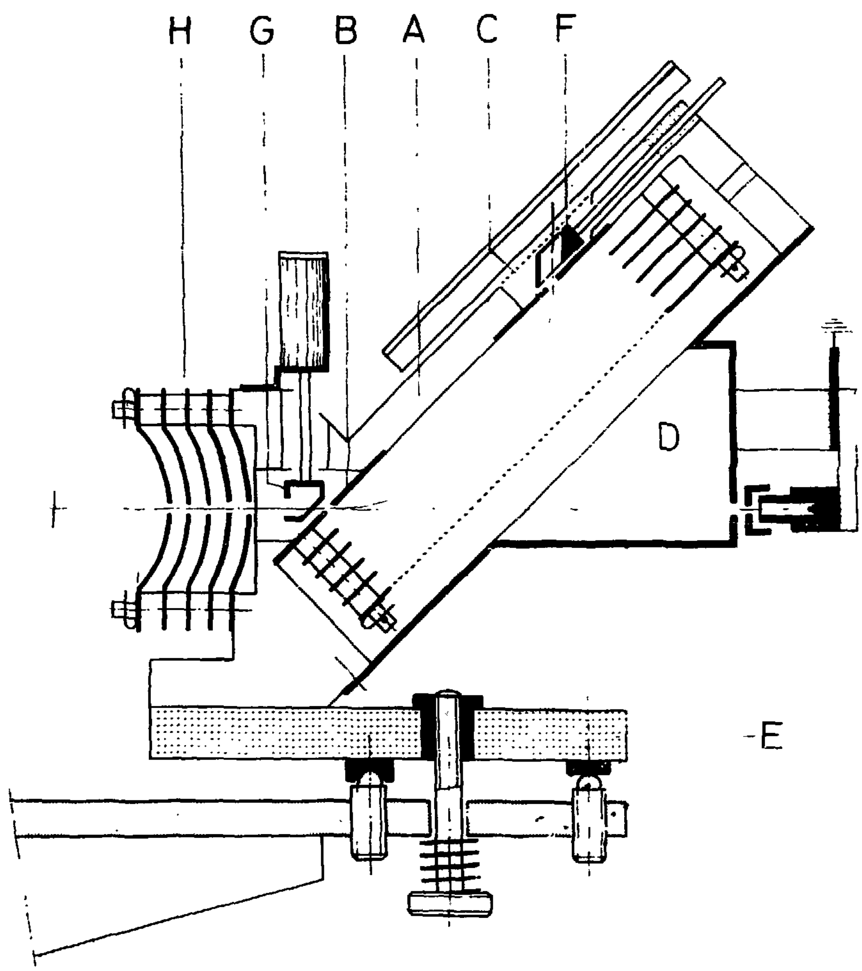

<u>FIGURE 6</u>

Construction details of the analyser (for explanation of parts, indicated by letter indices, see text).

The thickness of the analyser front plate (10 mm) leaves enough space for the installation of a small box-like Faraday cup (F) between exit slit and channelplates. This cup has been spot welded on a 1 mm thin thermo-coax cable in such a way, that the inner wire reaches into the cup. Biasing this wire positively with respect to the cup walls prevents secondary electrons to escape from it. However, this cup can only be used if the primary beam width is small enough for collision free entrance into the analyser, otherwise a flooding with secundary electrons occurs. This is certainly not the case with narrow slits at low beam energies. Therefore we installed a second box-like Faraday cage (G) just in front of the analyser, which can be moved up and down pneumatically.

Both cups are held at the same potential as the analyser front.

3.3. Resolution of the instrument

At this point, some characteristic details about the electron optics have to be given. A small diaphragm of 0.1 mm in the gun restricted the pencil angles of the beam electrons. In this way, chromatic aberrations are kept small, especially at low beam energies (see Blaauw et al. [9]). The image of this stripper, about a factor of 5 magnified, stays nearly fixed in the collision region when varying the beam energy. One can treat it as exit pupil for the further ray tracing behind the collision centre, see figure 7 (and also figures 2a and b). The anode aperture of 0.2 mm in the gun extraction region was focused on the channelplates with about unit magnification.

In order to calculate the angular resolution of the instrument, a closer inspection of the beam transport mechanism through the analyser is necessary. As mentioned before, the analyser possesses first order focusing properties only in planes perpendicular to the slits, i.e. in the radial direction as indicated in the figure, but not in the tangential direction. Therefore, the pencil angles $\Delta\beta$, which the elec-

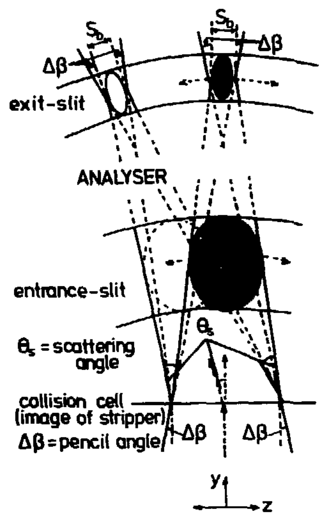

FIGURE 7

Projection of the scattering geometry on the analyser front plate. The angular resolution is determined by the beam spot size at the exit slit in the non-dispersive X-direction, whereas the energy resolution depends upon the beam size at the entrance slit in the Y-direction.

trons make with respect to the beam axis along the entrance slit will not be altered during passage through the analyser. As a result, the size of the beam spot along the exit slit will be the same as when no analysing field was present at all.

Focusing the beam to a small spot on the channelplates yields the best angular resolution attainable with this set-up; it is then given by s_b/L_{tot}, where s_b is the spot diameter (more precisely, the minor axis of the elliptical spot) and L_{tot} the path length traversed from the collision centre to the channelplates.

The beam divergence, if small (which is the case here), has no limiting influence and, as seen from figure 7, the resolution $\Delta\theta_s$ is the same for all scattering angles θ_s.

With respect to the energy resolution the situation is quite different. The analyser focuses the width of the beam in the radial direction with unit magnification from entrance to exit slit. Either the width of the entrance slit or the size of the beam projected onto this slit, which of the two is larger, determines the image size on the exit slit and thus according to eq. (3.5a) the energy resolution. Clearly, in both cases the shape of the spot will be elliptical.

4. Detector and data management

4.1. Detector

Each individual particle passing the exit slit is amplified by two channelplates (Galileo Electro-Optics Corp.) to a level suitable for counting electronics. The two plates (diameter 86 mm, channel pitch 25 µm, thickness 1 mm and bias angle $\beta = 8°$) were mounted in a chevron arrangement, prescribed in order to reduce afterpulsing due to ionic feedback [15]. The plates are separated at the edge by a thin mylar ring, 250 µm thick, which makes it possible to apply a bias voltage in between. By variation of this voltage together with those over the plates a narrow high gain pulse height distribution can be established [16]. Typical values we found were 300 V bias and 950 V over each plate, resulting in a ratio of the top of the charge distribution to its FWHM of 90 - 120% and mean charge ≈ 1 pC per pulse.

After amplification, the charge cloud is registered on a collector plate. To reduce the necessary measurement time, countrates of a few kHz must be processable by this plate and subsequent electronics without pulse pile-up. Two types of collector plate have been constructed, a simple concept for one-dimensional and a more sophisticated one for two-dimensional position analysis.

4.1.1. *One dimensional position measurement*

An interpolating multi-anode system, consisting of equidistant copper strips which are interconnected by capacitors and resistors, is the simplest way to achieve this [17]. Only two charge amplifiers are needed, one at each end of the capacitor string, to appoint the centroids of the charge cloud.

An advantage of this system is the freedom one has in accommodating the structure of the strips to the particular form in which the scattering information arrives at the collector. In our case part of a circular pattern is detected, so it is

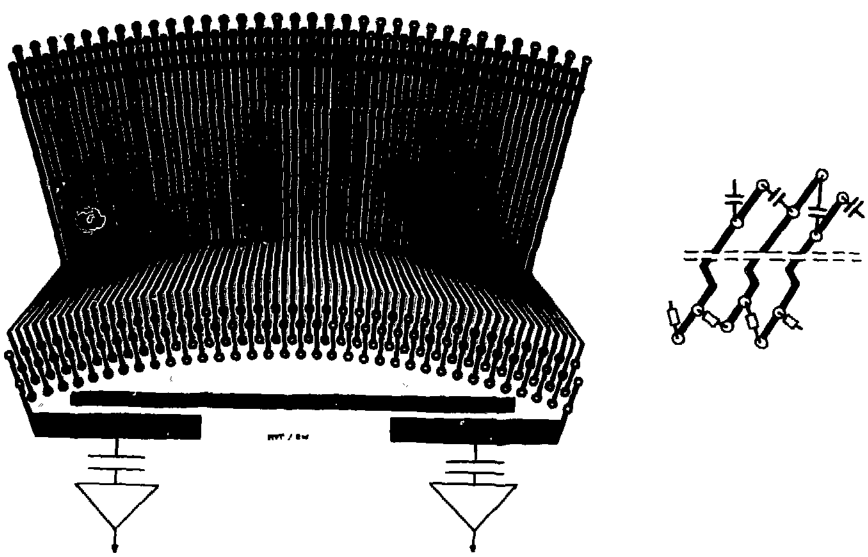

FIGURE 8

Anode for one-dimensional read-out.

obvious to arrange the strips along rays coming from the projection of the collision centre on the analyser front plate. Figure 8 shows this pattern foto-etched on an epoxy printing board, altogether 68 strips.

The resistors in the chain were taken 100 kΩ, whereas the capacitors were chosen 820 pF, resulting in a total chain capacity of 15 pF. The charge sensitive amplifiers (Canberra 2004) produce about 10^{-15} C of charge equivalent noise (FWHM), only .1% of the mean charge generated by the MCP's, so in principle a position resolution of .1% FWHM of the full range can be obtained. This figure of merit is highly sufficient for our measurements, where the angular resolution is limited by the beam spot size, typically 0.3 mm or larger over a full range of 70 mm (thus $> 1/250$ FWHM).

Just behind the back of the second channelplate a thin (0.3 mm) mask was inserted with a window in the form of a broad circle segment covered with a fine (1000 l/inch) gold mesh grid. This grid induces a further broadening of the charge cloud before reaching the detector plate at a gap dis-

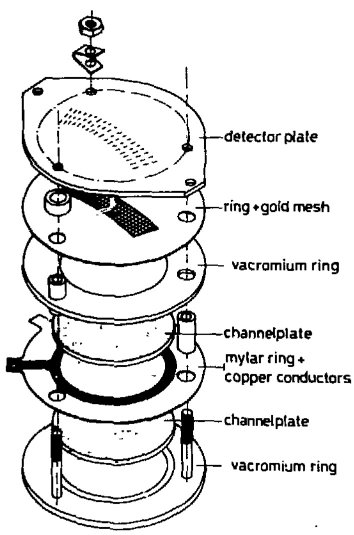

FIGURE 9

Construction of the detector, containing the two channelplates.

tance of 3 mm. This, together with an adjustable accelerating voltage guarantees the charge footprint to cover at least 3-5 strips in order to smooth out any gridlike structure in the final position spectrum. Figure 9 shows the construction of the detector.

The plates are clamped between two vachromium rings, which are centered by three thin bolts welded on the bottom ring. Mylar rings and Al-oxyde tubes are used where insulation is required. The contacts with the plates are made with thin copper foils. The anode and fitting rings are pressed together by springloads.

4.1.2. *Two-dimensional position measurement*

An alternative anode concept has been designed for this purpose, based on the wedge and strip configuration, first

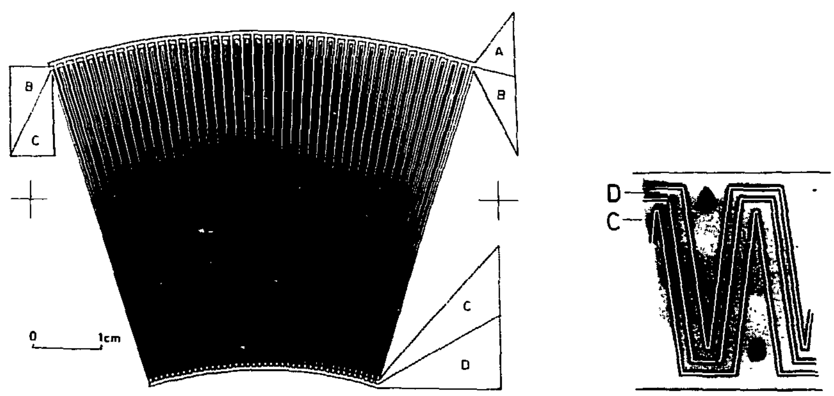

FIGURE 10

Anode for two-dimensional read-out. The inset shows the four electrode geometry in one unit cell.

proposed by Anger [18]. It has been shown recently [19] that this principle is capable of high resolution, essentially distortionless encoding of rectangular position events into charge ratios. The wedges and strips are certainly not bound to a rectangular shape, but, as in the one-dimensional case, can be arranged in a polar coordinate form matched to our particular energy resolved scattering geometry. Figure 10 displays this pattern.

Two series of wedges A and B linearly encode the event position in the R direction, where the energy is dispersed, whereas a pair of conductors C and D zigzag between the wedges in such a way, that one decreases in width, while the other increases, both linearly, as they progress in the θ-direction.

In principle only one series of wedges would suffice, thereby saving one charge amplifier, but this would require a common subplane conductor with the attendant substrate perforations for each wedge separately.

Thirty-one elements were foto-etched in a 1 μm thin aluminum layer, with a 40 μm gap between the electrodes. Two broad conductor strips carry the charge away from the wedges to the amplifier inputs. Each wedge measures a maximum resistance of 500 Ω from its top to the conductor band. However, because of their length (≈ 6 m), the zigzag electrodes do give a substantial larger resistance to the charge transport. In particular, if the charge footprint lies at one end of the electrode, while it has to be collected at the other end, the electrons have to pass the full resistance of 4 kΩ, a nasty feature which easily leads to thermal noise. We could reduce this effect by simply connecting both ends of the zigzag electrodes together. Now the most unfavourable situation exists for the charge centroid lying half-way these electrodes: the electrons see towards both ends half of the electrodes' resistance in parallel, so effectively only one quarter of it. This quantity (< 1 kΩ) can be accepted by the amplifier input electronics.

The same mounting as for the strip anode can be used, but because of the larger size of one unit cell (≈ 2 mm) the gap between the anode and second channelplate must be at least 8 mm.

4.1.3. *Channelplate sensitivity*

In order to perform reliable relative as well as absolute measurements, the efficiency of the channelplates has to be determined. This mainly depends on the energy and angle of incidence of the impinging particle. Galanti et al. [20] measured the efficiency as a function of incident angle with a 1 keV electron beam and found a nearly flat behaviour between 10° and 20°, followed by a slow decrease at larger angles, see figure 11. They also looked for the response as a function of impact energy at a fixed angle. For electron energies in the range of about 200 - 700 eV this remained nearly constant, whereas below 100 eV a severe drop is generally observed.

Since the electrons leave the analyser under 45° along a circle segment, their angle of incidence with respect to the microchannels will only weakly change over the exit slit range. A simple calculation showed the variation in this angle to be less than 1°, provided that the bias angle of the microchannel-

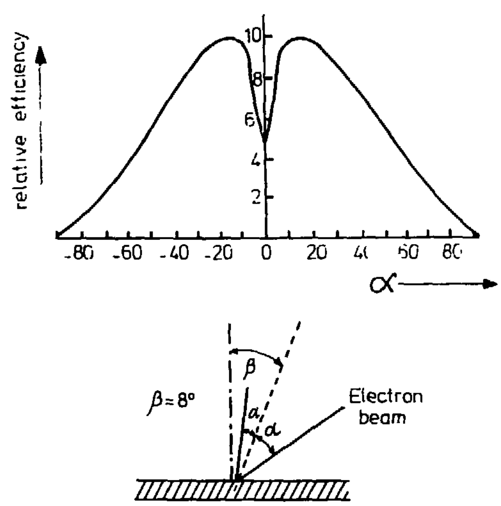

FIGURE 11

Relative efficiency as a function of angle of incidence [20]. The angle of incidence α is defined here with respect to the axis of the individual micro-channels.

plates (β in figure 11) is chosen to lie in the $\theta = 0$ plane. So, our configuration guarantees an essentially equal response for all the scattering angles at a fixed energy.

For measurements in the lower, i.e. $< \approx 200$ eV, impact energy regime postacceleration of the electrons is advisable before they hit the channelplate. For that purpose we mounted a second slit upon the analyser exit hole and biased the front of the first channelplate positively with respect to this slit. With this method of operation, the efficiency of our detection system indeed remained essentially constant while varying the energy from 15 to 150 eV. It was even possible to calibrate it absolutely, as will be discussed in section 5.3.

4.2. Electronics and data management

The electron cloud Q at angle θ is divided up by the capacitor chain into Q_1 and Q_2 at the respective ends of the detector, where they are decoupled from the high voltage on the plate to the virtual grounds constituted by the charge amplifiers. The signals from these are subsequently amplified by main amplifiers (ORTEC, model 575) and via a special purpose 'dynamic' amplifier (DA) fed into a 10 bit Dual ADC (0 - 10 Volt). The DA module amplifies the signals Q_1 and Q_2 further with a factor of 10 only if their sum pulse is less than 1 Volt. In this way a more economic use is made of the available 10 bits for the digital representation of the pulses, leading to a higher accuracy in the resulting number.

The output signals of the ADC are offered to a fast (400 ns per instruction) bitslice processor. This unit computes the position X of the particle according to:

$$X = Q_1 / (Q_1 + Q_2) \tag{3.9}$$

The resulting number is stored in the corresponding channel of a 1024-channel MCA. A display module transmits the data on line to a (Tektronics 604A) monitor scope, so one has a real time control over the measurement.

Preprocessor, ADC, MCA and display are all CAMAC controlled

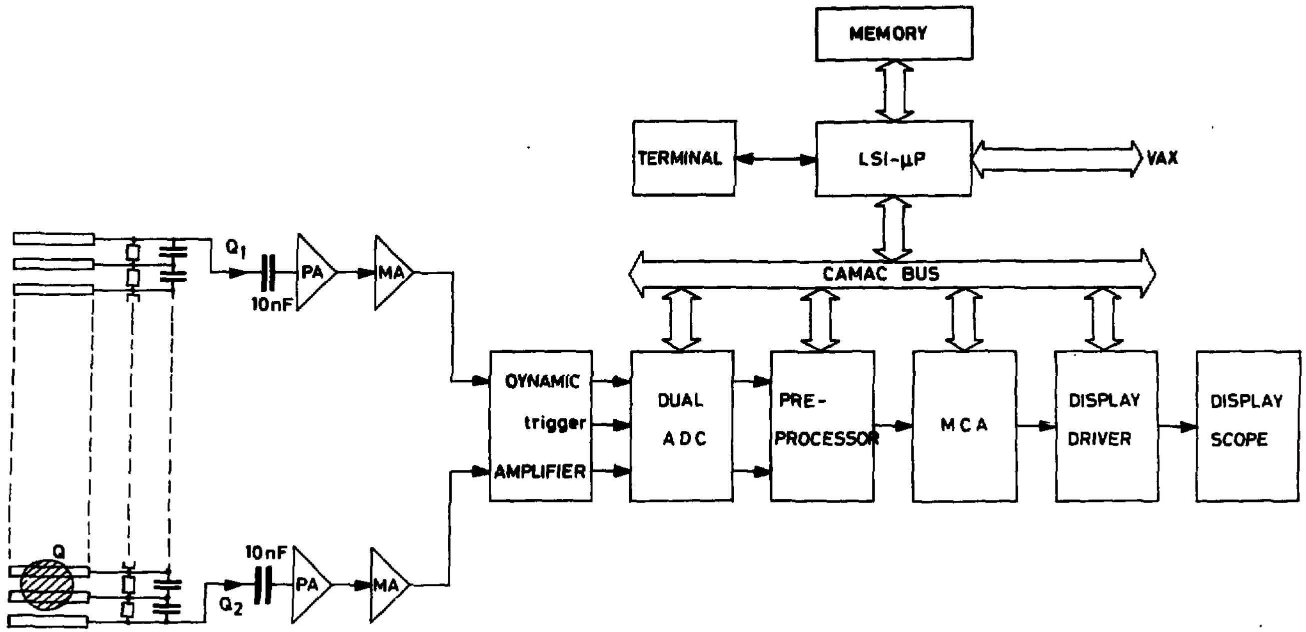

<u>FIGURE 12</u>

Schematic diagram of electronics and data acquisition system.

and interfaced with a LSI-23 microprocessor. This in its turn communicates with a VAX 11/750 computer system, where program developing and final data processing takes place. Figure 12 shows the set-up in block form.

5. Performance

The description sofar concerned the principles of the analyser and detector. However, before actual measurements can be carried out, a systematic test on their performance is necessary. We had to follow a two-step approach, in that first the detector response must be determined before one can start to investigate the analysers' properties. Since our primary aim formed the study of elastic scattering, we shall restrict the discussion to the one-dimensional read-out detection system.

5.1. Multi-anode detector and pulse processing system

5.1.1. *Linearity*

Although the chain capacitors (820 pF) between the anode strips were chosen large compared to stray capacities, typically 3 - 5 pF, their large number (68) can still cause appreciable leakage of charge if the cloud centroid lies near the edges. As a result, the simple linear relationship for the position as given in eq. (3.9) will no longer hold.

This effect has been checked by feeding each chain capacitor with a 1 pC pulse from a pulse generator and comparing their actual position with the one calculated by the preprocessor. In the MCA range corresponding with scattering angles between -8° and +8° the detector is linear, but towards the edges it displays a significant nonlinearity, see figure 13. By fitting a quadratic curve through these side regions, one can easily derive a correction formula for the real scattering angle as a function of the MCA channel number.

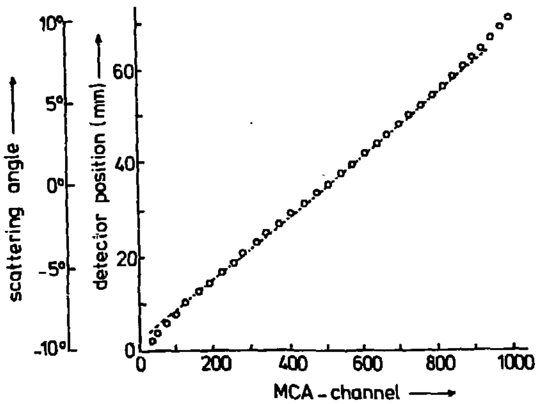

FIGURE 13

Anode response to equal pulses at its strips. The nonlinearity from the outermost strips can be clearly seen (the broken line is drawn to show the region of linearity).

5.1.2. *Resolution*

This feature is not only determined by the pulse processing electronics, but also by the size of the charge cloud as it arrives at the detector. So, the best way for testing it is to hit the channelplate surface in small localized regions. For that purpose we installed a thin foil consisting of spark eroded holes (70 μm) in between the exit slit and channelplates. A very low intensity, in order to avoid saturation of the channels, electron beam was scanned over these holes and the transmitted spots recorded. The choice of this hole size compared with the total detector area (70 mm) yields a 1/1000 resolution, large enough for our case.

We counted on the average an occupation of 4 out of 1024 MCA channels for the hole images, thus corresponding with a resolution of ≈1/250.

5.2. Analyser

5.2.1. *Transmission and energy resolution*

The slit widths have been chosen such, that only those electrons, which have undergone elastic collisions, are fully transmitted. With the help of a pair of horizontal and vertical deflection plates (length 15 mm and gap distance 10 mm) just behind the collision cell, we could test at any particular angle the transmission of a tiny electron beam by scanning the analysing field strength. This has been done for a whole range of impact energies. Figure 14 shows the results for an entrance slit width of 1 mm and an exit slit width of 2 mm.

Although a small deviation in field strength over the angular range was observed, we found at each energy enough overlap in the 100% transmission curves.

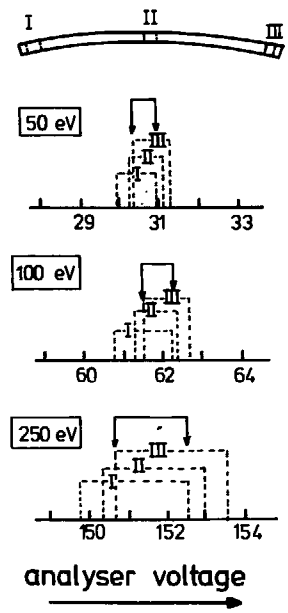

FIGURE 14

Analyser transmission at three spots of the exit slit as a function of the voltage between the analyser front and back plate. The two arrows mark the range of 100% transmission for the whole slit.

From the steep rise in the transmission curve sides one can deduce an approximate value for the energy resolution. With the particular choice of a 1 mm entrance slit it is indeed about 1/80 as predicted by eq. (3.5a). This can of course easily be enhanced by taking a narrower entrance slit.

5.2.2. *Linearity*

To test the linearity in angle, we replaced the exit slit by a series of equidistant small holes along the same circular segment. Again a tiny beam was scanned with the deflection plates over the entrance slit and the transmitted signal recorded. Taking the nonlinearity correction of the detector into account, we found a perfect linear relationship between scattering angle and deflection voltage. With a complete shielding of the space between collision cell and analyser against stray electric fields, this linearity pertained down to the lowest impact energies (15 eV) used.

5.3. Calibration

In section 4.1.3 we discussed the angle and energy dependence of the channelplate efficiency, where it was shown that the transmitted and thereby energy resolved particles hit the channelplate under practically the same angle. One should therefore expect an equal response of the detector at all scattering angles.

However, this will only happen if the channelplates possess a homogeneous sensitivity over their whole surface. More precisely, the gain factor in the delivering of pulses should not vary too much from channel to channel. As found by Macau et al. [21] and confirmed by accumulative experience in our institute, channelplates exhibit a decrease in gain during their first $10^7 - 10^8$ pulses, after which they enter a phase of stability. This period, characterized by a constant pulse height distribution, can last for up to $10^{10} - 10^{11}$ integrated counts.

Absolute measurements can only be done with channelplates operating in this regime, which can be reached quickly by illuminating the channelplate surfaces with a diffuse electron source, such as an ionization gauge, during some 30 hours.

We devised a simple method for testing the channelplate surface homogeneity as follows. A 1 kHz triangular sweep voltage was put on the deflection plates just behind the collision cell, thus transforming the primary electron beam into a shower of electrons. These will illuminate the entrance slit of the analyser uniformly, since for small deflection angles α the simple formula

$$\mathrm{tg}\ \alpha = c\,\frac{\Delta V(t)}{V_o} \tag{3.10}$$

holds and $\Delta V(t)$ changes linearly with time.

The preprocessor was loaded first with a program which displayed simultaneously the pulse height distributions of 4 conjugated areas on the channelplate. These distributions could be made equal in shape and well located within the upper and lower discrimination level of the peak detector, by adjusting the channelplate voltage and main amplification factor. The latter condition is essential for retaining a constant efficiency during the measurements.

Hereafter the preprocessor was run while calculating the position of the swept electrons and on the display appeared the near flat response curve as expected.

It must be stressed at this point that the sweep generator does not spread the beam electrons randomly over the entrance slit, but instead they pass it close to each other in short time intervals. The beam intensity should therefore be kept low to avoid pulse pile-up. A fast scope indicated when this critical level was exceeded.

It is even possible to calibrate the channelplates absolutely, if the beam intensity during sweeping is constant and exactly known and the proportionality constant c in eq. (3.10) has been determined. The latter could be easily found by tracing the position of the beam on the detector as a function of ΔV. We found for c an average value of 0.44, quite different from the ideal value of H/2D (.75 in our case), where H is the length and D the gap distance of the deflection plates. This ideal value will only be reached if $H \gg D$.

With a fixed beam intensity it is then a simple matter to calculate the number of electrons which have crossed a small part of the entrance slit during a certain time interval. The contents of the corresponding MCA channels divided by this number directly yield the required value for the efficiency.

6. Spherical retarding section

Since the energy resolution of the analyser is a fixed quantity given by the width of the slits and the distance between them, the final band pass energy ΔE can become too large at high impact energies in order to separate the elastic peak from inelastic contributions.

There are actually two ways to diminish ΔE in that case:

i) mechanically, by using narrower slits, and

ii) electrically, by retarding the particles before entering the analyser.

Procedure i) is the simplest to follow, but one should be cautious with it. For, the number of particles which will hit the slit edge and thereby scatter into the analyser can become substantial then with respect to those passing the slit directly. Consequently, the elastic peak will become broader due to these background particles, thus largely cancelling the gain in resolution. On the other hand, retardation has also its disadvantages, because it distorts the scattering geometry with inevitable stray fields. Fortunately, one can correct for this optical distortion, provided that about a factor of 0.2 in retardation is not exceeded.

With these considerations in mind, we chose for a combination of both methods in order to get ΔE small enough.

The design and optical properties of the retarding section, which we used for this purpose, will be discussed in the following subsections.

6.1. Design

In order to minimize the distortion of the scattering geometry, the retarding field lines have to be directed along the particle trajectories. Since these are radially scattered out of the collision cell, spherically shaped electrodes concentric around the interaction centre will fulfil this condition.

A package of five elements (H in figure 6) was mounted to realize a pure spherical electric field. They should be as thin as possible with respect to their mutual distance (5 mm). For that purpose an electroforming process was used, by which it was possible - in contrast to normal machining from bulk material - to make thin (0.2 mm) and yet stiff copper structures.

The radius of the first sphere R_1 is 30 mm, that of the last sphere R_2 50 mm.

Slits of equal width (4 mm) and increasing length (from 12 mm in no. I to 20 mm in no. V) were spark eroded in the electrodes in order to transmit the particles towards the analyser.

6.2. Optical properties

Although the electrodes have been made spherical in shape deliberately in order to minimize distortion of the scattering geometry, yet they will blur it severely, if one neglects two inherent optical effects. The first one concerns the virtual magnification of the beam at the collision centre due to Snell's law of refraction when the particles' velocity is reduced by the retarding field. The second effect is caused by the fringing fields at the slits of the first and last electrode. We shall investigate these two effects in detail here and indicate how one can, at least to some extent, compensate for them.

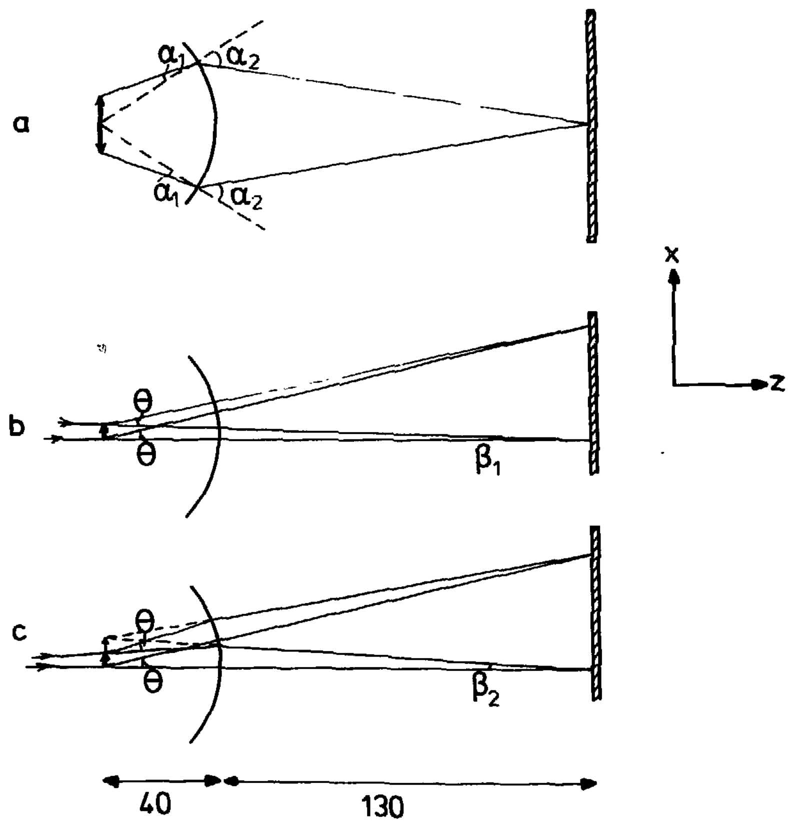

FIGURE 15

Showing refraction at the spherical surface (a) and how to compensate for it with the primary beam optics: (b) without retarding field, a converging beam, and (c) with retarding, a divergent beam is required.

6.2.1. *Refractive effects*

The following discussion is restricted to the situation in the non-dispersive plane of the analyser, i.e. the plane where the angular information is contained.

A basic drawback of the spheres is that only particles scattered from exactly the centre of the collision cell can escape along the radial field lines. In practice, one always deals with a small volume of scattering points, determined by the primary beam width. Assuming for the moment a perfect spherical field, it is easy to show that retardation, as indicated in figure 15a constitutes a positive lens. For, particles emanating from off-axis points will be refracted at the spherical surface (where we have replaced the five electrodes by one sphere to clarify the idea) according to Snell's law:

$$\sin \alpha_1/\sin \alpha_2 = \sqrt{V_2/V_1}.$$

Here V_2/V_1 is the ratio between the particles' kinetic energy behind and in front of the spheres respectively.

As a result, overfocusing will take place and the beam spot at the detector will become diffuse.

Clearly, this will happen just as well for particles scattered out of the beam over an arbitrary angle θ and thus the angular resolution will be reduced considerably.

However, by adjusting the primary beam with the gun zoom-lens, from a weakly converging to a weakly diverging one before it enters the retarding field, one can compensate for this overfocusing property. In this way, the unscattered as well as the scattered particles can still be brought to a focus at the detector. Figure 15b shows the normal situation when no retarding field is present, whereas figure 15c demonstrates the necessity for adjusting the primary beam if retardation is used (in this case with a factor of 4).

The net effect of retardation is to increase the product of spot size and pencil angle with $\sqrt{V_1/V_2}$ (according to Helmholtz-Lagrange's law). An increase in pencil angle (β_2 vs. β_1) is of no influence as long as we focus on the detector, only the spot size determines the angular resolution.

In the subjoint table this spot size is given as a function of (V_2/V_1), which we found experimentally at three different values of the beam energy, when appropriately focused.

TABLE I. Spot size (FWHM) in no. of MCA channels.

beam energy		200 eV	400 eV	800 eV
$\frac{V_2}{V_1}$	1.0	8	7	6
	0.75	9	8	6
	0.5	10	9	7
	0.25	12	11	9
	0.2	15	14	12

10 MCA-channels correspond with an angular width of 0.15°. The angular resolution decreases roughly with $(V_2/V_1)^{1/4}$, so before actually using retardation, the beam spot should match the required resolution amply.

6.2.2. *Fringing field effects*

An unavoidable disturbance in the spherical field is produced by the slits in the electrodes; particularly the first and last ones give rise to fringing fields. This will have its consequences on the particle trajectories, where both in the dispersive plane, i.e. perpendicular to the slits, as well as in the non-dispersive plane, i.e. along the slits, a change in their slope may be expected.

First we shall investigate what happens in the dispersive plane (the YZ-plane of figure 2b).

6.2.2.1. Ray tracing in the dispersive plane

The first and last slit separate regions with different field strengths and consequently induce a lens effect on the particle rays. The slits are relatively long with respect to their width, so to a first approximation refraction will only take place perpendicular to them. The rays will be refracted over an angle propertional to the distance to the centre of the slits, the well-known Calbick lens effect [22].

If the process under study concerns the energy and angle analysis of positive ions, one can cover these slits by fine meshed grids. In that case, each mesh acts as a separate lens and the resulting refraction will be minimal. However, in our experiment electrons carry the information and this will be blurred by the numerous secondary electrons from the grids.

Therefore, the lens effect at the first and last electrode slits together with the resulting off-radial motion in the spherical field will influence the electron trajectories. It is our aim here to assess the combination of these effects quantitatively.

The region between collision centre 0 and analyser entrance slit can at best be visualized as consisting of three parts as in figure 16: region I where no electric field is present, region II where the particles are retarded, and region III again field free.

The slit in the first electrode acts as a negative lens

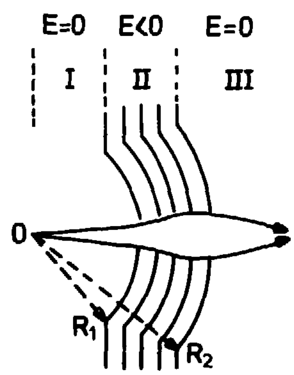

FIGURE 16

Calbick lens effect of first and last slit.

with a focal length given by [22]:

$$f = -\frac{2V_1}{E(R_1)} \tag{3.11}$$

where $E(R_1)$ is the electric field strength at $z = R_1$. We have taken for convenience the electron source at ground potential, so the primary beam energy equals eV_1 (the collision cell thus floats at potential V_1).

The slit in the last electrode however acts as a positive lens, with focal length:

$$f = +\frac{2V_2}{E(R_2)} \tag{3.12}$$

where $E(R_2)$ is the electric field strength at $z = R_2$.

It is easy to show that the spherical symmetric electric field between R_1 and R_2 is given by:

$$E(r) = \frac{V_2 - V_1}{R_2 - R_1}\,\frac{R_1 R_2}{r^2}\ ,\ R_1 < r < R_2 \tag{3.13}$$

r is the distance to the collision centre 0.

Due to the refraction at the first slit, the off-axis electrons will possess a velocity component perpendicular to the field lines as they enter region II. Only the component along the field will be retarded, and as a result their trajectory will be parabolic. Therefore the retarding field too plays the role of a negative lens.

Overall, the spherical electrodes form a system of three contiguous lenses, two negative and one positive; it depends upon the retarding ratio (V_2/V_1) if the system has a net converging or diverging power.

This overall behaviour can be revealed most appropriately by applying the formalism of the so-called transfer matrices [23]. In this method, the optical properties of each lens are expressed in a separate matrix, whereafter the product matrix yields the focal lengths and focal points of the combined system.

Since we are concerned with trajectories in a plane, (2×2)-matrices will suffice.

In the case of paraxial trajectories one can write then quite generally for the matrix relating the position and slope of a ray at the two sides of a lens:

$$\begin{pmatrix} y_2 \\ \\ y_2' \end{pmatrix} = \begin{pmatrix} -\dfrac{(z_2 - z_{PF_2})}{f_2} & \dfrac{(z_2 - z_{PF_2})(z_1 - z_{PF_1})}{f_2} + f_1 \\ \\ -\dfrac{1}{f_2} & \dfrac{(z_1 - z_{PF_1})}{f_2} \end{pmatrix} \begin{pmatrix} y_1 \\ \\ y_1' \end{pmatrix}$$

Here z_{PF_1,PF_2} are the positions of the focal points with $f_{1,2}$ as focal lengths. From these the location of the principal planes can be derived and so the optical properties are completely fixed by the matrix elements.

Since the width and slope of our beam are small, we are justified to transfer the above described paraxial matrix formalism to our problem.

For z_1 we take the position of the first and for z_2 that of the last sphere respectively; the centre of the spheres lies at $z = 0$.

It is a simple matter to find the matrix elements for the two Calbick lenses:

$$(I) : \begin{pmatrix} 1 & 0 \\ -\dfrac{E(R_1)}{2\,V_1} & 1 \end{pmatrix}, \qquad (III) : \begin{pmatrix} 1 & 0 \\ \dfrac{E(R_1)}{2\,V_2} & 1 \end{pmatrix}.$$

However, the computation of the matrix elements for the retarding field lens (II) is complicated due to the inverse-square dependence of the field (see eq. (3.13)). A rather lengthy calculation leads to the following result:

$$(II) : \frac{1}{\sqrt{V_2/V_1}+1} \begin{pmatrix} \dfrac{R_2}{R_1}\{\sqrt{V_2/V_1}-1\}+2 & 2(R_2-R_1) \\ \\ \dfrac{\{R_2\sqrt{V_2/V_1}-R_1\}\{\sqrt{V_2/V_1}-1\}}{R_1R_2\sqrt{V_2/V_1}} & \dfrac{2R_2\sqrt{V_2/V_1}-R_1\{\sqrt{V_2/V_1}-1\}}{R_2\sqrt{V_2/V_1}} \end{pmatrix}$$

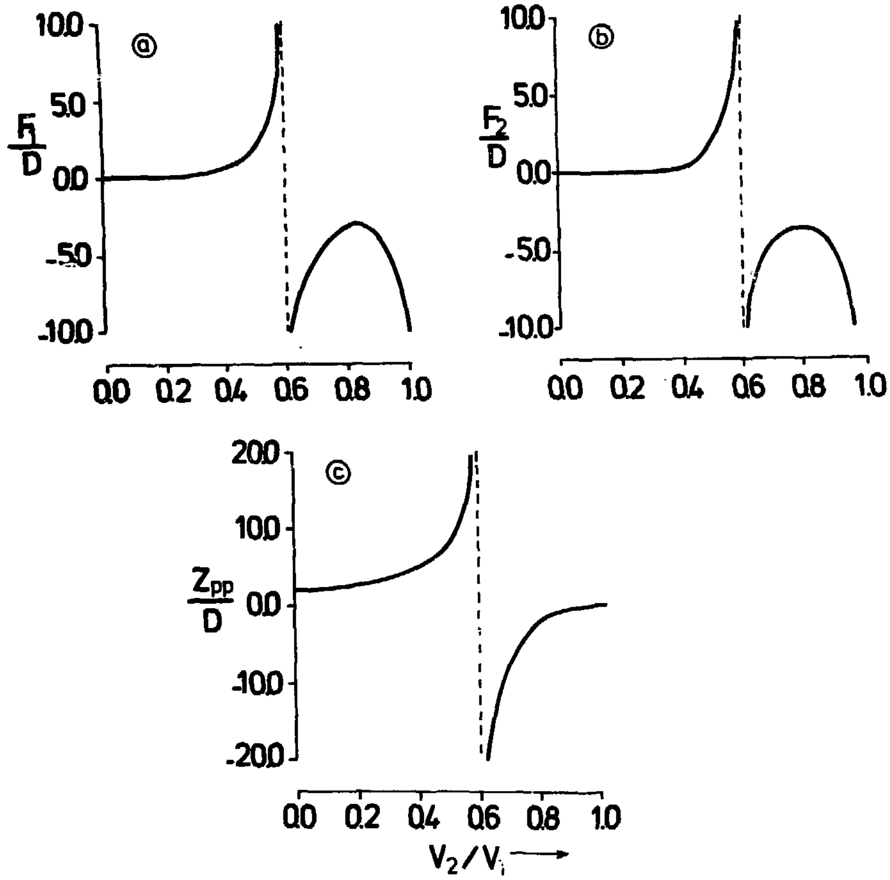

FIGURE 17

Lens properties of the spherical electrode system (with $R_2/R_1 = 5/3$) in the plane perpendicular to the slits. The focal lengths F_1 and F_2 as well as the location of the principal planes (all in units of $D = R_2 - R_1$) are shown as a function of V_2/V_1. The sign convention is the standard one [24].

By taking the product of these three matrices in the correct order (i.e. (III) × (II) × (I)), it is straightforward to find the focal lengths and principal planes as a function of the ratio (V_2/V_1).

For the ratio $(R_2/R_1) = 5/3$, table II gives the overall lens properties, normalized in units of $D = (R_2 - R_1)$.

Table II. Overall lens properties (in units of D)

Retarding ratio	Focal length F1	Focal point Z1	Focal length F2	Focal point Z2
0.950	-82.7515	82.5372	-80.6562	-80.8705
0.900	-46.5234	46.0234	-44.1359	-44.6359
0.850	-35.8026	34.9026	-33.0083	-33.9083
0.800	-32.2194	30.7194	-28.8179	-30.3179
0.750	-32.9112	30.4112	-28.5020	-31.0020
0.700	-39.2901	34.7900	-32.8724	-37.3724
0.650	-64.1296	53.6296	-51.7030	-62.2030
0.600	INF	INF	INF	INF
0.550	44.7123	-31.2123	33.1595	46.6595
0.500	18.9181	-11.4181	13.3771	20.8771
0.450	10.7171	-5.2171	7.1893	12.6893
0.400	6.8377	-2.3377	4.3246	8.8246
0.350	4.6438	-0.7438	2.7473	6.6473
0.300	3.2662	0.2338	1.7890	5.2890
0.250	2.3377	0.8766	1.1688	4.3831
0.200	1.6771	1.3229	0.7500	3.7500
0.150	1.1843	1.6490	0.4587	3.2920
0.100	0.7973	1.9027	0.2521	2.9521
0.050	0.4668	2.1241	0.1044	2.6953

First, at retarding ratios somewhat less than 1.0, the system behaves as a negative lens with a maximal diverging power at 0.8. At further retarding the system relaxes this defocusing, becomes neutral at 0.6 (exactly equal to the ratio (R_1/R_2)), whereafter it turns over into a positive lens. The principal planes shift thereby more and more towards the last sphere (see figure 17c).

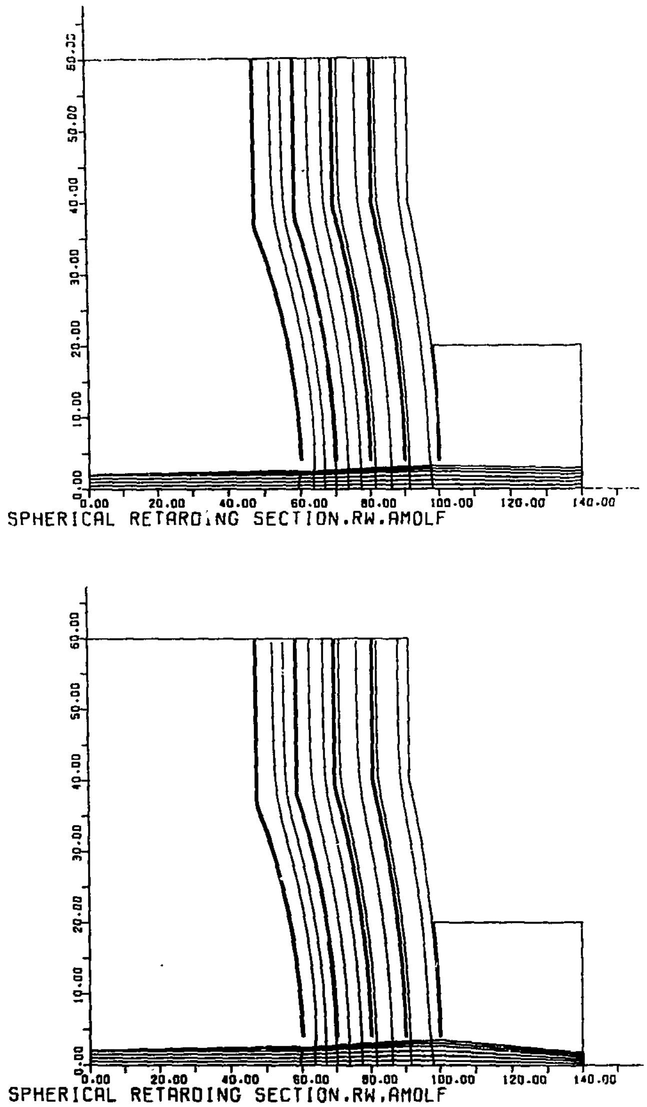

FIGURE 18

Computer simulated ray tracing from collision cell to analyser entrance slit. The equipotential lines and particle trajectories are shown for (a) $V_2/V_1 = 0.5$ and (b) $V_2/V_1 = 0.25$. Scale units are in 0.5 mm.

Taking into mind that the distance between the spheres and the detector is only 7D, it is clear that the diverging power of the spheres is too weak to influence the beam considerably, whereas its converging ability becomes problematic first at retarding ratios of about 0.2 or less.

This indeed we could confirm experimentally, where the flux of electrons on the channelplate stayed essentially constant while varying V_2/V_1 from 1.0 to 0.3, but where below 0.3 a steep increase in flux was found.

Another rough check on the correctness of the former calculations could be performed numerically with the help of a multi-purpose computer program [25]. This program is able to calculate equipotential lines and particle trajectories for all those electrode configurations, which can be reduced into two independent coordinates. Spherical surfaces are easy to handle as such, but in our case the azimuthal symmetry is broken by the rectangular slits.

Nevertheless, if the spheres are transformed into cylindrical surfaces with infinite long slits, the system can be accepted as input. Figure 18 shows a typical plot for V_2/V_1 = 0.5 and 0.25, where the rays are traced from collision centre to analyser entrance. As found analytically, only a weak focusing occurs at $V_2/V_1 = 0.3$, whereas the lens becomes quickly stronger at further retarding.

6.2.2.2. Ray tracing in the non-dispersive plane

The fringing of the field through the slits will also modify its pure spherical shape in the non-dispersive plane. One may expect the equipotential surfaces to flatten a bit along the slits, as indicated in figure 19.
Consequently, their geometrical centre appears to lie further away than the collision cell. The scattered particles can no longer follow the field lines exactly, and, according to the same reasoning as followed in section 6.2.1, their trajectories will bend outwards.

To simulate this effect analytically or even numerically is a nasty problem, because it will depend on the specific

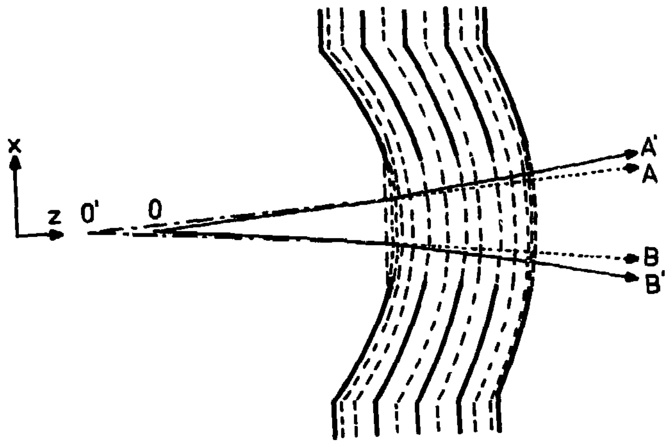

FIGURE 19

Sketch of equipotential lines (---) in the non-dispersive XZ-plane. Due to the lengths of the slits, the lines will flatten a bit over the first and last slit, leading to an apparent shift of their centre from 0 to 0'. As a result, rays OA and OB will bend towards OA' and OB'.

slit geometry and thus would require a three-dimensional treatment.

On the other hand, it is much easier to investigate empirically. For that purpose we replaced the collision cell by a set of horizontal and vertical deflection plates, such that their midpoint coincided with the collision centre. In that way real scattering trajectories could be simulated by deflecting a tiny, low intensity primary electron beam. At a fixed deflection voltage, corresponding with a specific scattering angle, we checked the position of the beam on the detector as a function of V_2/V_1. The results are given in figure 20. The system acts as a perfect negative lens, for the shift in position increases linearly going from small to large angles. Besides, the shift is directly proportional to V_2/V_1.

No dependence was found from the various impact energies used, so this extra refraction is wholly fixed by the specific value of V_2/V_1.

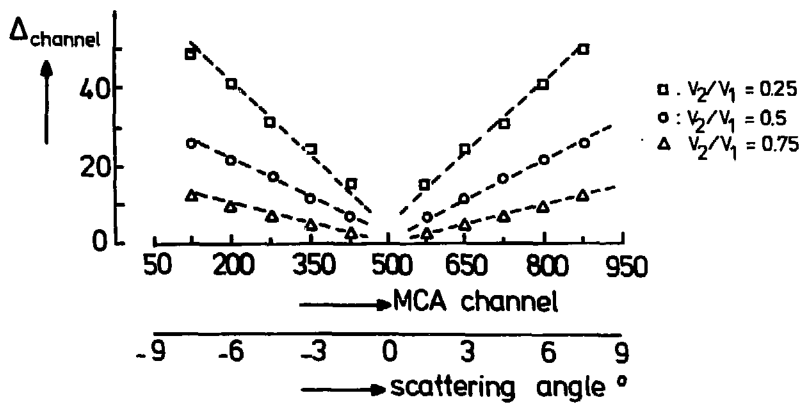

FIGURE 20

Lens property in the nondispersive XZ-plane as a function of V_2/V_1. From the shift in number of MCA-channels over the angular range it appears that the system behaves as a perfect negative lens.

The deformation is just a stretching of the scattering pattern as it arrives at the detector and can therefore easily be converted into the correct one with the help of figure 20.

Summarizing, application of this spherical retarding system indeed leads to the desired enhancement in energy resolution. With a broad focusing range of the primary beam optics and small spot size, still high angular resolutions are obtained. Unless excessive, i.e. $V_2/V_1 < \approx 0.2$, retardation is used, the influence of the slits on the energy resolution is negligible, whereas it stretches the angular distribution in a well defined way, dependent on the specific V_2/V_1 value.

7. Results and discussion

Figure 21 shows a typical spectrum for the angular distribution of electrons colliding elastically at argon at 200 eV. The correction formula as discussed in section 5.1.1 has been applied to obtain the right scattering angles.

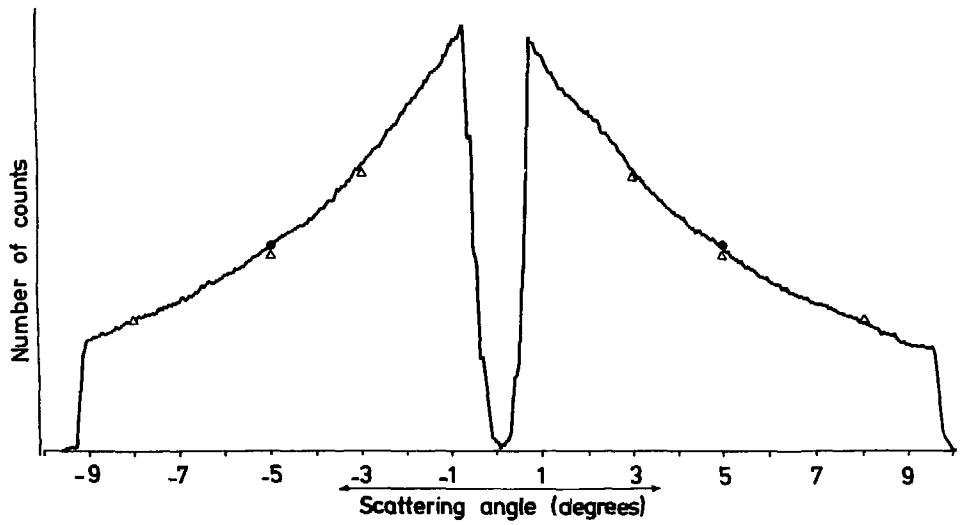

FIGURE 21

Intensity distribution for electrons, elastically scattered from argon at 200 eV impact energy. The data have been normalized on Bromberg [27] at 8° scattering angle. Δ : Bromberg, ● : Jansen et al. [26].

The dip in the centre is the shadow of the primary beam cup in front of the analyser, in this case 1.2 mm wide. It limits the minimal scattering angle to about 0.8°.

The position of the zero scattering angle is found with a simple least square routine as the point of symmetry between both sides. This could be compared with the location of the strongly attenuated beam centre on the channelplate just before and after the measurement. If these differed more than 0.1° (i.e. 5 MCA channels) among each other, the measurement was rejected.

The data have been corrected for the nonlinearity at the edges of the detector by dividing the raw spectrum by a sweep spectrum taken with the same setting for the analyser voltage. This procedure is only allowed if the statistical spread in both spectra is small, i.e. a large number of counts collected in each channel. At least 1000 counts per channel are required in order to reduce the statistical error to less than 4%. On the average, 300 - 400 s were needed to reach this criterion.

The displayed spectrum is relative, but by monitoring the beam current (which is done by a computer controlled ADC) and calibrating the detection efficiency as described in section 5.3, we can put the results on an absolute scale.

This high energy spectrum was taken deliberately in order to make comparison possible with the already existing data of Jansen [26] and Bromberg [27], who applied both an angular scan technique. Normalizing their results with ours at 8° we found an agreement within 3%. The slope in our data is slightly steeper than in Bromberg's results; this was also found at higher impact energies. It manifests itself only at the smallest angles of overlap, i.e. $\approx 2-5°$, where the angular scan method is hardly feasible anymore.

Concluding we may say, that the satisfactory agreement with other groups at overlapping impact energies shows how appropriate our novel technique is for small angle scattering experiments. Its design is not restricted to electron-atom scattering, but is just as well applicable for the investigation of ion-atom collisions.

Acknowledgements

The author wishes to thank Dr. J.G. Bannenberg, Dr. A.J. H. Boerboom, Prof. J. Los and Ing. E. de Haas for their valuable suggestions during the design phase, and Mr. W. Barsingerhorn for the skilful way in which he constructed the analyser.

References

[1] Geiger J and Moron-Leon D, Phys.Rev.Lett. 42, 1336 (1979).

[2] Pauty F, Matula G and Vernier P J, Rev.Sci.Instr. 45, 1203 (1974).

[3] Wijnaendts van Resandt R W, den Harink H C and Los J, J.Phys.E: Sci.Instr. 9, 503 (1976).

[4] Wijnaendts van Resandt R W and Los J, Book of Progress Reports of the XIth ICPEAC, North Holland Publ.Comp., pp.831 (1980).

[5] Weeks S P, Rowe J E, Christman S B and Chaban E E, Rev.Sci.Instr. 50, 1249 (1979).

[6] Van Hoof H A and van der Wiel M J, J.Phys.E: Sci.Instr. 13, 409 (1979).

[7] Smeenk R G, Tromp R M, Kersten H H, Boerboom A J H and Saris F W, Nucl.Instr.and Meth. 194, 625 (1982).

[8] De Bruyn D P and Los J, Rev.Sci.Instr. 53, 1020 (1982).

[9] Blaauw H J, Wagenaar R W, Barends D H and de Heer F J, J.Phys.B: Atom.Molec.Phys. 13, 359 (1980).

[10] Harrower G A, Rev.Sci.Instr. 26, 850 (1955).

[11] Yarnold G A and Bolton H, J.Sci.Instr. 26, 38 (1949).

[12] Green T S and Proca G A, Rev.Sci.Instr. 41, 1409 (1970).

[13] Proca G A and Green T S, Rev.Sci.Instr. 41, 1778 (1970).

[14] Kuyatt C A, in Methods of Experimental Physics, volume 7, Part A, ed. L. Marton, Academic Press, pp. 1-43 (1968).

[15] Colson W B, McPherson J and King F J, Rev.Sci.Instr. 44, 1694 (1973).

[16] Wiza J L, Nucl.Instr.& Meth. 162, 587 (1979).

[17] Gott R, Parkes W and Pounds K A, IEEE Trans.Nucl.Sci. 17, 367 (1970).

[18] Anger H O, Instr.Soc.Am.Trans. 5, 311 (1966).

[19] Martin C, Jelinsky P, Lampton M, Malina R F and Anger H O, Rev.Sci. Instr. 52, 1067 (1981).

[20] Galanti M, Gott R and Renaud J F, Rev.Sci.Instr. 42, 1818 (1971).

[21] Macau J P, Jamar J and Gardier S, IEEE Trans.Nucl.Sci. 23, 2049 (1976).

[22] Klemperer O, Electron Optics, Cambridge Univ.Press (1953).

[23] Di Chio D, Natali S V and Kuyatt C E, Rev.Sci.Instr. 45, 559 (1974).

[24] Harting E and Read F H, Electrostatic lenses, Elsevier Publ.Comp. (1976).

[25] Herrmannsfeldt W B, Electron Trajectory Program, Report SLAC 266, Stanford (1979); modified by van Bommel P J M, internal FOM report (to be published).

[26] Jansen R H J, de Heer F J, Luyken H J, van Wingerden B and Blaauw H J, J.Phys.B: Atom.and Molec.Phys. 9, 185 (1976).

[27] Bromberg J P, J.Chem.Phys. 61, 963 (1974).

CHAPTER IV

Absolute differential cross sections for elastic scattering over small angles from noble gas atoms

Abstract

Measurements of the absolute differential cross section for elastic electron scattering from the noble gases using a new simultaneous energy and multichannel position sensitive technique are presented. The range of electron energies is 20 - 100 eV, the range of scattering angles 1 - 10° and the angular resolution of both the primary and scattered electrons better than 0.25°. The accumulated signals have been made absolute to within 7% by carefully determining all the relevant parameters as primary beam intensity, gas density and collision length, analyser transmission and channelplate efficiency. An extensive account of the various existing theoretical models is given and a comparison is made between these calculations and the present results. The best agreement was found with the R-matrix calculations of Fon et al., although these systematically underestimate the experimental results for helium and neon at the intermediate energies. This discrepancy demonstrates the inadequacy of one single pseudostate to allow for polarization and absorption. A hitherto unknown structure in helium has been revealed, when the impact energy was scanned in a narrow range around the threshold for ionization. Its typical cusp shape and location on the energy scale indicates an accumulative effect, caused by the opening up of many high Rydberg states and the continuum.

1. Introduction

This chapter deals with the measurement and interpretation of differential cross sections for elastic scattering on noble gas atoms. It was our aim to obtain accurate experimental values for this cross section at angles as small as possible in order to extrapolate it to the experimentally inaccessible zero angle. This quantity we need as the second input parameter - besides the total cross section - for testing the forward dispersion relation.

Sofar, absolute small angle scattering measurements have been carried out by other groups only above 100 eV. Below 100 eV impact energy the existing data do not cover angles smaller than 15° - 20°, with some exceptions for helium and neon, where values at 10° have been reported. These angles are in general not small enough to support a reliable extrapolation.

Over the last five years, larger computer facilities and more sophisticated models enabled theorists to probe the intermediate energy regime in depth. As already stated in the introductory chapter, the most recent calculations still predict rather different values for the cross section at forward angles. This is mainly due to an insufficient assessment of the coupling effects between the elastic and the open inelastic channels, which can be particularly strong at these energies.

Therefore, our measurements have a twofold objective: first to test the dispersion relation, which will be undertaken in the next chapter. Then to provide accurate data sets, which can serve as standards for checking the achievements of present and future calculations. The latter forms the subject of the present chapter.

The chapter is organized as follows. Since a good understanding of the various theories is indispensable for a critical comparison of the calculated cross sections with our experimental results, section 2 comprises a rather extensive review of the relevant models. Emphasis will lie upon the often formidable computational problems one is faced with when entering the intermediate energy regime. Section 3 outlines the experimental procedure we followed for the measurements with the equipment as described in the previous chapter. In section 4 a detailed discussion of the results is given in relation to the existing theoretical models. A hitherto unknown structure in the cross section of helium, and to a lesser extent in neon, was observed, when scanning the impact energy over the thresholds for ionization of these atoms. We shall indicate that the existing theoretical calculations were inherently unable to predict this effect just because of their approximative character.

2. Review of theory

For the description of elastic and inelastic electron scattering by atoms one usually discerns three intervals of impact energy: the low energy range, well below the ionization threshold, where only a limited number of channels are open, the intermediate energy range, stretching from the inelastic thresholds to energies a few times the ionization energy, and the high energy range, where the Born approximation is believed to yield fairly accurately results. It should be noted here, that because of its purely real character, the first Born approximation never can correctly describe elastic differential cross sections in the forward direction (this is readily seen from the optical theorem, eq. (1.4), where the nonzero total cross section is related to the imaginary part of the forward scattering amplitude).

Quite generally, two lines have been followed for solving the scattering problem, the low and the high energy approach. The former ones resulted in a class of models, most of which are based upon eigenfunction expansion techniques, whereas the latter ones are more or less extensions of the first Born approximation.

Having settled the problem satisfactorily at the extreme sides of the impact energy scale, the theorists saw themselves confronted with the difficult task to clarify the intermediate energy regime, which is characterized by many channels being open and by the necessity of taking into account couplings to many atomic eigenstates. Over the last 10 - 15 years, experimental techniques have been developed which have allowed the absolute measurements of the differential (in angle) cross section for both elastic scattering and for discrete excitation. The existence of these measurements has been of great help for the theoretical studies, which indeed achieved appreciable success in the intermediate energy range.

However, there are still some problems unsolved, as recently summarized by Walters and Kingston [1], when pushing the high energy models downwards and the low energy models upwards in impact energy. In particular, for the elastic scattering at small angles the theoretical results still deviate strongly from each other. This is mainly due to the problem of how many channels and phase shifts have to be included in the calculations for the exchange and absorptive part of the interaction potential. Comparison could be made sofar only with the extrapolated values of the scarce experimental data, which extend down to only 10 - 15°; our measurements have filled this gap now and it is to be expected that they offer more support to the understanding of the long range electron interactions.

It is by no way our purpose here to treat in detail all the existing models. For this we refer the interested reader to the various excellent reviews which have been published over the last five years on this subject [2,3,4]. Rather, we shall indicate the typical problems which one encounters in applying these models at the intermediate energies. For this purpose, marking off their essential features will suffice†.

2.1. The low-energy approach

2.1.1. *The close coupling method*

Let us consider the scattering of an electron by an N-electron target atom (or ion). Most of the approximations used at

†Atomic units are employed throughout, i.e. $h = m_e = e = 1$.

low energies are based upon expansion series for the total electron-atom wavefunction, Ψ, in which the wavefunctions for the scattered electron, F_n, are found as coefficients:

$$\Psi = A \sum_{n=0}^{p} \Phi_n(\underline{x}_1,\underline{x}_2,\dots,\underline{x}_N)\ F_n(\underline{x}_{N+1}) \ +$$

$$A \sum_{n=p+1}^{p+q} \bar{\Phi}_n(\underline{x}_1,\underline{x}_2,\dots,\underline{x}_N)\ F_n(\underline{x}_{N+1}) \ +$$

$$\sum_{n=1}^{r} a_n \chi_n(\underline{x}_1,\dots,\underline{x}_{N+1}) \tag{4.1}$$

The first term in (4.1) is a sum over p+1 atomic eigenstates, Φ_n, the second over q so-called pseudostates, $\bar{\Phi}_n$, and the third over r short range (N+1)-electron correlation functions, χ_n. The combined space and spin coordinates of the i^{th} electron are labelled $\underline{x}_i$ and A is the antisymmetrization operator, which cares for exchange effects. It is assumed that the eigen-pseudostates are orthogonal to one another and to the states and that the L^2 (i.e. square integrable) functions χ_n are already antisymmetrized. Inserting (4.1) into the Schrödinger equation

$$H\Psi = E\Psi \ , \qquad \text{with} \tag{4.2a}$$

$$H = \sum_{i=1}^{N+1} \left[\left(-\nabla_i^2 - 2\frac{Z}{r_i}\right) + \sum_{j>i}^{N+1} \frac{2}{r_{ij}} \right]$$

$$= H_T - \nabla_{N+1}^2 - 2\frac{Z}{r_{N+1}} + \sum_{j=1}^{N} \frac{2}{r_{N+1,j}} \ , \tag{4.2b}$$

H_T being the target Hamiltonian, and requiring that the projection of $(H-E)\Psi$ onto the Φ_n, $\bar{\Phi}_n$ and χ_n vanishes, leads to a set of integro-differential equations for the functions F_n. When dropping the correlation functions χ_n, the coupled equations are of the form:

$$\left(\nabla^2 + k_n^2 - 2\frac{Z}{r_{N+1}}\right) F_n(\underline{x}_{N+1}) =$$

$$\sum_m^{p+q} V_{nm}(r_{N+1})\ F_m(\underline{x}_{N+1}) + \sum_m^{p+q} \int W_{nm}(r_{N+1},r_N)\ F_m(\underline{x}_N)\,d\underline{x}_N. \tag{4.3}$$

The right-hand side contains both direct potential terms V_{nm}:

$$V_{nm}(r_{N+1}) = \int \phi_n^*(\underline{x}_1,\ldots,\underline{x}_N) \left(\sum_{j=1}^{N} \frac{2}{r_{N+1,j}}\right) \phi_m(\underline{x}_1,\ldots,\underline{x}_N)\ d\underline{x}_1..d\underline{x}_N \tag{4.4a}$$

and exchange potential terms W_{nm}:

$$\int W_{nm}(r_{N+1},r_N)\ F_m(\underline{x}_N)\ d\underline{x}_N = -N \int \phi_n^*(\underline{x}_1,\ldots\underline{x}_N)\ [H-E]\ \phi_m(\underline{x}_1,\ldots,\underline{x}_{N-1},\underline{x}_{N+1})\ F_m(\underline{x}_N)\ d\underline{x}_1\ldots d\underline{x}_N\ . \tag{4.4b}$$

The W_{nm} are non-local† operators; they appear as a result of the antisymmetrization operator A in eq. (4.1). No attempt is made to reduce the latter equation furthermore. However, since coordinate N+1 refers to an occupied state in the right-hand function Φ_m, it is evident that exchange contributes exponentially decreasing terms to the integro-differential equations when r_{N+1} is large. With other words, exchange potentials will be of short range. Inclusion of correlation functions χ_n leads to extra terms in eq. (4.3) and to a second set of coupled equations; for more details, see e.g. Callaway [4].

For open (energetically accessible) channels not involving ionization, the boundary condition satisfied by the scatter functions F_n is

---

† A local potential is an operator, which is diagonal in its coordinate representation: $\langle \underline{r}|V|\underline{r}'\rangle = V(\underline{r})\ \delta(\underline{r}-\underline{r}')$.

$$F_n(\underline{r}) \underset{r\to\infty}{\sim} \exp(i\underline{k}_n\cdot\underline{r})\ \delta_{ni} + f_{ni}(\theta,\phi)\ \underline{r}^{-1}\ \exp(ik_n r) \qquad (4.5)$$

where the index i labels the incident channel and k_n the electron wave vector in the final channel n. In the closed channels, $F_n(r)$ vanishes asymptotically faster than $(1/r)$. In the case of elastic scattering, only the single channel equations resulting from the projection onto the ground state Φ_o have to be considered.

The differential cross section for elastic scattering, or for discrete excitation to a final level j is then

$$\left(\frac{d\sigma}{d\Omega}\right)_{ji} = \frac{k_j}{k_i}\ |f_{ji}(\theta,\phi)|^2 \qquad (4.6)$$

Several mathematical techniques have been developed for solving the coupled equations. We mention the linear algebraic method, first proposed by Eissner and Seaton [5], the R-matrix method of Burke et al. [6], the variational method as used by Nesbet [7] and the non-iterative integral equation method (NIEM) developed by Smith and Henry [8]. All these techniques have in common that their accuracy is limited by the available computer power. It is hard to say which yields overall the best results, since the methods have different efficiencies under differing circumstances. For example, the variational method has considerable advantages if one wishes to include a large number of closed channels, as in elastic scattering below the first inelastic threshold, or to study closely spaced energies below a threshold as in the investigation of resonances. However, it may be slow and not particularly accurate when there are many open channels.

Let us consider the three terms in (4.1) more closely. The first sum contains those eigenstates whose exact inclusion is thought to be essential for a correct description of the scattering process. For practical reasons only a few eigenstates can be retained in this sum; if eq. (4.1) is broken off after this term, (4.1) is called a (p+1)-state pure close-coupling approximation. Clearly, this form will be inappropriate at the intermediate energy range. Therefore, the second and third sum in (4.1) are inserted to take into account the eigenstates omitted from the first sum in some average way. The pseudostates and correlation terms embody as such the essence of the fundamental problem of intermediate energies, i.e. the need to include couplings to very many states.

The use of two types of terms to represent the omitted eigenstates can be derived from different physical points of view. The inclusion of short range correlation terms χ_n is motivated by a desire to describe accurately the correlated motion of the (N+1) electrons when they are close together. Pseudostates, $\bar{\Phi}_n$, are a natural way of building very important long range interactions such as polarization into (4.1). Alternatively, pseudostates may be primarily designed to allow for loss of flux from the eigenstate channels in the first sum, since at intermediate energies flux loss to other open channels is a very important physical effect.

We now come to the shortcomings in the above expansion formalism. The first is that one may ask whether the included pseudostates and correlation terms give a sufficiently complete representation of the omitted eigenstates. This is a fundamental problem, which is hard to assess at the intermediate energies. In the case of atomic hydrogen Walters [30] gives an example of one criterion for testing the 'effective completeness', where in a partial wave analysis he shows that the $2\bar{p}$-pseudostate calculation of Fon et al. [9] fails, very severely, to represent the short range interactions. This $2\bar{p}$-pseudostate however, does correctly describe the phase-shifts in the higher angular momenta, thus the long range part of the potential.

A second problem is that pseudostates behave as if they were real atomic eigenstates. This means that corresponding to each pseudostate is an excitation threshold with its associated resonances. Since these are unphysical and merely artifacts of the approximation (4.1), calculations in their vicinities will be unreliable. However, this difficulty may be overcome by using different sets of pseudostates, since there is no reason why the same set should be used at all impact energies.

There are unphysical pseudo-resonances also associated with the short range correlation terms, which can lead to catastrophic effects in the calculated cross section. Burke et al. [10] have proposed a technique of energy averaging over the resonant cross section. However, this process is not uniquely defined and further study is required.

Concluding this subsection, as the impact energy is increased and the higher intermediate energies are approached, the close coupling methods, in principle being valid, become unnecessarily complicated. Then a different attitude to the collision problem proves beneficial, which will be considered in section 2.2.

2.1.2. *The polarized orbital method*

An alternative approach to the elastic scattering of slow electrons from atoms is based on the polarized orbital approximation, first proposed by Temkin [11]. This method assumes that the velocity of the incident electron is substantially less than that of the atomic electrons, so that the electronic configuration of the atom can readjust itself instantaneously to the position of the projectile electron. Basically, this method consists of adding a term Φ^1 to the unperturbed atomic wavefunction Φ^0, where Φ^1 is a superposition of polarized orbitals, representing the perturbation of the atomic wavefunctions in the field of the incident electron. This interaction is treated in a Hartree-Fock scheme to first order, and mostly with the external electron considered as stationary, the so-called adiabatic approximation. The total wavefunction $\tilde{\Psi}$ for the system of an atom plus an electron is then written as

$$\tilde{\Psi} = A\ \Psi(\underline{r},\underline{x})\ F(\underline{x}) \ , \qquad (4.7)$$

where A is again the anti-symmetrization operator, Ψ is given by $\Psi = \phi^0 + \phi^1$, and F represents the scattering wave function; $\underline{r}$ is the ensemble of space and spin coordinates of the atomic electrons and $\underline{x}$ are those of the incident electron. In order to determine F, one projects the full Schrödinger equation onto the ground state of the atom:

$$<\Phi^{o}\ |H-E|\ A\Phi^{o}F> + <\Phi^{o}|H-E|\ A\Phi^{1}F> = 0 \qquad (4.8)$$

Most authors apply the adiabatic exchange approximation, i.e. the polarization-exchange terms are neglected, whence the second term in eq. (4.8) is replaced by $<\Phi^{o}|H-E|\Phi^{1}F>$ and one obtains

$$<\Phi^{o}|H-E|A\Phi^{o}F> + <\Phi^{o}|H-E|\Phi^{1}F> = 0 \qquad (4.9)$$

Assuming $<\Phi^{o}|H_o - E_o|\Phi^{1}> = 0$, where H_o is the atomic Hamiltonian, one can reduce eq. (4.9) to:

$$(\nabla_x^2 - 2V_s - 2V_p + k^2)\ F(\underline{x}) = 2K_{ex} \qquad (4.10)$$

Here V_s and V_p are the static and polarization potentials, respectively. Explicitly:

$$V_s(x) \equiv -\frac{Z}{x} + \sum_{i=1}^{N} <\phi_i^o\ |\frac{1}{|\underline{r}_i - \underline{x}|}|\ \phi_i^o> \qquad (4.11a)$$

$$V_p(x) \equiv \sum_{i=1}^{N} <\phi_i^o\ |\frac{1}{|\underline{r}_i - \underline{x}|}|\ \phi_i^1> = \sum_{v=0}^{\infty} V_p^v(x)\ , \qquad (4.11b)$$

where in (4.11b) V_p has been written as a multipole expansion; however, most calculations have been performed in the dipole approximation. The summation runs over N unperturbed and perturbed atomic orbitals, $|\phi_i^o>$ and $|\phi_i^1>$ respectively. K_{ex} is the static exchange kernel, a non-local potential expression.

The main difficulties with this method are caused by the non-local character of the exchange expression K_{ex}. One way to handle this is to approximate K_{ex} by an equivalent <u>local</u> exchange potential $V_{ex}(x)$, whence (4.10) reduces to a simple potential scattering equation to be solved with partial waves:

$$\left(\frac{d^2}{dx^2} - \frac{\ell(\ell+1)}{x^2} - 2[V_s(x) + V_p(x) + V_{ex}(x)] + k^2\right)f_\ell(x) = 0. \qquad (4.12)$$

A large number of local exchange potentials have been proposed in the literature; the most successful ones include the semi-classical exchange (SCE) approximation of Furness and McCarthy [12] and the free electron gas exchange (FEGE) model of Hara [13]. The accuracy of these approximations varies with the energy of the incident electron and, to a lesser extent, the structure of the atom. For example, the SCE is first valid at $k \gtrsim 1.5$, whereas the FEGE model - as it originates from the Fermi statistics of a free electron gas - is expected to work best for systems with many electrons.

Recently, McEachran and Stauffer [14] succeeded in calculating the exchange kernel exactly, i.e. retaining its non-local character. Besides, they made an extensive study on the influence of the higher multipoles in the expansion (4.11b). The results of their calculations will be discussed along with our experimental data in section 4.

Apart from its adiabatic construction, there is yet another important factor, which restricts the applicability of the polarized orbital method to the lower impact energies: it is essentially a one-channel approximation in which loss of flux to the inelastic channels is not accounted for and, as we have seen, this is a serious effect at the intermediate energies.

2.2. The high-energy approach

We now turn to the various models, which have been developed for the high impact energies. There the projectile electron has to penetrate deeply into the atom in order to get scattered over appreciable angles, whence the interaction with the static field of the atom plays the dominant role. Polarization and absorption contributions are mainly concentrated in the small angle deflections, whereas the exchange effects are relatively small. These ideas find expressions in the theoretical approaches for the high energy regime, in that usually perturbation methods are carried out for the direct part of the scattering amplitude to which afterwards exchange approximations are added.

Before actually discussing some of the models, we switch over from the notation, presented in the previous section, to the more formal concepts, as these have become common practice in scattering theory. In the following, we shall mainly work in momentum space representation.

The Hamiltonian of eq. (4.2b) is now written as

$$H = H_o + V \ , \tag{4.13}$$

where H_o is the sum of the kinetic energy operator of the projectile plus target Hamiltonian and V the full interaction potential between target and projectile. Scattering theory learns that the scattering amplitude for the <u>elastic</u> transition from the 'asymptotic free' state $|k_o,\Phi_o\rangle$ to the free state $|k_f,\Phi_o\rangle$ - which are eigenstates of H_o such that the target is left in its (normalized) ground state $|\Phi_o\rangle$ - can be written as

$$f(\underline{k}_f,\underline{k}_o) = -\frac{1}{2\pi}\langle \underline{k}_f,\Phi_o|V|\tilde{\Psi}^+\rangle \ , \tag{4.14}$$

where the 'stationary scattering state' $|\tilde{\Psi}^+\rangle$ is given by the Lippmann-Schwinger equation

$$|\tilde{\Psi}^+\rangle = |\underline{k}_o,\Phi_o\rangle + G_o^+V|\tilde{\Psi}^+\rangle \ . \tag{4.15}$$

G_o^+, the 'free' Green's operator, plays a central role in scattering theory and is given by

$$G_o^{\pm} = (E - H_o \pm i\eta)^{-1}, \quad \eta\to 0^+ \ . \tag{4.16a}$$

$$E = \tfrac{1}{2}\, k_o^2 + \varepsilon_o \ , \tag{4.16b}$$

ε_o being the ground state energy.

We shall discuss now the principles on which the most widely used models are based. Direct scattering will be considered first; incorporation of exchange contributions will be dealt with separately in subsection 2.2.3.

2.2.1. *The Born series*

The Lippmann-Schwinger equation is in fact an iterative equation; by assigning a suitable start function to $|\tilde{\Psi}^+>$ in the right-hand side of eq. (4.15), one can construct a series expansion by iteration as a solution for $|\tilde{\Psi}^+>$. The Born series is then generated starting from the free incoming wave $|\underline{k}_o,\Phi_o>$:

$$|\tilde{\Psi}^+> = |\underline{k}_o,\Phi_o> + G_o^+V|\underline{k}_o,\Phi_o> + G_o^+VG_o^+V|\underline{k}_o,\Phi_o> + \dots \qquad (4.17)$$

By substitution of eq. (4.17) into eq. (4.14) we obtain the Born series for the scattering amplitude,

$$f = \sum_{n=1}^{\infty} \bar{f}_{Bn} , \qquad (4.18)$$

where

$$\bar{f}_{Bn} = -\frac{1}{2\pi} <\underline{k}_f,\Phi_o|VG_o^+V \dots G_o^+V|\underline{k}_o,\Phi_o> . \qquad (4.19)$$

In this last expression the interaction V between the projectile and the target appears n times and the Green's operator G_o^+ (n-1) times. The Born series converges only rapidly for high impact energies and weak interactions; however, beyond the second order term calculations become very complicated and so modifications to the expansion (4.17) have been proposed.

2.2.2. *The eikonal Born series (EBS)*

Just as the exact Born series expansion, eq. (4.19), this method is a totally perturbative approach, the aim of which is to calculate the scattering amplitude correct up to order k_o^{-2}. It combines the properties of the usual Born series with those of the so-called Glauber [15] series, the last one obtained within a semi-classical approach, where the projectile electron is assumed to follow a well-defined trajectory. This approach is valid only if

$$k_o a >> 1 , \qquad (4.20)$$

where a is the 'size' of the atom. The terms f_{Gn} in the Glauber series are alternatively purely real and purely imaginary. For the elastic scattering of electrons (exchange excluded) the required amplitude, i.e. correct to order k_o^{-2}, is

$$\bar{f}_{B1} + \bar{f}_{B2} + \mathrm{Re}\ \bar{f}_{B3}\ , \tag{4.21}$$

where $\bar{f}_{B1,2,3}$ are given by (4.19). The amplitude $\bar{f}_{B3}$ would be very difficult to calculate exactly. Byron and Joachain [16] showed, that the third order Glauber amplitude $\bar{f}_{G3}$ gives a good representation of Re $\bar{f}_{B3}$; it can readily be calculated, so that replacement of Re $\bar{f}_{B3}$ by $\bar{f}_{G3}$ in (4.21) leads to a computationally tractable formula. The result is the EBS approximation, i.e.

$$f = \bar{f}_{B1} + \bar{f}_{B2} + \bar{f}_{G3}\ . \tag{4.22}$$

The method works very well for helium above ≈100 eV, but gives poor results for the heavier noble gases. The reason for this is that (4.22) treats <u>all</u> couplings up to third order in perturbation theory; as shown by Walters [17] the strong static fields of neon and argon require higher order perturbation terms, and for that purpose the next methods are more appropriate.

2.2.3. *Distorted wave and optical potential methods*

It has been recognized, that expanding the scattering amplitude in powers of the full electron-atom interaction V – as in the Born and EBS series – results in a slow convergence. The primary cause lies in the static potential of the ground state $\langle\Phi_o|V|\Phi_o\rangle$, because of the singular nature of the electron-nucleus interaction $-Z/r_o$ [18]. The static potentials of the other atomic eigenstates, $\langle\Phi_n|V|\Phi_n\rangle$ $n \neq 0$, will also converge slowly, but faster as compared to $\langle\Phi_o|V|\Phi_o\rangle$; the inelastic couplings, $\langle\Phi_m|V|\Phi_n\rangle$ $m \neq n$, are weak and well behaving functions of the scattered electron coordinate r_o. So one is led to the conclusion that inelastic couplings may be amenable to a perturbative treatment; scattering by static potentials, at least $\langle\Phi_o|V|\Phi_o\rangle$, should always be handled exactly.

The above considerations have been applied in the distorted-wave second Born approximation (DWSBA) [18,19] and in second order optical potential models [20]. The basic idea is simple: the full interaction V is splitted into two parts

$$V = V_1 + V_2 \tag{4.23}$$

and using the two-potential formula given by Goldberger and Watson [21], eq. (4.14) may be written

$$f(\underline{k}_f,\underline{k}_o) = -\frac{1}{2\pi}\langle \underline{k}_f,\Phi_o|V_1|\Phi^+(\underline{k}_o)\rangle - \frac{1}{2\pi}\langle\Phi^-(\underline{k}_f)|V_2|\tilde{\Psi}^+\rangle \ , \tag{4.24}$$

where

$$\Phi^\pm(\underline{k}) = e^{i\underline{k}\cdot\underline{r}_o}\,\Phi_o + G_o^\pm V_1\,\Phi^\pm(\underline{k}) \ . \tag{4.25}$$

If the Lippmann-Schwinger equation for $\tilde{\Psi}^+$ is now written in the form

$$\tilde{\Psi}^+ = \Phi^+(\underline{k}_o) + G_1^+ V_2 \tilde{\Psi}^+ \ , \quad \text{with} \tag{4.26}$$

$$G_1^+ = \lim_{\eta\to 0}\,(E - H_o - V_1 + i\eta)^{-1} \tag{4.27}$$

and a Born expansion of (4.26) is made, one finally obtains the distorted-wave Born series

$$f(\underline{k}_f,\underline{k}_o) = -\frac{1}{2\pi}\langle\underline{k}_f,\Phi_o|V_1|\Phi^+(\underline{k}_o)\rangle$$

$$-\frac{1}{2\pi}\langle\Phi^-(\underline{k}_f)|(V_2 + V_2G_1^+V_2 + \ldots)|\Phi^+(\underline{k}_o)\rangle . \tag{4.28}$$

The series in (4.28) is a perturbation expansion in terms of V_2 which, correct to any order in V_2, contains the effect of V_1 to all orders. The model derives its name from the fact, that the functions Φ^+ are the distorted waves in the static field V_1:

$$V_1 = PVP , \quad \text{with } P = |\Phi_o\rangle\langle\Phi_o| . \qquad (4.29a)$$

V_2 is given by:

$$V_2 = QVQ , \quad \text{with } Q \equiv 1 - P = \sum_n |\Phi_n\rangle\langle\Phi_n| \quad n \neq 0 , \qquad (4.29b)$$

where $\sum_n$ includes the continuum states. Substitution of eq. (4.29) into (4.28) leads to the distorted-wave second Born approximation:

$$f(\underline{k}_f,\underline{k}_o) = f_{st}(\underline{k}_f,\underline{k}_o) - \frac{1}{2\pi} \langle \Phi^-(\underline{k}_f)|V_{oo}|\Phi^+(\underline{k}_o)\rangle \qquad (4.30a)$$

with

$$V_{oo} = \frac{1}{4\pi^3} \sum_{n\neq 0} \lim_{\eta\to 0} \int d\underline{k} \, \exp^{i\underline{k}.(\underline{r}_o - \underline{r}_o')} \langle\Phi_o(\underline{x})|V(\underline{r}_o,\underline{x})|\Phi_n(\underline{x})\rangle$$

$$\cdot \frac{\langle\Phi_n(\underline{x})|V(\underline{r}_o',\underline{x})|\Phi_o(\underline{x})\rangle}{k_n^2 - k^2 + i\eta} , \quad k_n^2 = k_o^2 + 2(\varepsilon_o - \varepsilon_n) . \qquad (4.30b)$$

Here V_{oo} is explicitly written as a second order potential; it contains long range interactions and flux loss effects, the importance of which at intermediate energies was previously stressed.

The use of projection operators on the full interaction potential as in eq. (4.29) is a typical characteristic of so-called optical potentials, as it was initiated by Feshbach [22]. The basic philosophy behind the optical potential method is to include all channels in an approximate way in one or some higher order equivalent potentials; this in contrast to close coupling, where generally only a small number of states are explicitly taken along. On the other hand, a major difficulty associated with second order potentials is how to evaluate the infinite sum over intermediate atomic eigenstates $|\Phi_n\rangle$, actually the same problem as with the close coupling method. The most popular way of overcoming this difficulty has been to use the closure approximation [23]†. In this approach the contributions of a small number of 'important'

---

†The reader should recall that closure implies, for a complete set $|\phi_n\rangle$: $\sum_{\text{all } n} |\phi_n\rangle\langle\phi_n| = 1$.

states are calculated exactly while those of the remaining states are approximated by setting an average value $\bar{\varepsilon}$ for ε_n in (4.30b); the completeness of the atomic set $|\Phi_n\rangle$ is then invoked to reduce the sum to a tractable form. The average energy, $\bar{\varepsilon}$, is chosen in some physically meaningful way [19]; for example by demanding that the exact dipole polarizability of the atom is built into V_{oo}. It is important to note that in this way the completeness of the set $|\Phi_n\rangle$ is retained; this is to be contrasted with the use of finite, and therefore incomplete, sets of pseudostates and correlation terms. The price paid for it however, is the sacrifice of energy differences. The recent exact calculations of Ermolaev and Walters [24], i.e. sum over intermediate states carried out exactly, have shown that the closure approximation can work quite well, provided one stays well above the vicinity of the inelastic thresholds.

Another technique for approximation the sum in eq. (4.30b) is that used at lower energies, i.e. again with pseudostates [25]. Here the infinite sum over $|\Phi_n\rangle$ is replaced by a sum over suitably chosen pseudostates. As mentioned earlier, the difficulty with pseudostates is to know whether the finite set is 'effectively complete' for the problem in hand.

Another major technical problem in handling second order potentials is their non-local character. This difficulty has led to the study of local (energy dependent) approximations. For example, in the second order optical potential method one solves the wave equation (excluding exchange)

$$(H_o + V_1 + PV_2G_o^+V_2P - E)\tilde{\Psi} = 0 \quad , \tag{4.31}$$

where V_1 and V_2 are defined as in (4.29). In their ab initio optical model, Byron and Joachain [26] reduced the non-local operator $PV_2G_o^+V_2P$ to a complex *local potential* $V_{pol} + iV_{abs}$, with V_{pol} and V_{abs} both real. The long range term V_{pol} accounts for the polarization of the target; it is derived from first principles and contains both the dipole polarizability of the atom and the average excitation energy (from closure!) as parameters. V_{abs} arises from the absorption of flux from the elastic to open inelastic channels; it can be obtained using the properties of the Born and Glauber series. Constructed in this way, both V_{pol} and V_{abs} are impact energy dependent. The direct elastic scattering amplitude is then calculated by solving the one-channel Schrödinger equation:

$$(H_o + V_1 + V_{pol} + iV_{abs} - E)\tilde{\Psi} = 0 \ . \qquad (4.32)$$

McCarthy et al. [27] have used a local approximation for the entire optical potential to calculate elastic scattering from all the noble gases at energies from 100 - 3000 eV. Their potential is constructed in a rather ad-hoc way: the real part includes the ordinary static potential, plus an energy independent adiabatic polarization potential. An imaginary part is also introduced following a localization procedure of Furness and McCarthy [12] and is of the form

$$\text{Imaginary part} \sim i \ \frac{W(E)}{|E - V(r)|^2} \qquad (4.33)$$

in which $V(r)$ is the real part of the potential and $W(E)$ an adjustable parameter, which is fitted to the experimental total inelastic cross section. Current research of this group is to improve on $V(r)$, in particular the polarization part of it.

So far we have only discussed direct scattering. For electron scattering, also exchange contributions have to be incorporated. Usually this is done by adding an extra term to (4.22), (4.32) and (4.30a), obtained after localization the exchange part of the potential kernel W_{nm} (cf. eq. (4.3)). Several procedures have been developed for elastic scattering; we give one example here, the static exchange approximation.

It is supposed there, that the scattering function $F(\underline{r})$ of eq. (4.3) is given as the solution of an effective Schrödinger equation with the ordinary static potential of the atom, $V_o(r)$, and including a local static exchange potential $V_{se}(R)$, but ignoring coupling to other channels:

$$[\nabla^2 + k_o^2 - V_o(r)]\ F(\underline{r}) = V_{se}(r)\ F(\underline{r})\ . \tag{4.34}$$

The non-local exchange operator has the general structure of the left-hand side of eq. (4.35) as given below

$$\int \Phi_i^*(\underline{r}')\ \frac{e^2}{|\underline{r}-\underline{r}'|}\ F(\underline{r}')\ d^3r'\ \Phi_m(\underline{r}) \approx W_{im}(\underline{r})\ F(\underline{r})\ . \tag{4.35}$$

Rewriting this integral according to Riley and Truhlar [28] and inserting it in eq. (4.34) leads to a quadratic expression for V_{se}, which physical solution is

$$V_{se}(r) = \tfrac{1}{2}\ |k_o^2 - V_o(r)| - \tfrac{1}{2}[\,|k_o^2 - V_o(r)|^2 + \\ + 16\,\pi\, e^2 \sum_i \beta_i |\Phi_i(r)|^2]^{\frac{1}{2}} \tag{4.36}$$

The sum runs over all the occupied atomic orbitals $|\Phi_i\rangle$ used in constructing a Hartree-Fock wave function, and the β_i are numerical constants, positive or negative, depending on the spin arrangement considered. This potential, first proposed by Furness and McCarthy [12], describes the exchange process quite well at high energies down to about $k^2 = 4$. In the limit of large k it reduces to the familiar Ochkur [29] expression, which is used in the EBS calculations:

$$V_{Och}(r) = -\frac{8\,\pi\, e^2}{k^2} \sum_i \beta_i\ |\Phi_i(r)|^2 \tag{4.37}$$

It should be realized that the exchange amplitudes decrease faster with energy than the direct ones. The high energy behaviour of the former is given in the first Born approximation by the general Ochkur-Bonham formula. Second Born exchange amplitudes have been calculated only for electron-hydrogen scattering (both elastic and inelastic) by Gavrila and Mandal [31]. They showed that this term vanishes only slightly faster than the first order one at large k, which indicates a slow convergence rate for the Born exchange expansion.

For the present research we are more interested in handling exchange at smaller k; this should be done with care, as the following example demonstrates.

Although no calculations have been performed so far within the DWSBA formalism for the noble gases below 100 eV, extensive research by Walters [30] on atomic hydrogen at 30 and 50 eV has revealed some interesting aspects when pushing the DWSBA downwards into the intermediate energy regime. It appeared that not the closure approximation is responsible for a breakdown, but instead an inadequate treatment of exchange. Besides treating exchange as a static phenomenon only, as with potentials of the form of eq. (4.36), it is essential to incorporate exchange couplings to excited states too, just as done for the direct couplings, eq. (4.30b). We shall come back to this point in the discussion of the experimental results in section 4. We conclude this review with an alternative method for approximating the equivalent optical potential, i.e. developed within the many-body formalism.

2.2.4. Many-body theory

First applied successfully in nuclear physics, this theory lends itself equally well for the description of electron-atom interactions, which are of Coulombic character. For a reader, who is unexperienced in this field it is hard to make himself familiar with the basic formalism; even a brief outline would require to explain a lot of notational concepts. Therefore we confine ourselves to shortly indicating the essential steps, which Scott and Taylor [32] devised in order to construct a computational scheme for the elastic scattering of electrons on helium from 30 to 200 eV. Further details of the general theory may be obtained from Schneider et al. [33].

Recalling, for elastic scattering by the target ground state (the entrance channel is denoted by $n = 0$), eq. (4.3) becomes

$$(\nabla^2 + k_o^2 - 2\,\frac{Z}{r})\; F_o(\underline{r}) = \sum_m V_{om}(r)\; F_m(\underline{r}) + \sum_m \int W_{om}(r,r')\; F_m(r')dr'. \tag{4.38}$$

This equation is reduced to a one-channel problem of the form

$$(\nabla^2 + k_o^2)\; F(\underline{r}) = \int \Sigma(\underline{r},\underline{r}';\, k_o^2)\; F(\underline{r}')d\underline{r}' \;. \tag{4.39}$$

Here the optical potential $\Sigma(\underline{r},\underline{r}';\, k_o^2)$ replaces the many-channel problem of eq. (4.38). Physically, it is the effective potential experienced by the incoming electron as it approaches the target atom in the (incident) elastic channel. Again, Σ is a non-local and complex operator, the imaginary component accounting for absorption by the inelastic channels; it is extremely complicated, so for actual computations a number of approximations have been developed. Here many-body theory is called for, in which single and two-particle Green's functions play an important role. Within this framework, Scott and Taylor use the 'random phase approximation' and finally arrive at the following expression, correct up to second order in the Coulomb interaction:

$$\Sigma(\underline{r},\underline{r}';\, k_o^2) = \Sigma^{HF}(\underline{r},\underline{r}') + \Sigma^{P}(\underline{r},\underline{r}';\, k_o^2) - \Sigma^{EP}(\underline{r},\underline{r}';\, k_o^2) \tag{4.40}$$

The first term on the right-hand side Σ^{HF} is the static interaction, where the superscript HF denotes that Hartree-Fock potentials have been used for the mutual interaction between the atomic electrons. To simplify the computation, the exchange part in Σ^{HF} was approximated with the equivalent local potential of Furness and McCarthy, eq. (4.36). The term Σ^{P} is essentially a polarization potential; it is a complex quantity and contains a summation over the bound states of the target (just as in eq. (4.30b)) and an integration over the continuum states. Scott and Taylor retained just one pseudostate in this summation; their particular choice for this state leads to only one parameter, which is adjusted such that Σ^{P} reproduces the correct long-range dipole behaviour of the polarization potential. The disadvantage of this procedure is that no freedom is left for adjusting the imaginary part of Σ^P, so the absorptive part of the potential may not be suitably described. In their actual calculations, the exchange polarization term Σ^{EP} was omitted, since at lower energies it caused their computer programs to break down, whereas at energies above ≈ 80 eV it induced a difference in the final results of only a few percent.

Finally, eq. (4.39) was decomposed in a partial wave series, from which the first L terms were calculated; for the remaining terms the Born phase-shifts (see eq. (1.9)) were taken (which are real, so ignore absorption).

Having discussed the present status of the art of the most widely used theoretical models, we can compare them now critically with out experimental data, as will be done in section 4.

3. Experimental procedure and error discussion

3.1. Experimental procedure

The differential cross section $\sigma(\theta)$ for elastic scattering is defined as:

$$I_s = I_o \, \sigma(\theta) \, (NL)_{eff} \, \Delta\Omega \tag{4.40}$$

where I_s is the flux of electrons elastically scattered over θ into the solid angle $\Delta\Omega$, I_o the primary beam current and $(NL)_{eff}$ the effective product of gas density and collision length L. Actually, eq. (4.40) is only valid for an infinitesimally narrow collision plane in which the gas is concentrated and the primary beam is thought to be constant. However, since we deal with a finite collision length, electrons are continually scattered out of the beam along the path because of both elastic and inelastic processes, as shown in figure 1 by the small arrow bunches.

The beam is thus attenuated and I_o has to be replaced by a local beam intensity $I(x)$, where x runs over the interaction length. $I(x)$ is simply given by the Lambert-Beer law (see eq. (2.1)):

$$I(x) = I_o\, e^{-Nx\sigma_{tot}} \quad . \tag{4.41}$$

The same happens with the scattered electron intensity I_s which is registered at the detector. For, the partial current $\Delta I_s(\theta)$ scattered from a slice Δx at position x (see figure 1) will undergo an absorption according to:

$$\Delta I_s(\theta) = I(x)\ \sigma(\theta)\ N\Delta\Omega(x)\ e^{-(L_{eff} - x)N\sigma_{tot}} \tag{4.42}$$

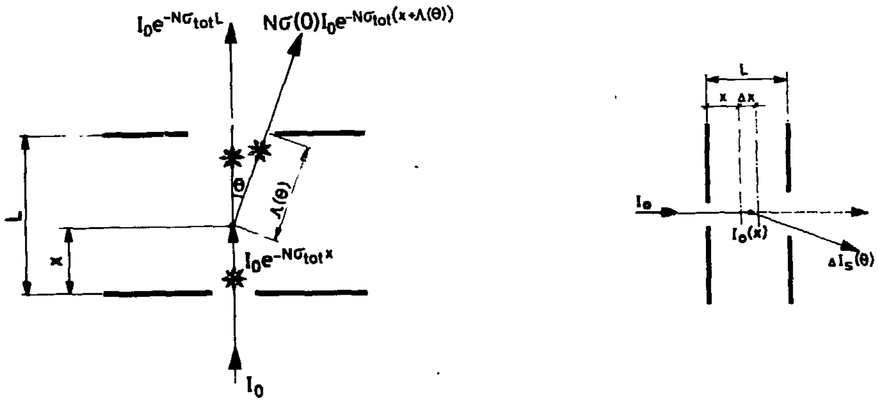

FIGURE 1

Scattering geometry in the collision chamber.

(a) Multiple collisions (indicated by arrow bunches) cause a further attenuation of the primary and scattered electron signal before leaving the collision cell. This extra absorption depends on the traversed path length; for small scattering angles θ, it is nearly independent of the collision event position x (i.e. $\Lambda(\theta) \approx \Lambda(0) = L - x$).

(b) Consequently, the detected signal $\Delta I_s(\theta)$ of electrons scattered from a slice of width Δx is approximately equal for all positions x in the cell.

In the last exponent no account has been given for the difference $\Lambda(\theta) - \Lambda(0)$ (see figure 1) in path length to the exit aperture of the collision cell between a scattered and beam electron, since this is negligible at the small scattering angles of interest to us.
Inserting eq. (4.41) into eq. (4.42) leads to:

$$\Delta I_s(\theta) = I_o \sigma(\theta)\ N\Delta\Omega(x)\ \Delta x\ e^{-(LN)_{eff}\ \sigma_{tot}} \quad . \qquad (4.43)$$

Integrating these contributions over the whole collision length L finally gives:

$$I_s(\theta) = I_o\ e^{-(LN)_{eff}\sigma_{tot}}\ \sigma(\theta)\ (NL)_{eff}\Delta\Omega \quad . \qquad (4.44)$$

where we have taken $\Delta\Omega(x)$ constant because L is small. Comparing eq. (4.44) with eq. (4.40) one sees that the influence of 'scattering out' is simply given by one exponential attenuation term.
Eq. (4.44) can be recasted into:

$$\sigma(\theta) = \frac{q\ S(\theta)}{\eta(NL)_{eff}\ \Delta\Omega I_o\ e^{-(NL)_{eff}\sigma_{tot}}} \qquad (4.45)$$

where $S(\theta)$ represents the number of pulses per second from the channelplates, η its quantum efficiency and q the electron charge. $\Delta\Omega$ is constant for all θ along the analyser entrance slit (see section 3.1 of the previous chapter) and easily calculated from the slit geometry. $(NL)_{eff}$ has been determined accurately by checking the linearity of the scattered signal as a function of the adjusted collision cell length (see section 3 of Chapter II), η is calibrated as described in section (5.3) of Ch. III. Finally, since we measure $I_o e^{-(NL)_{eff}\sigma_{tot}}$ directly with the Faraday cage (G in figure 6 of Ch. III) behind the cell, the requested differential cross section $\sigma(\theta)$ can be calculated.

It is worthwhile to note in view of eq. (4.45) that the calculation procedure for $\sigma(\theta)$ is facilitated considerably by measuring the attenuated beam intensity instead of the primary beam I_o. However, the approximation used in eq. (4.42) is only valid at small scattering angles; therefore, all other experimental groups concerned with absolute differential cross section measurements over a larger angular range, determined I_o. Consequently, they had to follow rather elaborate procedures in order to account for the 'attenuation' effect (see for example Jansen [34] and Bromberg [35]).

The primary beam intensity I_o we applied for the measurements lay in the 0.05 to 0.5 nA range, safely below its space charge limited value (typically 0.05 - 0.1 μA). The electron beam will not be defocused effectively by the field of the ions which are produced by ionizing collisions of the primary electrons with the target gas in the short collision cell. Indeed, the number of counts $S(\theta)$ appeared strictly proportional to the beam intensity I_o, when this was varied from 0.01 to 1 nA.

The gas density N was adjusted such that for each target gas species under study the final absorption of the primary beam did not exceed 10 - 15% of its incoming intensity I_o; in this way, contributions from multiple collisions back into the Faraday cup could be neglected. The pressures used varied from ≈ 0.5 Pa (4 mTorr) for the heavy noble gases to ≈ 4 Pa (30 mTorr) for helium.

The energy of the primary beam could be calibrated in two ways: (a) from the variation of the signal in the Faraday cup when the energy is scanned over the 19.3 eV resonance in helium (see Ch.II, sect.3), and (b) from the analyser voltage setting, needed for a full transmission from entrance to exit slit, as a function of the (low) beam energy. With narrow slits (entrance width 0.25 and exit width 0.75 mm) the latter method yields an accuracy of ≈ 0.3 eV for beam energies of ≈ 25 eV (see eq. (3.5) defining the energy resolution).

3.2. Error discussion

The derivation of the differential cross section is subject to more error sources in comparison with those involved in the total cross section measurements; this is mainly due to the channelplates and subsequent electronic data processing. We shall evaluate both the possible statistical and systematical errors step by step (for details of the apparatus and electronic equipment the reader is referred to Ch.III).

3.2.1. Statistical errors

(a) Statistics in the number of counts delivered by the channelplates. As in any other counting system, these are Poisson distributed and the statistical spread is thus approximately given by $\sqrt{N}$, where N represents the total number of counts in each channel. Since the measurements were stopped after an accumulation of at least 2000 counts per channel, this spread was $\lesssim 2.5\%$.

(b) Rounding-off errors due to digitizing in the ADC and division in the preprocessor. By using the dynamic amplifier before conversion in the ADC and by filling the remaining 2 - 5 bits in the processor with random numbers, an accuracy of 1 - 2% is achieved.

(c) Determination of the channelplate sensitivity η. Applying the calibration procedure, as described in section (5.3) of Ch.III, the resulting values for η at each impact energy fluctuated by no more than 3 - 5%.

(d) Amplifier noise. The Canberra preamplifiers generate only 1 fc equivalent noise, which is negligible with respect to the charge clouds of typically 1 pC as delivered by the channelplates.

(e) Reading errors of the baratron due to pressure fluctuations. To eliminate these, we developed an electronic (P(roportional), I(ntegrative), D(ifferentiating)) pressure controller and connected it in between the baratron read-out module and piezoelectric leak valve. The thus created feedback loop stabilized the pressure values we used within a few tenths of a percent.

3.2.2. *Systematical errors*

(a) Uncertainty in the effective product $(PL)_{eff}$. As described in Ch.II, sec.3, this product could be determined by carefully recording the scattering count rate as a function of the collision cell length. To the value for the short cell extracted from this procedure we assign an error of at most 2%.

(b) Uncertainty in the energy definition. From both calibration methods we estimated it at 0.3 eV; its influence on the accuracy depends again on the magnitude of the primary beam energy and on the target gas, but in no case exceeded 2%.

(c) Uncertainty in the solid angle $\Delta\Omega$. This is rather sensitive to the accuracy with which the distance collision centre-entrance slit is measured. The final error in $\Delta\Omega$ could be kept within 2%.

(d) Extra contributions to the scattering from (i) target gas outside the cell, (ii) impurities in the admitted gas, (iii) background particles, and (iv) electrons scattered off the cup edges and side-walls.

ad (i): From the conductivity of the entrance and exit apertures of the collision cell and the pumping speeds of the baffled oil diffusion pumps, it is a simple matter to calculate the contribution of scattering from target gas effusing through the apertures. With the short cell of 2 mm it enhances the scattering count rate with 2%. Recall that for the determination of $(PL)_{eff}$ we recorded the number of scattered particles as a function of the cell length; in that way, the extra scattering from the target gas outside the cell is automatically taken along in $(PL)_{eff}$.

ad (ii): This contribution could only be of importance for the light (helium and neon) gases. However, setting the analyser to the inelastic transitions of typical impurities like N_2 and O_2 showed that these contributions are negligible, after baking the gas inlet system and using the molecular sieve trap.

ad (iii): The background pressure was always kept as low as possible. Yet, in the case of helium and neon, we wanted to rule out any background contribution; this could be done by just subtracting it from the actual measurement, both recorded with the same amount of accumulated charge from the primary beam.

ad (iv): A fraction of the near forward scattered electrons will hit the cup edges and be further reflected. Consequently, some of them will enter the analyser, near equally distributed over the entrance slit. Bearing in mind that the cup knife edges are smaller than 0.1 mm, whereas the directly accepted scattering pattern extends already over 10 mm there, and that the entrance slit spans a solid angle of about $3 * 10^{-2}$ sr as seen from the cup, this contribution is negligible. More critical is the alignment of the cup; for, its rather long (14 mm) side walls will reflect the electrons directly into the analyser. However, such a perturbation would show up as an observable asymmetry between the left and right side in the final spectrum. With the primary beam well aligned in the centre of the cup, no such asymmetries did appear. Therefore, this error source could also be discarded.

TABLE I. Error estimations.

Statistical errors

error sources	estimated errors (%)	
(a) count-rate statistics	$\lesssim$ 2.5	
(b) digital rounding-off errors	$\lesssim$ 2.0	
(c) channelplate efficiency	$\lesssim$ 4.0	
mean sum error		$\lesssim$ 5

Systematical errors

error sources	estimated errors (%)	
(a) uncertainty in $(PL)_{eff}$	$\lesssim$ 2	
(b) uncertainty in energy calibration	$\lesssim$ 1-2	
(c) uncertainty in solid angle $\Delta\Omega$	$\lesssim$ 2	
total systematical error		$\lesssim$ 5-6
Total sum (systematical + statistical)		$\lesssim$ 7-8

Table I gives a summary of all relevant error sources; it must be emphasized that the displayed numbers are all taken as maximum bounds.

The total error is found by summing all the systematic errors, squaring this partial sum, adding it to the sum of the squares of the statistical errors and finally taking the square root of the final sum. From this a global error of 8% is derived.

As a final remark we mention that the least squares fits through the raw measurement spectrum indeed confirmed the estimated statistical error bound of 5%.

4. Results and discussion

In the following we shall restrict ourselves to presenting small angle elastic cross sections for impact energies between 17.5 and 100 eV. The lower limit was set by the primary beam performance: at still lower energies we were no longer able to keep the beam tail background below an acceptable level. At energies above 100 eV previous measurements by others already resulted in a consistent and accurate picture, experimentally as well as theoretically, as reviewed by Jansen et al. [34]. As such, nothing new could be added to their analysis. However, we did perform measurements there for calibrating and testing our equipment (see section 7 of Ch. III).

On the other hand, experimental data at angles smaller than 10° and below 100 eV were completely lacking. The only data we could compare with are those of Register et al. [36] for helium. However, these are extrapolated results from 10° down to 0° and therefore should be handled with care.

Since we are the first to open up this experimentally difficult region, a careful analysis and comparison with the various theories is possible now.

4.1. Helium

4.1.1. *Comparison with theory and other experiments*

The differential cross sections are summarized in table II; in figures 2(a), (b) and (c) three angles have been selected to compare with Register's extrapolated data and the existing theoretical calculations.

TABLE II. Differential (elastic) cross sections† of electron scattering on helium, in units of $a_o^2\ sr^{-1}$

θ(deg) \ E(eV)	18	20	22.5	25	27.5	30	35	40	50	60	70	80	90	100
0*	2.52	2.75	3.00	2.84	2.99	3.18	3.39	3.67	3.76	3.70	3.53	3.42	3.22	3.20
1	2.51	2.72	2.98	2.82	2.97	3.16	3.36	3.63	3.70	3.61	3.38	3.30	3.07	3.06
2	2.49	2.68	2.95	2.79	2.94	3.12	3.32	3.55	3.60	3.47	3.22	3.15	2.91	2.89
3	2.46	2.64	2.95	2.76	2.90	3.07	3.27	3.44	3.48	3.32	3.08	2.99	2.77	2.73
4	2.43	2.60	2.92	2.73	2.86	3.01	3.21	3.32	3.33	3.15	2.94	2.84	2.60	2.54
5	2.39	2.56	2.89	2.70	2.81	2.95	3.13	3.18	3.16	2.96	2.79	2.68	2.45	2.38
6	2.34	2.51	2.84	2.67	2.76	2.89	3.03	3.04	2.99	2.79	2.65	2.52	2.31	2.24
7	2.29	2.47	2.80	2.64	2.71	2.81	2.92	2.93	2.84	2.63	2.50	2.36	2.18	2.10
8	2.24	2.42	2.75	2.60	2.66	2.72	2.81	2.81	2.70	2.48	2.36	2.21	2.05	1.97
9	2.20	2.37	2.63	2.55	2.61	2.62	2.68	2.66	2.57	2.35	2.21	2.05	1.93	1.87
10*	2.16	2.33	2.56	2.50	2.56	2.52	2.55	2.52	2.45	2.23	2.05	1.92	1.83	1.76

* extrapolated values

† *total error* $\lesssim$ 7%

Before going over to a detailed discussion, a look at Register's method [36] of handling the data may help in understanding the picture. In order to put their data, obtained in a crossed-beam experiment, on an absolute scale, two procedures have been followed by them. For energies below the inelastic threshold, the measured angular distribution was χ-squared fitted with a partial wave formula, using three real phase shifts and one scaling parameter as minimalization parameters. This formula modifies the usual partial wave series in the sense that the non-varied higher phase shifts are approximated by the Born effective range expression (see eq. (1.9) of Ch.I). Since at these low energies the scattering process is largely dominated by a few partial waves only, the fitting will be highly reliable. On the other hand, above the inelastic threshold the phase shifts are no longer real quantities and as such the former procedure loses its validity. To fit complex phases means twice as much independent parameters and easily leads to ambiguities in the final results. An alternative approach was used: the same formula as before was fitted on the measurements, but now without the adjustable scaling factor. The fitting procedure is then in fact simply a reasonable parametrization of the relative cross section, whose magnitude is arbitrary. By extrapolation of the thus fitted curve to angles inaccessible to their equipment, total elastic cross section could be calculated and normalized on a semi-empirically derived value from the literature. Both procedures are claimed to yield an accuracy of 5 - 9%.

Figure 2(a) shows our results to agree well within the combined error bars with Register et al. at 10°, the smallest angle at which they could still measure above 40 eV. At 5°, figure 2(b), we found on the average 5% larger values between 30 and 60 eV, whereas at 0° both sets again confirm each other there. The actual small angle scattering thus possesses a more concave intensity distribution than the one obtained by extrapolation, although the difference is tiny.

Between 20 and 30 eV a step structure shows up from Register's extrapolations; however, one must be cautious in giving too much credit to these data, since their actual measurements had to stop at 15° in that regime. A careful scan in steps of 1 eV with our apparatus could give the answer about the existence of structure. Indeed, as shown in figure 3, a typical small angle phenomenon appears: the flux of elastically scattered electrons has a dip structure as a function of the impact energy, with its minimum located just in the vicinity of the single ionization threshold. Besides, the effect becomes stronger with decreasing angle, whereas it has nearly disappeared at angles > 10°. Sofar, this structure has not been predicted by any of the theoretical models, described in section 2. Since the effect is restricted to the region of

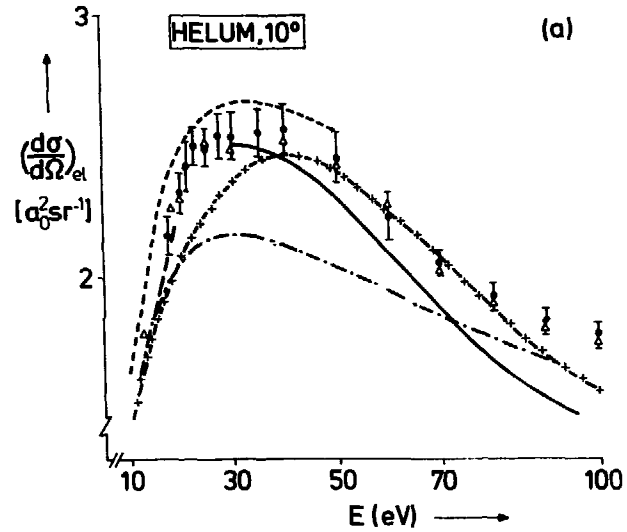
HELUM,10°
(a)
3
2
(dσ/dΩ)el
[a0²sr⁻¹]
10
30
50
70
100
E (eV)

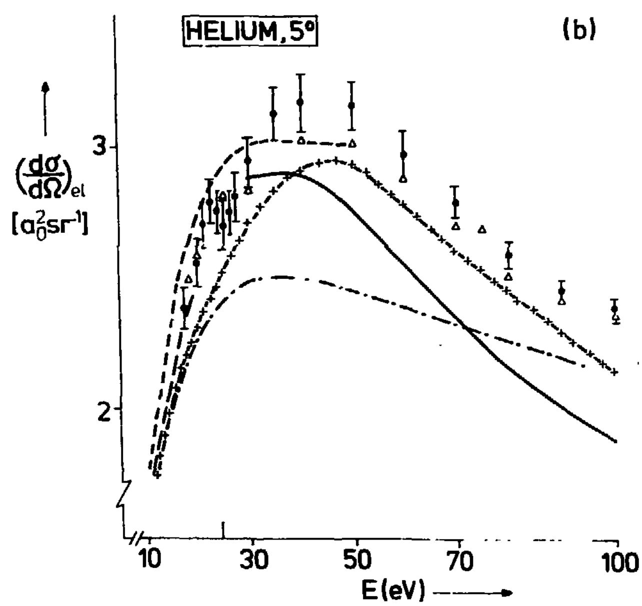
HELIUM,5°
(b)
3
2
(dσ/dΩ)el
[a0²sr⁻¹]
10
30
50
70
100
E(eV)

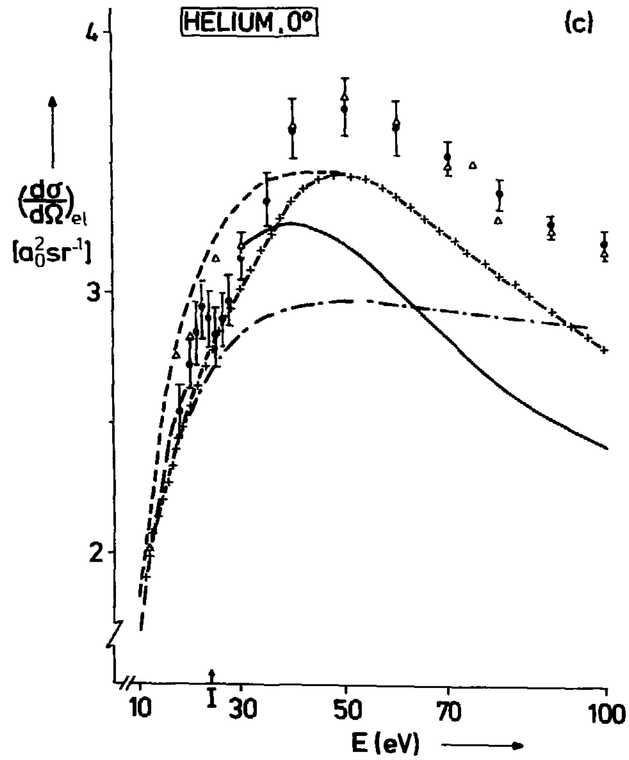

FIGURE 2

Differential cross sections for elastic electron-helium scattering as a function of the impact energy. Three scattering angles are displayed: (a) 10°, (b) 5° and (c) 0°. Legend: ⌶ , present results; Δ , Register et al.; - - - -, Nesbet; -.-.-.- Callaway; ———, Scott and Taylor; +-+-+-+, Fon et al.; ------, McEachran and Stauffer.

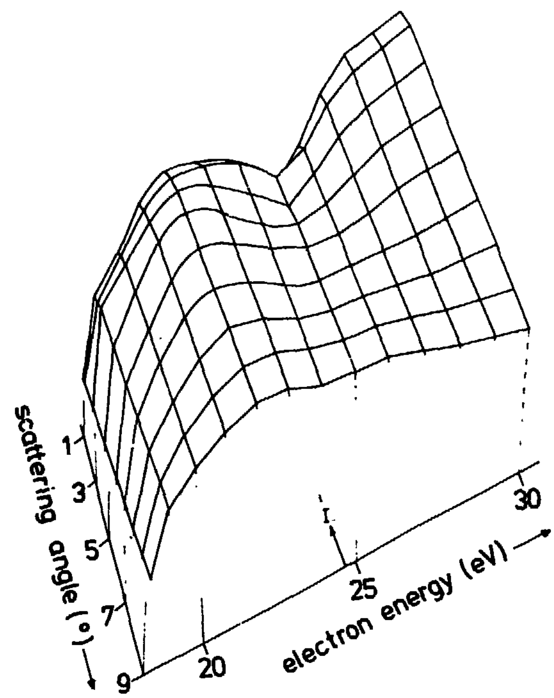

FIGURE 3

Three-dimensional representation of the dip structure at small scattering angles in the cross section when scanning the impact energy over the ionization threshold, I. The energy spread in the beam was 0.3 eV.

high Rydberg excitation and ionization, the explanation should be found in models explicitly developed for threshold phenomena. We shall defer a more thorough discussion to the next subsection; first we shall examine critically the performance of the existing theoretical models against our results.

The variational calculations of Nesbet [37], carried out up to the first inelastic threshold with a claimed accuracy of better than 2%, join perfectly well to our lowest energy (17.5 eV) data. Only the first three phase shifts were determined exactly; for the higher ones he took, following the suggestion of Andrick and Bitsch [38], the Born values. The agreement with the present results sustains this procedure.

Let us now look at calculations performed with the polarized orbital method. McEachran and Stauffer [14] used the adiabatic exchange approximation as in eq. (4.10), where they were able to determine the exchange kernel exactly. In their study they investigated the influence of the higher multipoles in the polarization potential, eq. (4.11b); at first sight the surprising result was that retaining only the dipole part yielded the best results. A critical examination of the perturbation expansion proved that the full adiabatic polarization potential will be too attractive in the case of electron scattering. Dropping the higher terms should compensate for this overattractiveness, although no guarantee can be given as to the right magnitude. Their best results lie systematically $\approx 7\%$ above ours at all angles, thus showing that even the dipole part alone still produces too large scattering.

Above 30 eV the adiabatic model is no longer valid; besides, inelastic effects become important there, which are not reflected in this model. As a result, McEachran's data level off and drop below the real cross section at the smallest angles. In order to extend the applicability of the polarized orbital method, Labahn and Callaway [39] did not project out the Schrödinger equation onto the target ground state $|\Phi_0\rangle$, but instead onto the disturbed wave function $|\Phi_0 + \Phi^1\rangle$. It leads to an extra dynamical potential term in eq. (4.10) by the action of the kinetic energy operator on this function; otherwise stated, the model accounts for non-adiabatic effects, when the incoming electron penetrates the atom. The repulsive character of this extra term weakens the adiabatic dipole polarization; the thus obtained values follow the experimental results much better below 25 eV. Unfortunately, their calculations do not allow for flux loss to inelastic channels. Figure 2 clearly demonstrates the large discrepancy to which this omission leads at forward angles; in particular it marks energies around 50 eV as the region of the most pronounced inelastic couplings.

In this context it is worthwhile to note that Onda and Truhlar [40] recently reactivated interest in the effective modelling of the polarization potential. They developed a new quantum-mechanical approach to the description of dynamic target charge polarization at intermediate energies. This resulted in a matrix effective potential, in which also flux loss is accounted for; it supersedes Labahn and Callaway's non-adiabatic distortion potential. However, their analysis contains some approximations, whose overall effect is hard to assess. The calculations they performed did not result in an improvement over Labahn and Callaway: on the contrary, their data deviate even more strongly at small angles from our results than those of these authors. One has to wait for future work for assessing if their model represents a progress in constructing effective potentials.

The two remaining theoretical curves in figure 2 are from models, explicitly developed for the intermediate energies: the close coupling calculations by Fon et al. [41] and the many-body calculations by Scott and Taylor [32]. For a good understanding of the following discussion, it is worthwhile to recall the basic feature common to these models. Both approximate the effective interaction potential with a static part, which dominates scattering over large angles, and a polarization part, which is leading at small momentum transfers. The static part is restricted to the atomic ground state wavefunction only, whereas the latter accounts for coupling with the higher intermediate states. For obtaining cross section values, a partial wave series starting with $\ell = 0$ has to be calculated for both the static and the polarization potential terms. We shall see below that just an incomplete treatment of the latter term causes deviations from our small angle data, whereas at large angles, mainly dominated by the static potential, Fon's calculations agree satisfactorily with Register's data [36] over a wide (5 - 200 eV) energy range.

Fon et al. [41] used a R-matrix method in which the target ground-state wavefunction is coupled with one pseudostate only, a $2\bar{p}$ state to allow for the full dipole polarizability (cf. section 2.2.1). Partial waves up to $L = 13$ were calculated directly by the R-matrix program, whereas for $\ell > 14$ the Born phase-shifts were taken. As noted before, difficulties arise with pseudo-resonances, in particular with those due to the correlation terms (i.e. χ_n in eq. (4.1)). These could be removed using the averaging technique of Burke et al. [10]. Clearly, by the choice of only one pseudo-state the calculations will not show any resonance structure in the region of thresholds for excitation, apart from unrealistic effects due to the single pseudo-threshold. As remarked by them, the results should be treated with caution in the energy range 19.3 to 27 eV. Indeed, the calculations do not predict the structure we found experimentally around 25 eV; besides, their data underestimate the magnitude of the cross section in that range even at 10°.

At higher energies, Fon's results are in good agreement with ours at 10°, but fall significantly below the true values at smaller angles. This is surprising, since the small angle region is dominated by polarization, for which correct description the $2\bar{p}$ pseudo-state had been adjusted intentionally. The cause cannot lie in an unsatisfactory treatment of the high partial waves; at $\ell > 14$ the incident electrons do not penetrate the inner part of the atom and thus only feel the longer range part of the electron-atom interaction. The Born values for the phase shifts can be safely used then. Looking at the many-body optical potential calculations of Scott and Taylor [32], one observes the same deviation even more pronounced. The rather large discrepancy between their results and our measurements may be partly ascribed to a crude assessment of the absorptive part in the interaction potential (see remarks made in section 2.2.5). But recall that Scott and Taylor also used one $2\bar{p}$ pseudo-state to represent the infinite sum appearing in their Σ^{P} (eq. (4.40)); the question can be asked whether the choice of only one pseudo-state might be responsible for the failure of both methods to describe the forward angular region correctly. This led Walters [30] to investigate how well the single $2\bar{p}$ pseudo-state approximates that part of the DWSBA direct amplitude which arises from the coupling of the ground state to excited states (eq. (4.30b)). For that purpose he replaced the infinite sum in eq. (4.30b) by the $2\bar{p}$ state and compared the thus calculated value with the one obtained using closure as method of solution. This procedure can be figured as a test on the 'effective completeness' of the single pseudo-state (cf. remarks made at the end of section 2.2.3). As important result it came out that the pseudo-state largely underestimates the lowest phase shifts; with other words, since low angular momenta correspond to close encounters with the region around the nucleus, it is to be concluded that the $2\bar{p}$ state does not correctly account for the short-range coupling terms (not to disturb with the short-range static interaction). As Walters showed, this deficiency explains why both methods yield too low valued cross sections. Of course, his conclusions are only justified above ≈ 50 eV, where exchange plays a minor role. At lower energies, the coupling mechanism becomes weaker and thus less sensitive to its pseudo-state substitute. Indeed, at 30 eV Scott and Taylor's method yields the correct value, whereas below ≈ 20 eV Fon's results are in agreement with experiment and other theories.

The above analysis also provides more insight in why the DWSBA approximation diverges so severely at small angles for intermediate impact energies [42]. This can be made plausible as follows. The anti-symmetry in the total electron-atom wavefunction which keeps the electrons apart at low impact energies, causes the electron-atom interaction to be weaker than it would be in direct scattering. Consequently, the net coupling of the ground-state to excited states will also be smaller. This should manifest itself in the scattering amplitude as a cancellation between the direct and exchange coupling of the ground-state to excited states. As exchange is significant for close collisions, this cancellation will occur at low angular momenta. Therefore, omission of the exchange coupling term in the DWSBA leads to erroneous results. Scott and Taylor omitted the exchange polarization, because in their model the contribution from this term was negligible (Σ^{EP} of eq. (4.40)). This is not in contradiction to Walters' findings: since the direct coupling term Σ^{P} used by them is much too weak at low angular momenta, it is not surprising that the corresponding exchange coupling will also be weak. In reality the short-range direct coupling is much stronger and so will be the exchange coupling, at low enough energy.

4.1.2. *Cusp structure around the threshold for ionization*

The new structure found in the differential cross section for small angle elastic scattering in helium is worth a separate discussion. Figure 4 shows once again the variation of the elastic signal as a function of the impact energy, now at a scattering angle of 4°. For orientation the lowest lying excitation channels have been indicated on the energy scale. The dip starts around ≈ 24 eV near the $n = 5$ excitation level, has its minimum at the ionization threshold, whereafter the yield rises again. Since the dip covers the near continuum too, it is unlikely that resonances are responsible for its appearance. Rather, we believe that its typical shape points at a threshold effect.

Obviously, passing over the threshold for each new inelastic channel will have implications for the flux in the previously opened channels, including the elastic one. As first pointed out by Wigner [43], and later confirmed by various electron impact experiments [44], the requirement on conservation of flux leads to a discontinuity in the cross section for the open channels at those energies. It is straightforward to show from the unitarity of the S-matrix that, for two open channels in both of which the angular momentum of

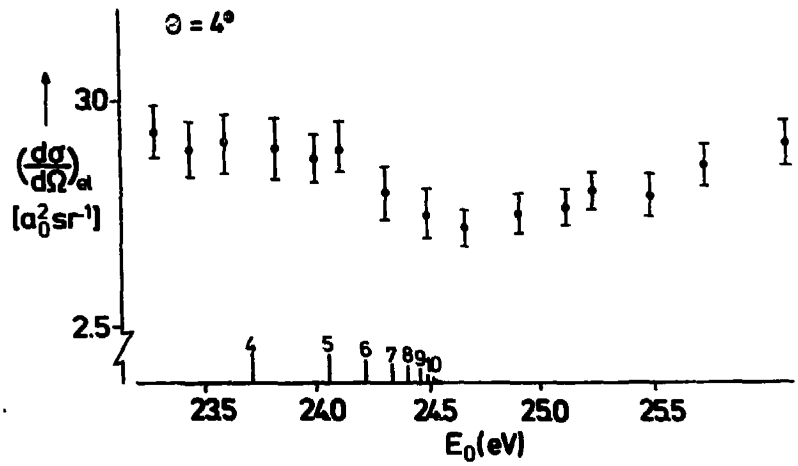

FIGURE 4

Absolute differential cross sections for elastic scattering of electrons on helium at 4° as a function of the impact energy around the threshold for ionziation.

the colliding electron is zero, the elastic cross section displays a cusp or step [45]. Although no such calculations have been performed at the ionization limit, the presence of structure may not be excluded a priori there.

Referring to figure 4, it remains to explain two significant features. The first is the remarkable width, i.e. ≈ 2 eV, of the cusp. The key to this may be found in the experiments performed by Cvejanovic and Read [46] and Spence [47]. These were meant as a test of Wannier's [48] threshold law for ionization.

According to Wannier's classical model and the later quantummechanical versions of it given by Rau [49] and Peterkop [50], the collision of an electron of incident energy E_0 slightly above the threshold I will result in ionization only if the two outgoing electrons remain tightly correlated over a large distance from the ionic core. The correlation required is such that the electrons leave the ion with near equal velocities in opposite directions. Whereas the angular correlation is stabilized by the mutual electron repulsion, the radial correlation is inherently unstable. The electron which happens to acquire a higher radial velocity than the other, will experience a lesser attraction and thus move farther and farther ahead of the other, an effect described by Rau as a 'dynamic screening'. This is a well known mechanism leading to a wealth of 'post collision' effects in other electron processes too [51].

As noted by Rau, the above mechanism applies equally well to incident energies E_o just below the ionization threshold I. Accordingly, the probability of excitation to high Rydberg states near the maximal available energy E_o should be depressed when E_o approaches I, much as the probability of ionization is reduced for E_o just above I. Indeed, with a sensitive coincidence method Cvejanovic and Read [46] observed a 'cusp' in the yield of electrons escaping with near-zero energies (<20 meV) as E_o is scanned over the ionization threshold for helium, with its minimum at $E_o = I$. In addition, with a trapped electron technique Spence [47] showed that this correlation in helium holds up to a maximal energy exchange of 2 eV between the outgoing electrons. With other words, the ionization channel is opening gradually, instead of instantaneously as with the lower excited states. As indicated by Fano [52], electrons, which do not succeed in a final escape, are trapped in bound states of high (n,l) quantum number. Consequently, the 2 eV wide range around I represents one broad absorption channel. This might explain the near equal cusp width as observed by us in the differential elastic cross section.

The second feature, i.e. the deepening of the cusp towards small momentum transfers, is harder to understand. Sofar, the most likely explanation seems to us to consider the structure as an interference between the smooth background amplitude f_{bg} and a resonant part f_{res}:

$$|f|^2 = |f_{bg} + f_{res}|^2 = |f_{bg}|^2 + |f_{res}|^2 + 2\,\mathrm{Re}[f_{bg} \cdot f_{res}^*]$$

where the * denotes complex conjugation. Since f_{bg} increases monotonously towards small angles, the interference term will be enhanced correspondingly. To test this speculation any further, complementary data at larger scattering angles are urgently needed in this energy range.

4.2. Neon

The present results are given in table III; in figures 5(a), (b) and (c) again three angles have been selected to compare with other experimental and theoretical data.

Table III. Differential (elastic) cross sections† of electron scattering on neon, in units of $a_o^2\ sr^{-1}$

θ(deg) \ E(eV)	18	20	23	25	30	40	50	70	100
0*	1.68	2.05	2.24	2.72	3.93	6.05	7.82	10.9	12.6
1	1.70	2.04	2.22	2.69	3.90	5.97	7.73	10.8	12.4
2	1.73	2.02	2.20	2.66	3.86	5.87	7.63	10.5	12.0
3	1.75	2.00	2.18	2.62	3.80	5.76	7.49	10.2	11.5
4	1.80	1.98	2.16	2.56	3.73	5.66	7.27	9.8	11.0
5	1.80	1.96	2.13	2.50	3.63	5.52	7.02	9.35	10.35
6	1.80	1.94	2.10	2.44	3.52	5.35	6.75	8.90	9.70
7	1.82	1.92	2.07	2.38	3.40	5.18	6.46	8.36	9.05
8	1.81	1.89	2.02	2.32	3.27	5.00	6.20	7.85	8.45
9	1.78	1.86	1.96	2.26	3.15	4.80	5.93	7.45	7.85
10*	1.75	1.83	1.91	2.21	3.04	4.62	5.70	7.20	7.30

* extrapolated values

† total error $\lesssim$ 7%

The experimental results of Register et al. [53] only overlap with us at 10° above 60 eV; no extrapolated data to smaller angles were reported by them. The relative cross sections were normalized using the same procedures as with helium. Due to uncertainties in the semi-empirical excitation and ionization cross section, the calibration error becomes larger at increasing impact energy and can amount up to 12%. At 100 eV, excellent agreement is found between the absolute data of Jansen et al. [34], ours, and the normalized value of Register. Figure 5(a) shows however, that below 100 eV Register's data are systematically $\approx 5-10\%$ higher. Although the difference lies within the combined error bars, we hesitate to attribute this deviation wholly to calibration problems. As it was the smallest angle within the reach of their apparatus, primary beam background, if present, might enlarge the apparent cross section [Trajmar, priv.comm.].

It is particular interesting to see if the structure, as found in helium around the ionization threshold, is also present in neon. Indeed, comparing figures 5(a), (b) and (c) one observes a step structure between 20 and 23 eV, which again manifests itself most clearly at the smallest scattering angles. However, for this atom our measurements did not reveal such a pronounced dip shape as with helium.

Let us now turn to the various theoretical calculations. McEachran and Stauffer [54] continued their work on the polarized orbital method within the adiabatic exchange approximation. Just as in helium, they obtained best results by taking exchange exactly and including the dipole part of the polarization potential only. Up to 30 eV the agreement with our results is very good; at higher impact energies the target cloud will no longer be polarized adiabatically. Besides, the influence of the open inelastic channels becomes important.

The second set of interest are the cross sections as calculated by Fon et al. [55]. In essence their approach resembled the two-state R-matrix calculations of Blum and Burke [56]; since this pioneering work the R-matrix program has undergone considerable improvements. Again a single pseudo-state of P-symmetry was chosen to include the full ground-state static dipole polarizability. As with helium, the first 13 partial waves were calculated with the R-matrix method, whereas the higher phase-shifts are obeying the Born formula. Also Burke's procedure [10] has been used to average out pseudo-resonances in the energy range from 35 eV to 120 eV. Finally, it is clear

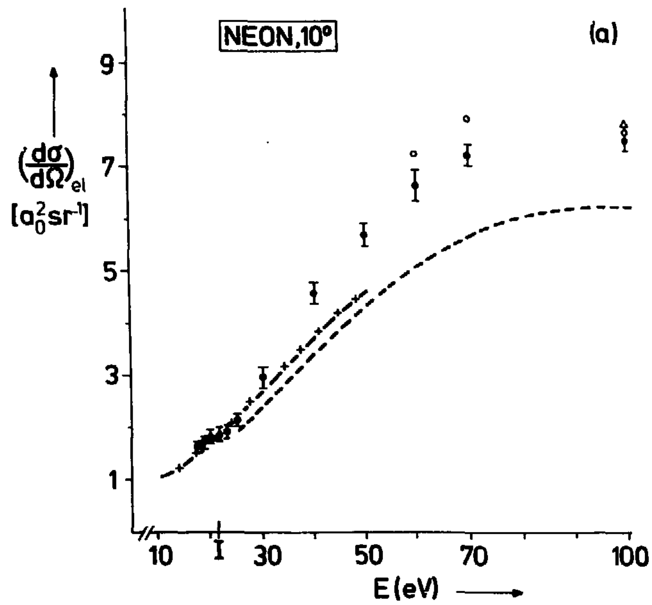

NEON,10°
(a)
$\left(\frac{d\sigma}{d\Omega}\right)_{el}$
$[a_0^2 sr^{-1}]$
E (eV)

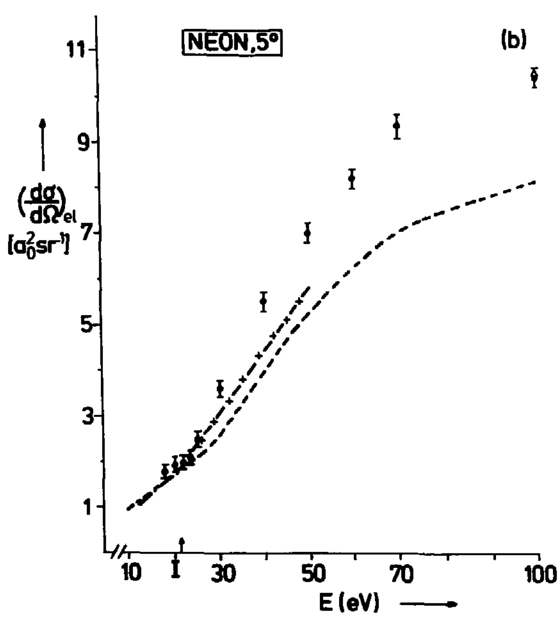

NEON,5°
(b)
$\left(\frac{d\sigma}{d\Omega}\right)_{el}$
$[a_0^2 sr^{-1}]$
E (eV)

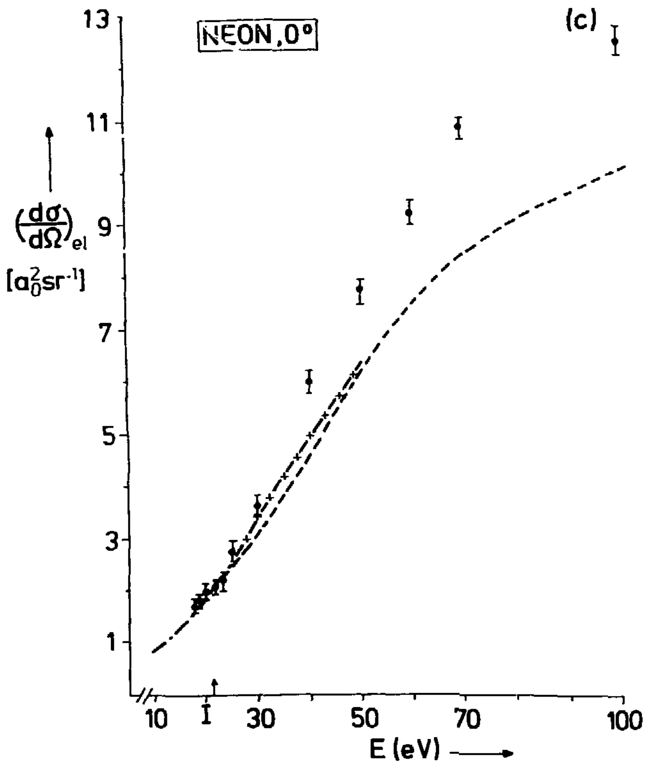

Differential cross sections for elastic electron-neon scattering as a function of the impact energy. Three scattering angles are displayed: (a) 10°, (b) 5° and (c) 0°.
Legend: Ī, present results; -----, Fon et al.; -+-+-+, McEachran and Stauffer.

that their method will not reveal any resonance structure other than that of the single pseudo-state in the inelastic threshold region from 16 to 22 eV.

Apart from the step structure we found between 20 and 22 eV, which is smoothed out by Fon's computational method, figure 5 shows his results to agree very well with our data below ≈ 30 eV. It proves the superiority of the modified R-matrix program over the early versions, since at 20 eV the calculations of Blum and Burke [56] display a completely different behaviour at small angles.

However, at increasing energy one observes a gradual deterioration of Fon's values; although no 'effective completeness' test has been performed sofar, the suspicion lies again with the pseudo-state used. Since neon possesses a large dynamical behaviour (the magnitude of the cross section rises with a factor of five over a rather limited energy range), the coupling mechanism will be strong. An incomplete account for these couplings will thus induce large errors, which indeed occur. Another point of discussion could be how sensitive the calculated cross sections are for the pseudo-resonance smoothing technique, for which Fon et al. gave no details in their paper.

4.3. Argon

The present results are given in table IV and graphically displayed in figure 6 for comparison with other data.

The perfect agreement with Jansen et al. [34] has been mentioned already in the previous chapter. DuBois and Rudd [57] are the only ones who measured absolutely at small angles, also below 100 eV. Their set-up consisted of a fixed parallel plate analyser equipped with small entrance and exit holes and a movable electron gun to adjust the scattering angle. Although their experimental procedure became rather complicated at the smaller scattering angles, yet their results can be seen to agree with our data well within the combined error bars.

Table IV. Differential (elastic) cross sections† of electron scattering on argon, in units of $a_o^2\ sr^{-1}$.

θ (deg) \ E (eV)	18	20	30	40	50	70	100
0*	51.7	50.2	53.9	57.9	59.8	66.2	69.7
1	51.0	49.6	52.7	56.4	58.2	63.9	66.4
2	50.1	48.7	51.0	54.6	56.1	60.5	61.8
3	49.2	47.5	49.5	52.6	53.7	56.6	57.1
4	48.3	46.2	47.9	50.2	51.1	52.8	52.7
5	47.4	45.0	46.3	48.0	48.8	49.3	48.9
6	46.4	43.8	44.7	45.7	46.0	45.5	44.7
7	45.5	42.9	42.9	43.3	42.9	42.1	40.1
8	44.5	41.9	41.3	40.9	40.1	38.7	35.9
9	43.4	40.9	39.6	39.3	37.6	36.0	32.3
10*	42.4	40.0	38.1	37.5	35.8	33.3	29.7

* extrapolated values

† total error $\lesssim$ 7%

When we compare our measurements with the calculations of Fon et al. [58], one observes an excellent agreement now over the whole intermediate energy range at all angles of overlap; Fon's data are even systematically a few percents higher! Clearly, this result is in contrast to what has been found for helium and neon. Again, Fon used a single P pseudo-state to account for the long range dipole polarization potential. Since the polarizability of argon is so strong, the higher ($L > 3$) phase-shifts are at least an order of magnitude larger in comparison to those of helium and neon. The 'screening' due to the Pauli exclusion mechanism, which is only effective at short range, will therefore be masked in the overall electron-argon interaction. Besides, Fon showed that excitation of his P state practically leads to the same total inelastic cross section as recommended by de Heer et al. [59]: the chosen P state represents most of the inelasticity at the intermediate energies. Both factors are necessary and apparently sufficient conditions for calculating cross sections of the correct shape and magnitude.

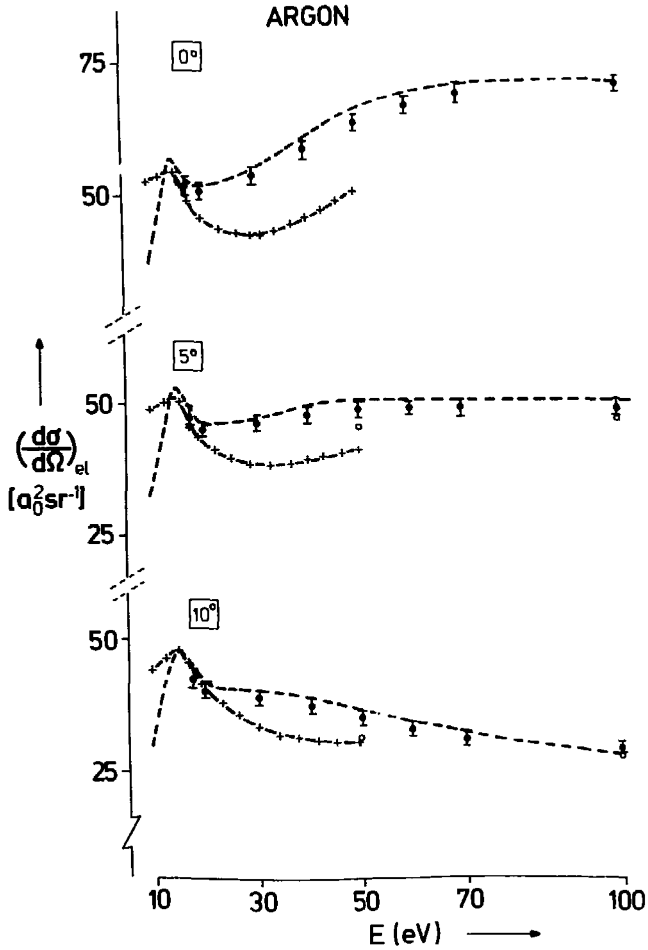

FIGURE 6

Differential cross sections for elastic electron-argon scattering as a function of the impact energy at (a) 10°, (b) 5° and (c) 0°.

Legend: ⫮ , present results; 0 , Dubois and Rudd; theoretical, -----, Fon et al.; -+-+-+-, McEachran and Stauffer.

It is worthwhile to note at this point that Fon's calculations do support the measurements of DuBois and Rudd [57], Williams and Willis [60] and Jansen et al. [34] at scattering angles $> 15°$. The most recent experiment in this angular range is that of Srivastava et al. [61]; they used the same apparatus as Register [36] did for helium and neon, but applied a different calibration technique. Surprisingly, they found substantially (up to 30%) lower cross sections at angles below $\approx 50°$. Since in turn we confirm Fon's data, one is led to the conclusion that Srivastava et al. are probably wrong at the smaller angles.

The polarized orbital calculations of McEachran and Stauffer [54] predict a much larger value for the d-wave phase shift than Fon et al.: the corresponding cross sections are too high at low energies. A refinement should consist of augmenting their adiabatic dipole polarization potential with distortion terms, accounting in some way for the kinetics of the projectile electron (as what Callaway [39] did for helium). Again, at higher impact energies the model breaks down mainly because of its one-channel formalism (i.e. inelasticity is excluded).

4.4. Krypton and xenon

Table V shows the present results, where we have rounded off the values of the cross sections to whole numbers. The only experimental data to compare with are those of Jansen et al. [34] at 100 eV, for a scattering angle of 5° and 10°; for both gases excellent agreement has been found (within 3%). Other experimental results, those of Williams and Crowe [62] and Srivastava et al. [61], lie outside our angular range. Again Srivastava's values are lower than of Williams and Jansen, as was found in discussing argon. No attempt has been made by us to extrapolate these results to angles of 10° and less, since the differential cross sections are so sharply peaked due to the large polarizability of krypton and xenon. One has to wait for reliable theoretical calculations in the intermediate energy regime for connecting the latter experi-

<u>Table V</u>. Differential (elastic) cross sections† in units of $a_o^2\ sr^{-1}$ (rounded off to whole numbers)

Energy (eV) / θ (degree)	20		25		30		40		50		70		100	
	Kr	Xe	Kr	Xe	Kr	Xe	Kr	Xe	Kr	Xe	Kr	Xe	Kr	Xe
0*	91	212	103	229	112	226	122	182	130	178	133	212	136	235
1	89	208	101	225	110	221	119	174	127	165	128	193	127	208
2	87	205	99	221	107	214	115	163	123	150	122	175	117	172
3	85	200	97	215	104	207	111	151	118	136	115	155	106	149
4	83	194	95	208	101	199	106	140	113	122	107	135	96	124
5	81	188	92	200	98	190	101	129	108	108	99	115	86	102
6	79	181	88	191	94	180	96	120	102	98	92	101	79	89
7	77	174	84	182	90	171	90	111	95	89	85	88	71	77
8	74	167	81	174	87	162	85	102	88	79	77	75	63	63
9	72	161	78	166	83	153	80	93	81	70	70	62	55	53
10*	69	154	76	159	79	145	75	85	74	61	64	51	48	44

* extrapolated values

† total error $\lesssim$ 7%

ments with our data (as could be done for argon with the help of Fon's results); such calculations are now underway.

At present, the only available calculations with which we overlap are the preliminary data of McEachran and Stauffer [63]. These polarized orbital calculations, carried out up to 50 eV, predict our cross section values surprisingly well; only at the smallest angles deviations larger than ≈10% are found. It indicates the accuracy with which they approximated the overall exchange contribution to the final cross section.

4.5. <u>Conclusions</u>

Small angle differential cross sections have been presented for elastic electron scattering from the noble gases at intermediate impact energies. The data were measured absolutely with the apparatus as described in Chapter III, claiming an accuracy of 8%. The energy range under study is characterized by a strong coupling between the elastic channel and all open inelastic channels, i.e. polarization and absorption. The results clearly unmask the deficiencies in the existing theoretical calculations in assessing these couplings. In particular, the use of one single pseudostate yields values for the cross section, which are too low in the case of helium and neon. For argon on the other hand, this approximation works quite well.

We believe that the existence of the new feature we found in the cross section for the elastic scattering on helium can be ascribed to threshold effects. This suggests a number of further experimental investigations. First, it would be interesting to obtain more detailed information on its structure (magnitude and location), by using higher energy resolution. Further, the ideas presented in connection with Wannier's threshold law for ionization should be applicable also to the inelastic scattering channels for which the atom is left in an excited state. Similar investigations would be interesting also for neon and argon, for which our results show a less pronounced dip.

We may also hope that our experimental results will stimulate further theoretical calculations of comparable or higher accuracy.

References

[1] Kingston A E and Walters H R J, Comm.Atom.Mol.Phys. XI, 177 (1982).
[2] Bransden B H and McDowell M R C, Phys.Rep. 30, 207 (1977).
[3] Burke P G and Williams J F, Phys.Rep. 34, 325 (1977).
[4] Callaway J, Adv.in Phys. 29, 771 (1980).
[5] Eissner W and Seaton M J, J.Phys.B 5, 2187 (1972).
[6] Burke P G and Mitchell J F B, J.Phys. B 6, 320 (1973).
[7] Nesbet R K, Adv.quant.Chem. 9, 215 (1975).
[8] Smith E R and Henry R J W, Phys.Rev. A 7, 1585 (1973).
[9] Fon W C, Burke P G and Kingston A E, J.Phys.B 11, 521 (1978).
[10] Burke P G, Berrington K A and Sethumar C V, J.Phys.B 14, 289 (1981).
[11] Temkin A, Phys.Rev. 107, 1004 (1957).
[12] Furness J B and McCarthy I E, J.Phys.B 6, 2280 (1973).

[13] Hara S, J.Phys.Soc.Japan 22, 710 (1967).
[14] McEachran R P and Stauffer A D, J.Phys.B 16, 255 (1983).
[15] Glauber R J, in: Lectures in Theoretical Physics, ed: Brittin W E (Interscience, New York) Vol.1, p.315 (1959).
[16] Byron F W and Joachain C J, Phys.Rev.A 8, 1267 and 3266 (1973).
[17] Walters H R J, J.Phys.B 8, L54 (1975).
[18] Dewangen D P and Walters H R J, J.Phys.B 10, 637 (1977).
[19] Kingston A E and Walters H R J, J.Phys.B 13, 4633 (1980).
[20] Winters K H, Clark C D, Bransden B H and Coleman J P, J.Phys.B 7, 788 (1974).
[21] Goldberger M L and Watson K M, in: Collision Theory (Wiley, New York) p.202 (1964).
[22] Feshbach H, Ann.Phys. 5, 357 (1958).
[23] Holt A R and Moiseiwitsch B L, J.Phys.B 1, 36 (1968).
[24] Ermolaev A M and Walters H R J, J.Phys.B 12 L779 (1979).
[25] Scott T and Bransden B H, J.Phys.B 14, 2277 (1981).
[26] Byron F W and Joachain C J, Phys.Rev.A 9, 2559 (1974).
[27] McCarthy I E, Noble C J, Phillips B A and Turnbull A D, Phys.Rev.A 15, 2173 (1977).
[28] Riley M E and Trujlar D G, J.Chem.Phys. 63, 2182 (1975).
[29] Ochkur V I, Sov.Phys. JETP 18, 503 (1964).
[30] Walters H R J, J.Phys.B 14, 3499 (1981).
[31] Gavrila M and Mandal P, Phys.Lett.A 84, 417 (1981).
[32] Scott T and Taylor H S, J.Phys.B 12, 3367 and 3385 (1979).
[33] Schneider B, Taylor H S and Yaris R, Phys.Rev.A 1, 855 (1970).
[34] Jansen R H J, de Heer F J, Luyken H J, van Wingerden B and Blaauw H J, J.Phys.B 9, 185 (1976);
Jansen R H J and de Heer F J, J.Phys.B 9, 213 (1976).
[35] Bromberg J P, J.Chem.Phys. 50, 3906 (1969).
[36] Register D F, Trajmar S and Srivastava S K, Phys.Rev.A 21, 1134 (1980).
[37] Nesbet R K, Phys.Rev.A 20 (1979).
[38] Andrick D and Bitsch A, J.Phys.B 8, 393 (1975).
[39] Labahn R W and Callaway J, Phys.Rev.A 2, 366 (1970).
[40] Onda K and Truhlar D G, Phys.Rev.A 22, 86 (1980).
[41] Fon W C, Berrington K A and Hibbert A, J.Phys.B 14, 307 (1981).
[42] Walters H R J, J.Phys.B 13, L749 (1980).
[43] Wigner E, Phys.Rev. 73, 1002 (1948).
[44] Brunt J N H, King G C and Read F J, J.Phys.B 10, 433 (1977).

[45] Massey H S W and Burhop E H S, Electronic and ionic impact phenomena, 2nd ed., Oxford (Clarendon Press), p.645.

[46] Cvejanovic S and Read F H, J.Phys.B 7, 1180 (1974).

[47] Spence D, Phys.Rev.A 11, 1539 (1975).

[48] Wannier G H, Phys.Rev. 90, 817 (1953).

[49] Rau A R P, Phys.Rev.A 4, 207 (1971).

[50] Peterkop R, J.Phys.B 4, 513 (1971).

[51] Heideman H G M and Van der Water W, Comm.on Atom.and Mol.Phys. X, 87 (1981).

[52] Fano U, J.Phys.B 7, L401 (1974).

[53] Register D F and Trajmar S, to be published in Phys.Rev.A.

[54] McEachran R P and Stauffer A D J, to be published in J.Phys.B.

[55] Fon W C and Berrington K A, J.Phys.B 14, 323 (1981).

[56] Blum K and Burke P G, J.Phys.B 8, L410 (1975).

[57] DuBois R D and Rudd M E, J.Phys.B 9, 2657 (1976).

[58] Fon W C, Berrington K A, Burke P G and Hibbert A, J.Phys.B 16, 307 (1983).

[59] de Heer F J, Jansen R H J and Van der Kaay W, J.Phys.B 12, 979 (1979).

[60] Williams J F and Willis B A, J.Phys.B 8, 1672 (1975).

[61] Srivastava S K, Tanaka M, Chutjan A and Trajmar S, Phys.Rev.A 23, 2156 (1981).

[62] Williams J F and Crowe A, J.Phys.B 8, 2233 (1975).

[63] McEachran R P and Stauffer A D J, private communication.

CHAPTER V

The forward dispersion relation for electron-helium collisions

Abstract

The dispersion relation for forward electron-helium scattering is tested numerically with the measured values for the total and small angle elastic cross sections. The discrepancy function, which accounts for contributions from the non-Born part of the exchange amplitude, vanishes first at impact energies above 500 eV. It displays a peaked structure just above the threshold for single ionization, which indicates an enhancement of exchange coupling occurring there. A mathematical stabilization technique has been applied to invert the discrepancy function. The discontinuous behaviour of the exchange amplitude along the negative real energy axis could be derived qualitatively herewith. Further theoretical research is necessary for tracing the singularities, which are responsible for its typical shape.

1. Introduction

This last chapter will be concerned with a numerical test of the electron-helium forward dispersion relation and its consequences for the discrepancy function. In chapter I we already introduced these concepts to the reader, thereby referring to the historical context in which dispersion relations were developed. We also pointed out why the original formulation by Gerjuoy and Krall [1] (cf. eq. (1.6)) failed in describing electron-atom collision processes: it is the rearrangement part of the scattering amplitude which complicates matters. This followed from a preliminary study which we carried out some years ago for both electron and positron scattering on helium and atomic hydrogen [2,3]. We could show that the Gerjuoy-Krall dispersion relation is correct for positron scattering, but for electrons this is the case only at high enough energies, where exchange can be neglected. Those results stimulated theoretical research into the exchange amplitude and appealed for new measurements of both total and differential elastic cross sections.

Having measured total cross sections σ_t over a wide energy range with the apparatus as described in chapter II, Blaauw [4] analysed the electron-helium dispersion relation more profoundly in cooperation with Tip [5,6]. It appeared that the exchange amplitude is non-analytic along part of the negative axis in the complex energy plane. The lack of small angle elastic cross sections at the intermediate energies, where exchange is still important, prevented Blaauw from making explicit statements on the discrepancy function.

On the other hand, with the small angle data as discussed in the previous chapter, we are in the position to perform a complete experimental test on its shape and magnitude.

The chapter has been organized as follows. In section 2 we derive the electron-helium dispersion relation with its supplementary discrepancy function. The actual evaluation of the discrepancy function is done in section 3. As such it partly replaces, partly complements Blaauw's [4] analysis with both revised* and completely new experimental data. In section 4 its shape and magnitude are discussed. Besides, an attempt is made to invert the discrepancy function, which is an integral expression, to the imaginary part of the scattering amplitude. A modified version of the regularization method of Phillips and Tuhonov [7] has been used for that purpose [8]. Linking on to the discussion on helium, we critically comment upon the recent study by Dumbrajs and Martinis [9] on the discrepancy function for atomic hydrogen. Finally, in section 5 the main conclusions from the present study on the dispersion relation are summarized.

2. Dispersion relations for electron-atom forward scatterring

As described in chapter 1, it is essential to assess the analytic properties of the scattering amplitude before it is subjected to a contour integration. There it was stated that the various theoretical studies to this analyticity problem did not yield the same results; eventually Tip [5,6] was able to settle the question convincingly with the help of advanced mathematical tools delivered by Combes and coworkers [10]. The interested reader may find an extensive account of their procedure in the thesis of Blaauw [4]. In this section we shall briefly recall Tip's conclusions and show how they are used in a stepwise derivation of the proper dispersion relation.

Consider the elastic forward scattering of an electron from a ground-state atom (the nucleus is assumed to be infinitely heavy). The total number of electrons is N, so that the nuclear charge is $Z = N - 1$; units are such that $\hbar = e^2 = 1$ and m_e, the electronic mass, is ½. The electronic position vectors $\underline{x}_j$ (associated momenta $\underline{p}_j$) have the nucleus as origin. The full Hamiltonian

*The σ_t values derived by Blaauw [4] were 2.5% low due to an incorrect assessment of the thermal transpiration effect (cf. Ch.II, 3.1).

$$H = \sum_{j=1}^{N} \underline{p}_j^2 - \sum_{j=1}^{N} \frac{Z}{|\underline{x}_j|} + \sum_{i>j} |\underline{x}_i - \underline{x}_j|^{-1} \tag{5.1}$$

then acts in the Hilbert space $H = L^2(R^{3N})$. The interaction between electron i and the atom made up from the remaining particles is

$$V^{i,at} = \sum_{j \neq i} |\underline{x}_i - \underline{x}_j|^{-1} - \frac{Z}{|\underline{x}_i|} \; . \tag{5.2}$$

The spectrum $\sigma(H)$ of H consists of a finite number of isolated eigenvalues (the negative ion bound states) and a remaining part consisting of its continuum spectrum and, if present, continuum embedded eigenvalues. For z outside $\sigma(H)$ the Green's operator $G(z) = [z-H]^{-1}$ is a bounded operator and for such z one finds for the direct scattering amplitude

$$f^d(z) = -2\pi^2 < \psi_1 | V^{1,at} | \psi_1 > - 2\pi^2 < \psi_1 | V^{1,at} \; G(z) \, | V^{1,at} | \psi_1 > =$$

$$= f_B^d + \phi^d(z) \quad , \tag{5.3}$$

and for the exchange (or rearrangement) amplitude

$$f^r(z) = -2\pi^2 < \psi_2 | V^{1,at} | \psi_1 > \; - 2\pi^2 < \psi_2 | V^{1,at} \; G(z) \; V^{1,at} | \psi_1 > =$$

$$= f_B^r(z) + \phi^r(z) \quad . \tag{5.4}$$

In eq. (5.3) and (5.4) we have splitted the amplitudes into a Born part f_B and a non-Born part ϕ. Furthermore

$$\psi_j(\underline{x}_1, \ldots, \underline{x}_N) = (2\pi)^{-3/2} \exp[i\underline{k}.\underline{x}_j] \; \cdot$$

$$\phi_o(\underline{x}_1, \ldots, \underline{x}_{j-1}, \underline{x}_{j+1}, \ldots, \underline{x}_N) \tag{5.5}$$

is a product of a plane-wave state (momentum $\underline{k}$, energy k^2) and the properly symmetrized atomic ground state (energy $\varepsilon_o < 0$). The scattering amplitude for the process under consideration is a linear combination of the direct amplitude f^d and the rearrangement amplitude f^r.

It is not clear a priori that $f^d(z)$ and $f^r(z)$ exist. This, however, is indeed the case. For the Born parts this follows directly from the special nature of the ground state wavefunctions (boundedness and exponential decay) and for the non-Born parts from the square integrability of $V^{i,at}\ \psi_i$.

From (eq. 5.3) and (5.4) the physical amplitudes are obtained by substituting $z = k^2 + \varepsilon_o + i\varepsilon$ and taking the limit $\varepsilon \to 0$. This is trivial for the real quantities f_B^d and f_B^r, the first of these being independent of z and $\underline{k}$, whereas the second only depends on k. For the ϕ's the situation is more complicated (see Combes and Tip [6]).

Having decomposed the amplitudes in a Born and non-Born part, the question is raised as to the analytic behaviour of ϕ^d and ϕ^r as k is continued in the upper half complex plane, i.e. $k \to \xi$, $\mathrm{Im}\xi > 0$. The general approach Combes [10] follows towards this problem is in terms of analytic continuations of some one-parameter unitary transformation groups. More specifically, a dilatation group, which transforms both the position and the momentum operators, as well as a boost group, which leaves position operators invariant but 'boosts' some of the momenta, are used. We skip the mathematical details here and withstand with presenting the two major conclusions:

(i) ϕ^d is analytic outside $\sigma(H)$ everywhere in the upper half plane, including the negative real axis; one thus encounters the same situation as in pure potential scattering;

(ii) ϕ^r is analytic in a domain consisting of the complex plane <u>outside</u> the real axis, combined with the open interval $(\varepsilon_o - B, \varepsilon_o)$; B is equal to the difference in energy of the threshold for single ionization and the ground state ε_o.

Possible remaining singularities in the region $(\varepsilon_o - B, \varepsilon_o)$ are only the familiar poles associated with bound states of the negative ion. The conclusion that ϕ^r is not necessarily regular along the negative energy axis has important consequences as discussed below. The dilatation formalism has the

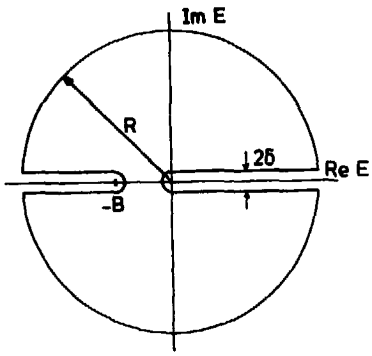

FIGURE 1

The integration contour for the derivation of the forward dispersion relation ($R \to \infty$ and $\delta \to 0$).

drawback that it is not explicit about the nature of eventual singularities there; we shall come back to this in section 4.

With these results at hand we can proceed according to the procedure as described in chapter I, eq. (1.2) - (1.3) for the contour integral in the complex energy upper half plane, sketched in figure 1.

For the direct part

$$\frac{f^d - f^d_B}{E'-E} \equiv \frac{\phi^d}{E'-E} ,$$

which is analytic outside the right-hand cut, this gives

$$\mathrm{Re}\ \varphi^d(E) = \frac{1}{\pi} P \int_0^\infty dE' \frac{\mathrm{Im}\ \phi^d(E')}{E'-E} = \frac{1}{\pi} P \int_0^\infty dE' \frac{\mathrm{Im}\ f^d(E')}{E'-E} \quad (5.6)$$

On the other hand, the rearrangement part

$$\frac{f^r - f^r_B}{E'-E} \equiv \frac{\phi^r}{E'-E} ,$$

yields an extra contribution $\Delta(E)$ to the principle value integral from the contour along the negative real energy axis:

$$\mathrm{Re}\ \phi^{r}(E) = \frac{1}{\pi}\, P \int_{0}^{\infty} dE' \ \frac{\mathrm{Im}\ \phi^{r}(E')}{E' - E} + \Delta(E) =$$

$$\frac{1}{\pi}\, P \int_{0}^{\infty} dE' \ \frac{\mathrm{Im}\ f^{r}(E')}{E' - E} + \Delta(E) \ . \tag{5.7}$$

The quantity

$$\Delta(E) = \int_{-\infty}^{-B} dE' \ \frac{\mathrm{Im}\ \phi^{r}(E')}{E' - E}$$

is called the discrepancy function. Combining eq. (5.6) and (5.7) gives

$$\mathrm{Re}\ [\phi^{d}(E) + \lambda\phi^{r}(E)] = \frac{1}{\pi}\, P \int_{0}^{\infty} dE' \ \frac{\mathrm{Im}[f^{d}(E') + \lambda f^{r}(E')]}{E' - E} + \lambda\Delta(E) \ . \tag{5.8}$$

Since

$$f(E) = f^{d}(E) + \lambda f^{r}(E) = f^{d}_{B} + \lambda f^{r}_{B}(E) + \phi^{d}(E) + \phi\lambda^{r}(E)$$

we find

$$\mathrm{Re}\ f(E) = f^{d}_{B} + \lambda f^{r}_{B}(E) + \frac{1}{\pi}\, P \int_{0}^{\infty} dE' \ \frac{\mathrm{Im}\ f(E')}{E' - E} + \lambda\Delta(E) \ . \tag{5.9}$$

For helium $\lambda = -1$, for atomic hydrogen $\lambda = -\frac{1}{2}$. Eq. (5.8) as it stands is not complete: a sum term accounting for the contributions from eventual negative ion bound states has to be added (cf. eq. (1.3)). Since we restrict the present numerical analysis to helium, this extra term may be omitted.

The real and imaginary parts are related to the elastic differential cross section at angle zero through the relation (cf. eq. (1.5)):

$$\left(\frac{d\sigma}{d\Omega}\right)_{el}(E,0) = [\mathrm{Re}\ f(E,0)]^{2} + [\mathrm{Im}\ f(E,0)]^{2} \ , \tag{5.10}$$

whereas the total (elastic + inelastic) cross section σ_t is related to the imaginary part through the optical theorem as (cf. eq. (1.4))

$$\mathrm{Im}\ f(E,0) = \frac{k}{4\pi}\ \sigma_t(E)\ . \tag{5.11}$$

The electron-helium dispersion relation then finally reads (cf. eq. (1.6)):

$$\mathrm{Re}\ f(E,0) = f_B^d - f_B^r(E) + \frac{k}{4\pi^2}\ P \int_0^\infty dE'\ \frac{\sigma_t(E')}{E'-E} - \Delta(E)\ . \tag{5.12}$$

In the next section we shall evaluate $\Delta(E)$ for those energies, where it has non-zero values.

3. Evaluation of the discrepancy function

We have reached the point, where accurate values for $\Delta(E)$ are derived from eq. (5.12) by substitution of the appropriate experimental data for σ_t and

$$\left(\frac{d\sigma}{d\Omega}\right)_{el}(E,0)$$

and the best available theoretical values for f_B^d and $f_B^r(E)$. For clarity of presentation we shall discuss these four entries separately.

3.1. Evaluation of the principal-value integral

With the apparatus as described in chapter II we have measured σ_t between 17.5 and 750 eV [11]. The data agreed particularly well (within 2%) with Kennerly and Bonham [12] at overlapping energies. Given the nearly equal (within 2 - 4%) results among the most recent data sets at the boundaries of their respective measurement ranges, it is easy to compile an accurate set σ_t values from 0 - 750 eV impact energy.

For the principal-value integral we approximated the thus chosen σ_t data with polynomials in different energy intervals as given below (σ_t in a_0^2; k^2 in Ryd):

$E = 0 - 7$ eV $\quad \sigma_{tot} = 17.21 + 30.36\ k - 53.78\ k^2 + 24.93\ k^4$

$E = 3 - 15$ eV $\quad \sigma_{tot} = 0.32\ k^{-4} - 3.69\ k^{-2} + 38.41 - 39.45\ k^2 + 25.10\ k^4 - 7.00\ k^6$

$E = 12 - 25$ eV $\quad \sigma_{tot} = -27.44\ k^{-4} + 94.45\ k^{-2} - 94.11 + 50.24\ k^2 - 9.44\ k^4 - 0.03\ k^6$

$E = 20 - 250$ eV $\quad \sigma_{tot} = -5.55\ k^{-4} + 16.36\ k^{-2} + 2.38 - 0.10\ k^2 + 0.004\ k^4$

$E = 150\text{–}700$ eV $\quad \sigma_{tot} = -549.67\ k^{-6} + 164.17\ k^{-4} + 2.40\ k^{-2} + 2.45 - 0.05\ k^2$

$E = 500 - \infty \quad \sigma_{tot} = 19.40\ k^{-2} + 9.46\ k^{-2}\ \ln k^2 - 82.0\ k^{-4} + 7.32\ k^{-6}$

The first five polynomials have been calculated by a least-squares method, which is capable of taking into account the weights of the data points. This implies the possibility of getting a good fit at the boundaries of the various intervals. The principal-value has been calculated analytically. This method introduces no significant error provided that the energy E at which the integral is evaluated does not lie too close to the boundaries of the interval. In such cases the boundary between the relevant intervals has been shifted. The coefficients of the expressions have been fitted in such a way that, extending the length of one interval by 15% at the side of the critical boundary, a deviation of at most 3% is introduced in the σ_t value of the new end-point as compared to the σ_t value of the expression used before. The experimental values of Im f(E,0) in table I correspond through relation (5.11) to the values of the polynomials used for the interpolation.

Since the principal-value integration extends to infinity, one has to establish the behaviour of σ_t for high energies. It is obvious to take the Born approximation for this purpose as it is a high energy approximation. This is reflected in the last polynomial, which is the sum of the theoretical Born cross sections of Inokuti and McDowell [13] for total elastic scattering and of Kim and Inokuti [14, eq. (49c)] for total inelastic scattering. When comparing his previous σ_t data with these calculations, Blaauw [4] found a constant value of 0.95 for the ratio between them above 200 eV collision energy. He attributed this difference to another high energy approximation in Inokuti's calculations, i.e. use of closure in the summation of projector operators (see remarks in section 4.2 of the previous chapter). Although this objection certainly counts at lower energies, it does not explain the apparent constant deviation above ≈ 300 eV. As noted before, the data used by Blaauw were 2.5% too low, so the actual difference is only 2%, a far less alarming figure. Besides, the contribution from the high energy part to the integral is heavily damped by the denominator in the integrand. Therefore, we could safely adopt Inokuti's expression for the present evaluation.

The result of the integration is presented in table I; its accuracy is estimated to be better than 4%.

3.2. Evaluation of Re f(E,0)

In order to determine this quantity, we distinguish again three collision energy intervals, as we did in the previous chapter for the differential cross section

$$\left(\frac{d\sigma}{d\Omega}\right)_{el}(E,0):$$

(a) energies below the first inelastic threshold,
(b) intermediate energies up to 100 eV, and
(c) the high energy regime above 100 eV.

3.2.1. *Collision energies below the first inelastic threshold*

Below 18 eV no direct experimental material exists for

$$\left(\frac{d\sigma}{d\Omega}\right)_{el}(E,\theta)$$

at θ near zero degrees. The experiments of Andrick and Bitsch [15], McConkey and Preston [16] and Register et al. [17] all stop at 15 - 20°. The best one can do is to rely upon the variational calculations of Nesbet [18] for constructing Re f(E,0) at $E < 18$ eV. This choice is certainly justified, since both we at small angles and Register et al. and Andrick and Bitsch at larger scattering angles, all confirm Nesbet's data within a few percent.

Nesbet showed that for energies up to 19.1 eV,

$$\left(\frac{d\sigma}{d\Omega}\right)_{el}(E,\theta)$$

is fixed with an accuracy of one percent by calculating only the s and p wave phase shifts (i.e. δ_o and δ_1) with his model and the remaining δ_ℓ, $\ell > 2$ with the Born formula (eq. (1.9)):

$$\tan \delta_\ell = \frac{\pi\alpha_d \; k^2}{(2\ell+3)(2\ell+1)(2\ell-1)} \; , \; \ell > 1 \qquad (5.13)$$

where α_d is the dipole polarizability (= 1.384 a_o^3 for helium [19]). In his actual calculations of the scattering amplitude $f(E,\theta)$ Nesbet applied Thomson's formula [20], where, with the further approximation of replacing $\tan \delta_\ell$ by $\sin \delta_\ell$, the sum of contributions to $f(E,\theta)$ for all δ_ℓ with $\ell > 2$ is given in closed form:

$$f(E,\theta) = \frac{1}{k} \sum_{\ell=0}^{2} (2\ell+1) \; e^{i\delta_\ell} \sin \delta_\ell \; P_\ell(\cos\theta) +$$

$$\pi\alpha_d \; k\left[\frac{1}{3} - \frac{1}{2}\sin\frac{\theta}{2} - \sum_{\ell=1}^{2} \frac{1}{(2\ell+3)(2\ell-1)} P_\ell(\cos\theta)\right]. \qquad (5.14)$$

From this formula a simple relation is deduced for Re $f(E,0)$

$$\mathrm{Re}\; f(E,0) = \frac{1}{2k} \sum_{\ell=0}^{2} (2\ell+1) \sin 2\delta_\ell + \frac{3}{35}\pi\alpha_d \; k \; . \qquad (5.15)$$

By inserting Nesbet's values for δ_o and δ_1 and the Born value for δ_2, we could derive the appropriate values for Re $f(E,0)$. The results, accurate within 2%, are given in Table I under the entry 'theoretical'.

3.2.2. *Intermediate collision energies*

Between 18 and 100 eV we can use the experimental data as presented in table II of the previous chapter. Scattering angles below 1° were inaccessible to us; a simple least squares curve fitting procedure yielded the required values for

TABLE II. Small angle differential cross sections for elastic electron-helium scattering at high collision energies

Angle	E = 150 eV		E = 200 eV				E = 300 eV				E = 500 eV			
	J	This* work	J	Br	This* work	EBS	J	Br	This* work	EBS	J	Br	This* work	EBS
0°	-	(2.90)	-	-	(2.76)	3.08	-	-	(2.40)	2.51	-	-	(2.00)	1.98
1°	-	2.76	-	-	2.55	2.83	-	-	2.13	2.23	-	-	1.67	1.66
2°	-	2.60	-	2.30	2.34	2.58	-	1.85	1.87	1.97	-	1.41	1.41	1.41
3°	-	2.41	-	2.17	2.17	2.35	-	1.68	1.70	1.74	-	1.23	1.19	1.21
5°	2.01	2.04	1.68	1.73	1.74	1.94	1.28	1.31	1.31	1.39	0.91	0.94	0.93	0.94
10°	1.36	1.36	1.08	1.08	1.08	1.23	0.79	0.81	0.80	0.85	0.55	0.57	0.56	0.57

*relative measurements, normalized on the absolute data of Jansen and Bromberg at 10°; numbers in parentheses are extrapolated values.

J : Jansen et al. [21]

Br : Bromberg [22]

EBS : Eikonal Born Series calculations of Byron and Joachain [23].

$$(\frac{d\sigma}{d\Omega})_{el}(E,0).$$

These data have an experimental inaccuracy of at most 7%. The next step is to apply the optical theorem, as given in eq. (5.11), to σ_t for calculating Im $f(E,\theta)$. Substitution of this value together with

$$(\frac{d\sigma}{d\Omega})_{el}(E,0)$$

in eq. (5.10) finally yields Re $f(E,0)$. The results are presented in table I under the entry 'experimental'.

Note that the structure in

$$(\frac{d\sigma}{d\Omega})_{el}(E,0)$$

around the threshold for ionization is propagated to Re $f(E,0)$. Although this structure is considerably damped by the non-zero value of Im $f(E,0)$ through eq. (5.10), it has still a dramatic effect on the exchange amplitude, as we shall see in section 4.

3.2.3. *High collision energies*

Between 150 and 500 eV we performed relative measurements for

$$(\frac{d\sigma}{d\Omega})_{el}(E,\theta)$$

in the angular range $\theta = 0.5 - 10°$. These could be made absolute by normalization on Jansen's [21] and Bromberg's [22] data, who measured absolutely down to respectively 5° and 2° as smallest scattering angle. Jansen and Bromberg agreed within 2% with each other at 10° at all common collision energies; so we chose as calibration standard the mean value from both experiments for

$$(\frac{d\sigma}{d\Omega})_{el}(E,\ 10°)\ .$$

TABLE I. The evaluation of the forward dispersion relation for $e^- - He$ scattering.

E(eV)	Re f(E,0) experimental	Re f(E,0) theoretical	Im f(E,0)	$\frac{P}{\pi}\int_0^\infty dE' \frac{Im\ f(E',0)}{E'-E}$	f_B^d	$f_b^r(E)$	Δ(E)
0.60		-0.92(±0.05)	0.35	2.53(±0.06)	0.791	3.59	0.65(±0.08)
1.50		-0.64(±0.02)	0.57	2.45(±0.06)		3.25	0.63(±0.08)
2.20		-0.46(±0.02)	0.68	2.38(±0.06)		3.02	0.61(±0.08)
2.75		-0.31(±0.01)	0.75	2.33(±0.06)		2.85	0.58(±0.07)
3.40		-0.17(±0.01)	0.82	2.26(±0.06)		2.66	0.56(±0.07)
3.90		-0.07(±0.01)	0.86	2.21(±0.06)		2.53	0.55(±0.07)
5.0		0.13(±0.01)	0.93	2.13(±0.05)		2.26	0.53(±0.06)
6.0		0.30(±0.01)	0.98	2.05(±0.05)		2.05	0.49(±0.06)
7.0		0.43(±0.02)	1.02	1.97(±0.05)		1.86	0.47(±0.07)
9.0		0.64(±0.02)	1.06	1.84(±0.05)		1.54	0.45(±0.07)
11.0		0.82(±0.03)	1.08	1.72(±0.05)		1.27	0.42(±0.07)
13.0		0.96(±0.03)	1.09	1.62(±0.05)		1.06	0.39(±0.06)
15.0		1.06(±0.03)	1.08	1.54(±0.04)		0.88	0.39(±0.06)
17.0		1.15(±0.03)	1.06	1.48(±0.04)		0.74	0.38(±0.06)
18.0	1.19(±0.06)		1.05	1.46(±0.04)		0.68	0.38(±0.07)
20.0	1.27(±0.06)		1.04	1.41(±0.04)		0.56	0.37(±0.07)
22.5	1.37(±0.06)		1.02	1.36(±0.04)		0.45	0.36(±0.07)
25.0	1.34(±0.06)		1.02	1.31(±0.03)		0.36	0.40(±0.07)
27.5	1.42(±0.06)		1.01	1.27(±0.03)		0.28	0.36(±0.07)
30.0	1.47(±0.06)		1.00	1.24(±0.03)		0.22	0.33(±0.07)
35.0	1.56(±0.07)		0.98	1.18(±0.03)		0.12	0.29(±0.07)
40.0	1.62(±0.07)		0.96	1.13(±0.03)		0.05	0.26(±0.07)
50.0	1.66(±0.07)		0.94	1.06(±0.03)		-0.04	0.23(±0.07)
60.0	1.69(±0.07)		0.91	1.01(±0.03)		-0.08	0.20(±0.07)
70.0	1.65(±0.07)		0.89	0.96(±0.02)		-0.11	0.20(±0.07)
80.0	1.63(±0.07)		0.86	0.92(±0.02)		-0.12	0.20(±0.07)
90.0	1.59(±0.07)		0.86	0.89(±0.02)		-0.13	0.19(±0.07)
100.0	1.58(±0.07)		0.85	0.86(±0.02)		-0.12	0.18(±0.07)
150.0	1.59(±0.07)		0.82	0.74(±0.02)		-0.12	0.15(±0.07)
200.0	1.46(±0.07)		0.79	0.66(±0.02)		-0.10	0.09(±0.07)
300.0	1.37(±0.06)		0.74	0.54(±0.02)		-0.08	0.04(±0.07)
500.0	1.24(±0.06)		0.66	0.41(±0.02)		-0.05	0.01(±0.06)

All terms in units of a_o.

Table II shows the results together with the eikonal Born series (EBS) calculations of Byron and Joachain [23]. Our data possess a slightly steeper slope as compared with Jansen and Bromberg. As expected the EBS values are too high at the lower energies, but they merge perfectly with experiment at 500 eV.

It is now straightforward to extrapolate the measured slope in the data from a half to zero degrees. As above, substitution of

$$\left(\frac{d\sigma}{d\Omega}\right)_{el}(E,0)$$

in eq. (5.10) leads to Re f(E,0), with a quoted accuracy of 5%.

3.3. Evaluation of the Born amplitudes f_B^d and $f_B^r(E)$

The last quantities we need for calculating $\Delta(E)$ are the Born approximations to the elastic direct f^d and exchange $f^r(E)$ forward scattering amplitudes.

For electron-helium scattering the value for f_B^d is well-established (Pekeris [24], Kim and Inokuti [25]): $0.7913 \pm 0.0002\ a_o$. It has a fixed value, independent of the collision energy.

The Born exchange term has been calculated by Bransden and McDowell [26] and Hutt et al. [27]. The latter found best results with configuration interaction wave functions; these have been adopted by us, see table I.

Having collected all the necessary ingredients for eq. (5.12) the discrepancy function can be calculated; table I shows the final data on $\Delta(E)$.

4. Discussion of the discrepancy function

The discrepancy function for electron-helium forward scattering is shown in figure 2. It accounts for the contributions from the non-Born part of the exchange amplitude, as it is defined in eq. (5.7). The overall shape is that of a monotonic decreasing function and vanishes at energies above ≈ 500 eV. It fits in the picture of exchange scattering, since this mechanism is feeded by overlap of the projectile and atomic electron wave functions, which occurs mainly when the electron velocities are of comparable magnitude.

As expected, around the threshold for single ionization, I, the same structure as in the differential cross section is present, but of reversed and reduced size. Actually, it is induced by Re f(E,0) and not by Im f(E,0), since within the experimental accuracy of 3% no such structure was found in the total cross section σ_t. On the contrary, even if σ_t had a pronounced structure around I it would not affect $\Delta(E)$ seriously. This we investigated numerically by evaluating the extra

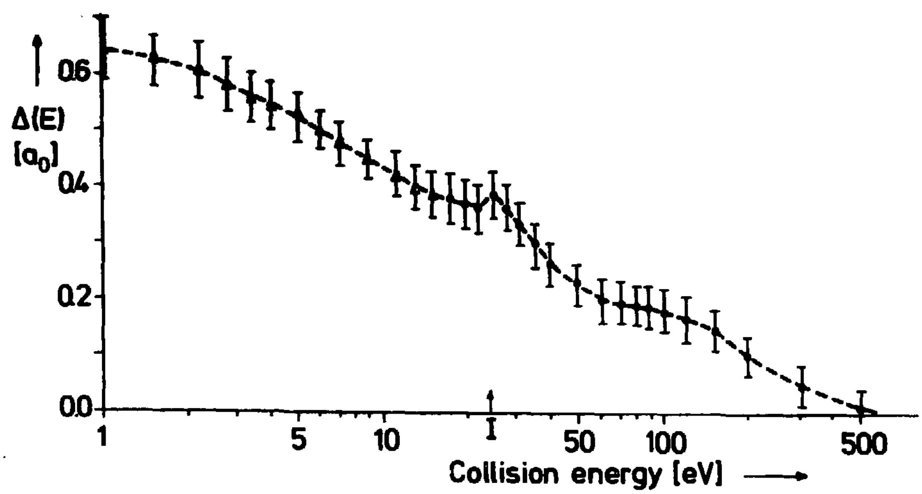

FIGURE 2

The discrepancy function for electron-helium scattering:
•, using present σ(E,0) and ▲, using theoretical [18] σ(E,0).

contribution to the principal-value integral which a Gaussian shaped peak or dip would give. No more than half a percent of the actual value is found with a relative peak height of 10% and half width 1 eV imposed on the smooth σ_t background. Clearly such structure, if present, is effectively washed out by the long tails of σ_t as E goes to infinity as integration limit.

That the structure reappears in $\Delta(E)$, i.e. in the exchange amplitude $\phi(z)$ is not surprising. The correlated motion between the projectile and one of the atomic electrons can be considered as a strong exchange mechanism, in which both electrons participate as equal partners.

The question is raised now whether more specific information can be gained from $\Delta(E)$ in figure 2 with respect to the underlying exchange processes. It cannot yet be answered unambiguously; let us therefore recall the expression for $\Delta(E)$:

$$\Delta(E) = \frac{P}{\pi} \int_{-\infty}^{-B} dE' \, \frac{\mathrm{Im}\, \phi^r(E',0)}{E' - E} \,, \tag{5.16}$$

where B is equal to I, the energy for single ionization. The imaginary part stands for the discontinuity $\rho(E',0)$ of the non-Born part of the exchange amplitude $\phi^r(z)$ across the left hand cut (see figure 1):

$$\rho(E') = \lim_{\delta \to 0} \left[\phi^r\Big(z = k \ \exp[i(\tfrac{1}{2}\pi - \delta)]\Big) - \right.$$
$$\left. - \phi^r\Big(z = k \ \exp\ i(\tfrac{1}{2}\pi + \delta)]\Big) \right] \tag{5.17}$$

The above expression contains among ohters bound-state eigenfunctions dilated over $\pm \frac{\pi}{2}$ so that their exponential decay is changed into an oscillating behaviour. This complicates actual computations for (5.17) considerably and sofar no concrete numbers have been reported for helium.

On the other hand, since we have exact values for $\Delta(E)$, inverting eq. (5.16) would reveal the behaviour of $\rho(E')$ and might point at eventual singularities in $\phi^r(E')$. Unfortunately, eq. (5.16) is an integral of the Fredholm type which belongs to the class of 'ill-posed' problems, i.e. there is no

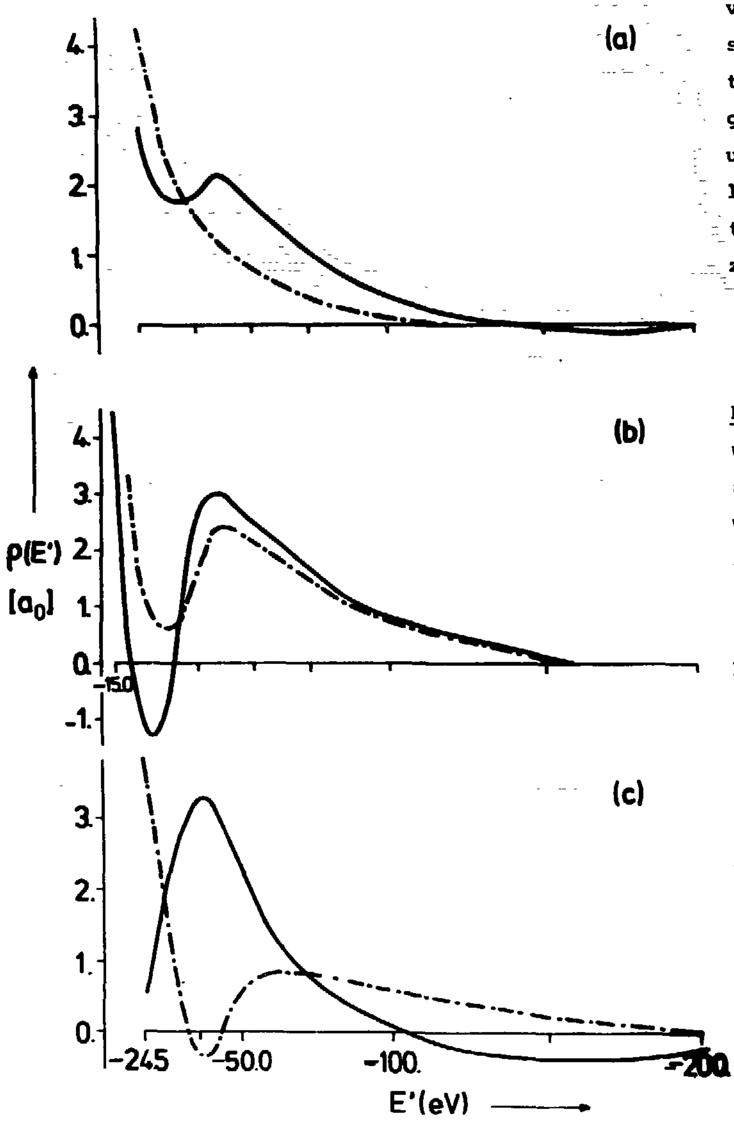

FIGURE 3(a). Results obtained for $\rho(E')$ after inversion of eq. (5.16): solid line, using the actual $\Delta(E)$ values as in figure 2, and broken curve, using the same $\Delta(E)$ values but with removal of the peak around the ionization threshold.

FIGURE 3(b). The same as under (a) for the unsmoothed $\Delta(E)$ values, but with displacement of the lower boundary B of the integration interval: solid line, B = -15 eV and broken curve, B = -20 eV.

FIGURE 3(c). The same as under (a), but with shifting the peak towards -20 eV, solid line, and -30 eV, broken curve.

unique solution: the set of solutions of the zero space, i.e. $\rho_o(E')$ with $\Delta(E) \equiv 0$, will not be empty. Therefore, the general solution of eq. (5.16) is formed by linear combinations of $\rho_o(E')$ added to a particular solution $\rho(E')$. Besides, such solutions will be unreliable: due to the strong damping factor $[E' - E]^{-1}$ in the integrand a small shift in the value of $\Delta(E)$ calls for large variations in $\rho(E')$. Yet, there exists a technique with inherent stabilization properties, the regularization method of Phillips and Tuhonov [7], which could be applied to our problem successfully [8]. Herewith, the second derivative of $\rho(E')$, multiplied by a regularization parameter α, is inserted at the right-hand side of eq. (5.16). Minimalization of this functional with respect to α then leads to an unique solution $\rho(E')$.

The 'most stable' result obtained with this technique is shown in figure 3(a). The displayed values for $\rho(E')$ must not be taken for absolute: only the general shape may be considered. Note the broad bump between $E' = -40$ and -60 eV. In order to be sure that it reflects a real physical effect instead of being an artefact from the employed inversion technique, the following three tests have been carried out.

First, the structure in the $\Delta(E)$ values around the threshold I was smoothed out, whereafter the program was run again. Figure 3(a) shows the consequences for $\rho(E')$ of this operation: the big bump has disappeared! So, its existence is directly related with the small structure in $\Delta(E)$.

Second, we investigated how critical the branch point B is for the particular shape and magnitude of $\rho(E')$. Figure 3(b) shows the resulting graphs when B is set to -20 and -15 eV respectively. The bump becomes more pronounced and asymmetric as B decreases, but its maximum remains fixed at ≈ -50 eV.

Third and last, we shifted the structure in $\Delta(E)$ from I to a lower respectively higher position on the energy axis: the whole $\rho(E')$ pattern is shifted along in the same direction, as seen in figures 3(c) for -20 and -30 eV.

From these tests one may conclude that there indeed exists a one-to-one relationship between the structure in $\Delta(E)$ and the bump in $\rho(E')$.

As said before, this solution will not be unique for the actual $\Delta(E)$, as given in eq. (5.16). One may expect zero solutions $\rho_o(E')$, constrained to $\Delta(E) = 0$ for any value E and a fall-off faster than $|E'|^{-\frac{1}{2}}$ as $|E'|$ increases, to be of a highly oscillatory character. Clearly, such solutions cannot have any relevance to our problem. Therefore, the solution as shown in figure 3(a) can be assumed as quite realistic.

When we now return to the question asked before as to the consequences for the discontinuity in $\phi^r(E')$, we fail to give a definite answer. The bump in $\rho(E')$ is not specific enough for translating it into an isolated singularity. Besides, pole singularities that migh occur in the electron-hydrogen case can be expected to smear out for helium. This is due to the integration over an additional electronic coordinate (as can readily be seen in the first Born approximation). More sight on progress can be expected if one is able to interpret the behaviour of $\rho(E')$, which is only defined for negative values in its variable, as a reflection of processes occurring at physical (i.e. positive) energies. This is subject to current research [Tip, private communication].

The problems and pitfalls one encounters in attempts to localize singularities can best be illustrated by what other groups have achieved in their analysis of the, in principle simpler, $\phi^r(z)$ for atomic hydrogen. Blum and Burke [28] found that in the static exchange approximation $f^r(E)$ possesses a third-order pole at $E = -\frac{1}{2}$, i.e. at the ionization energy. Tip [5] showed that, just as with helium, $\phi^r(z)$ is analytic in the interval stretching from the left semi-axis cut at $E = -\frac{1}{2}$ up to zero (see figure 1). On the contrary, Gerjuoy and Lee [29] argued that in $\phi^r(E)$ singularities occur at $E_n = -\frac{1}{2}\, n^2$ and that the singularity at $E = -\frac{1}{2}$ is not a third-order pole but merely logarithmic. Byron and Joachain [30] analysed the singularities of the second Born approximation to the exchange amplitude f^r_{B2}. They showed that it has poles of order (n-1) at $E_n = -\frac{1}{2}\, n^2$, $n > 2$, which are associated with the excited intermediate states of the target. Thereupon they gave a non-rigorous argument suggesting that the bound-state singularities are most likely cancelled by singularities coming from the continuum intermediate states, leaving only a singularity at $E=-\frac{1}{2}$. Amusya and Kuchiev [31] confirmed Tip's findings that the exchange amplitude has a cut at the left semi-axis of the complex energy plane; the branch point at $E=-\frac{1}{2}$ is logarithmic. No additional singularities were found. Recently, Dumbrajs and Martinis [9] explored the singularity structure of $f^r_{B2}(z)$ on the basis of the so-called Landau rules [32]. They found that part of $f^r_{B2}(z)$ has a third-order pole at $E=-\frac{1}{2}$ as its 'leading' singularity and a cut starting at the same point. As such, this result does not contradict Tip's conclusions. However, a closer inspection of their computations shows that this singularity is cancelled by the remaining part of the second Born amplitude. Besides, it cannot be excluded that singularities at $E=-\frac{1}{2}$ arise from higher Born terms too. Thus the conclusions Dumbrajs and Martinis [9] draw from their study for the shape of $\Delta(E)$ are at the least premature.

5. Conclusions

The preceding analysis leaves no opportunity to escape from the rather negative conclusion that dispersion relations do not work for electron-atom scattering. Appropriate as they may be in fields where causality is explicitly built into the formalism, such as scattering of light and relativistic quantum dynamics, it is just the time-independent Schrödinger equation which prevents a clear causal description.

Thus, the analytic properties of the amplitude must be investigated from the theory itself instead of being derived from causality. For the direct part of the amplitude these could be firmly established. Consequently, positron-atom scattering can be caught in a simple dispersion relation. However, it is the exchange part which complicates matters seriously. Given the fact, that the various theoretical groups already disagree on its singularity structure for the simplest system of electron-hydrogen, it is rather doubtful that in the near future a consistent interpretation will be given for the present results on helium.

More sight on progress can be expected when the present experimental analysis is extended to atomic hydrogen. Although feasible with our equipment, it might be very difficult to obtain data with comparable accuracy as with helium.

Another drawback is that forward dispersion relations - just because of their general nature - do not make an appropriate tool for clearing up the mechanisms behind a specific physical effect. This is best illustrated with what happened when we inverted the discrepancy function: the first peaked structure is blown up to a large bump, which rather obscures the picture than clarifies it.

To close this discussion, we may state that the present analysis unmasks the limited usefulness of dispersion relations for experiments with electron-atom collisions. It does reveal exchange as one of the responsible processes for the observed structure in the cross section of helium for forward elastic scattering, but leaves the questions on the physical details unanswered. Only at those high impact energies where the exchange part is negligibly small, dispersion relations may be of value for constructing accurate zero angle differential cross sections.

References

[1] Gerjuoy E and Krall N A, Phys.Rev. 127, 2105 (1962).

[2] de Heer F J, Wagenaar R W, Blaauw H J and Tip A, J.Phys. B9, L269 (1976).

[3] de Heer F J, McDowell M R C and Wagenaar R W, J.Phys. B10, 1945 (1977).

[4] Blaauw H J, On the forward dispersion relation for electron-atom scattering (thesis), Amsterdam (1979).

[5] Tip A, J.Phys. B10, L11 and L295 (1977).

[6] Combes J M and Tip A, Ann.Inst.Henri Poincare, to be published (1983).

[7] Phillips D L, J.of A.C.M. 9, 84 (1962).

[8] Wagenaar R W and Ter Riele J, Comp.Phys.Comm., to be published (1983).

[9] Dumbrajs O and Martinis M, J.Phys. B15, 961 (1982).

[10] Combes J M and Thomas L, Comm.Math.Phys. 34, 251 (1973).

[11] Blaauw H J, Wagenaar R W, Barends D H and de Heer F J, J.Phys. B13, 359 (1980).

[12] Kennerly R E and Bonham R A, Phys.Rev. A17, 844 (1978).

[13] Inokuti M and McDowell M R C, J.Phys. B7, 2382 (1974).

[14] Kim Y K and Inokuti M, Phys.Rev. A3, 665 (1971).

[15] Andrick D and Bitsch A, J.Phys. B8, 393 (1975).

[16] McConkey J W and Preston J, J.Phys. B8, 63 (1975).

[17] Register D F, Trajmar S and Srivastava S K, Phys.Rev. A21, 1134 (1980).

[18] Nesbet R K, Phys.Rev. A20, 58 (1979).

[19] Leonard P J and Barker J A, in Theoretical Chemistry, Advances and Perspectives, ed. H. Eyring and D. Henderson, Academic Press, N.Y. (1975) vol.I, p.117.

[20] Thompson D G, Proc.Roy.Soc.(London) A294, 160 (1966).

[21] Jansen R H J, de Heer F J, Luyken H J, van Wingerden B and Blaauw H J, J.Phys. B9, 185 (1976).

[22] Bromberg J P, J.Chem.Phys. 61, 963 (1974).

[23] Byron F W and Joachain C J, FOM Report no. 37521 (1975) and private communication.

[24] Pekeris C L, Phys.Rev. A115, 1216 (1959).

[25] Kim Y K and Inokuti M, Phys.Rev. 165, 39 (1968).

[26] Bransden B H and McDowell M R C, J.Phys. B3, 29 (1970).

[27] Hutt P K, Islam M M, Rabheru A and McDowell M R C, J.Phys. B9, 2447 (1976).

[28] Blum K and Burke P G, Phys.Rev. A16, 163 (1977).

[29] Gerjuoy E and Lee C M, J.Phys. B11, 1137 (1978).

[30] Byron F W and Joachain C J, Phys.Rev.Lett. 35, 1147 (1975).

[31] Amusya M and Kuchiev M Yu, Sov.Phys.-JETP 47, 484 (1978).

[32] Landau L D, Nucl.Phys. 13, 181 (1959).

Summary

This thesis describes a detailed experimental study in the field of electron atom collisions. Its main subject of investigation concerned the measurement of small angle elastic scattering. At high impact energies, i.e. at least an order of magnitude larger than the orbital velocities of the outer atomic electrons, the cross sections for this process can be calculated accurately. At lower velocities however, a strong 'competition' takes place between the two possible processes, viz. elastic and inelastic scattering. Therefore, couplings between the elastic and all open inelastic channels have to be calculated explicitly, which is an extremely hard task. Besides, exchange coupling becomes important then. This is the mechanism where projectile and atomic electrons change roles due to their indistinguishability. At still lower energies, i.e. below the first inelastic threshold, the theoretical description becomes simpler again.

Chapter I describes how we gained interest in just this particular collision process as a result of a study on the validity of dispersion relations for electron-atom scattering. These relations are easily derived for processes, which obey a simple causality condition. In case of electron scattering the dispersion relation couples the differential elastic cross section at angle zero to the total cross section. However, the exchange mechanism escapes a simple causal description. As such, preliminary research pointed out that exchange does not obey a dispersion relation equal to that for scattering of light. To determine this discrepancy quantitatively, accurate values for both total and differential cross sections are indispensable, in particular at the intermediate energies.

Chapter II describes the equipment and experimental procedure as applied for the total cross section measurements between 20 and 800 eV. A short, in length adjustable collision cell allowed target gas densities, high enough for accurate pressure recordings. In this way, earlier results obtained for argon, krypton and xenon could be improved. Besides, with this cell a thorough test could be carried out on the 'effective' target gas pressure. First at lengths shorter than twice

the diameter of the entrance aperture, a significant pressure drop was observed, in contrast to what a computer model for effusive molecular flow predicted. This information is essential for obtaining absolute differential cross sections, where, on behalf of a high angular resolution, a short interaction length was used.

The apparatus built for the small angle scattering measurements forms the subject of Chapter III. A novel design of a parallel plate analyser is thereby treated in detail. Key characteristics are its curved entrance and exit slit, which make the electron energy dispersion independent of the particular scattering angle. Herewith the analyser is also suited for doubly, i.e. scattering angle and energy loss, differential cross section measurements. Channelplates behind the exit slit enable a simultaneous particle detection over a range of 10° around the primary beam axis. The chapter closes with a discussion of the optical properties of a set of spherically shaped electrodes, by which the electrons can be retarded before entering the analyser. With this extension the energy resolution of the analyser can be enhanced up to a factor five, without serious distortion of the scattering pattern.

In chapter IV the measured elastic cross sections from the noble gases at energies between 20 and 100 eV are interpreted. An accuracy of 8% could be obtained down to a minimum angle of 1°. First the various approximations inherent to the existing theoretical models are critically examined with respect to their reliability at intermediate energies. Then, with these notes in mind, our results are analysed. The best agreement was found with the R-matrix calculations of Fon et al., although their data for helium and neon are systematically lower with increasing energy. It shows the inadequacy of using only one pseudo-state to allow for polarization and absorption.

The measurements displayed a broad cusp-like structure in the cross section for helium around the threshold for single ionization, which none of the existing theories has predicted sofar. The structure most probably reflects the accumulation of cusps, which occur at the successive thresholds for excitation of high Rydberg states and the continuum. Given the (yet) speculative character of this interpretation, the need for complementary research with high energy resolution is stressed.

Finally, in Chapter V, the dispersion relation for helium is tested. As expected, the discrepancy function, as it reflects the exchange part of the interaction, possesses non-zero values at energies below 200 eV. The reappearance of structure, as observed in the elastic cross section, indicates an enhancement of exchange when the ionization channel is opened. On the other hand, theory is not (yet) able to relate this function nor its inverse to specific properties of the exchange amplitude. Given the problems, which already persist in a likewise analysis for atomic hydrogen, as it is the simplest system, one may seriously doubt whether dispersion relations will ever be formulated correctly for many-electron systems.

Samenvatting

Dit proefschrift beschrijft zeer gedetailleerd een experimentele studie in de atoomfysica, en wel op het gebied van de elektron-atoom verstrooiing. Het onderzoek spitst zich toe op het bepalen van de kans van optreden van die botsingen, welke resulteren in slechts een kleine afbuiging van de baan van het projektiel elektron, zonder dat het daarbij een deel van zijn bewegingsenergie afstaat aan het getroffen atoom.

Een dergelijke 'zachte' elastische botsing moet men zich voorstellen als een aftasten van de periferie van het atoom door het elektron tijdens zijn passage. De elektronenwolk van het atoom raakt daarbij 'virtueel' aangeslagen, hetgeen zich uit als een geïnduceerd polarisatie-veld. Dit veld oefent op zijn beurt een, zij het zwakke, kracht uit op het projektiel elektron, dat onder invloed hiervan wordt verstrooid.

Bij hoge botsingssnelheden, dat wil zeggen tenminste een orde groter dan de baansnelheid van de atoom-elektronen, zijn de werkzame doorsneden voor dit proces nauwkeurig uit te rekenen. Bij lagere snelheden evenwel treedt een sterke 'competitie' op tussen de twee mogelijke processen, te weten elastische en inelastische verstrooiing. Voor een korrekte berekening van de verstrooiingskans moeten derhalve koppelingen tussen het elastische en de open inelastische kanalen in enigerlei vorm meegenomen worden, hetgeen een uitermate lastige opgave is. Bovendien wordt daar 'uitwisselings' koppeling belangrijk, een mechanisme waarbij projektiel en atoom-elektronen van rol verwisselen. Bij nog lagere botsingsenergieën, te weten beneden de drempel voor inelastische verstrooiing, is de theoretische beschrijving echter weer eenvoudiger geworden.

In het inleidende Hoofdstuk I staat beschreven hoe onze interesse in juist dit speciale botsingsproces werd gewekt tijdens een studie naar de geldigheid van dispersie-relaties voor elektron-atoom verstrooiing. Deze relaties spelen een rol bij die fysische processen, welke strikt causaal beschreven kunnen worden. Hun naam ontlenen zij aan verstrooiing van licht aan een dispersief medium. In het geval van elektron-atoom verstrooiing koppelt de voorwaartse dispersie-relatie de differentiële elastische doorsnede bij hoek nul aan de

totale doorsnede. Evenwel, het bij dit botsingsproces mede optredende 'uitwisselings' mechanisme laat zich niet in een eenvoudig causaal beeld vertalen. Voorlopig onderzoek wees dan ook uit, dat deze 'exchange' niet aan een dispersie-relatie voldoet, zoals die voor lichtverstrooiing kon worden afgeleid. Om deze diskrepantie kwantitatief te bepalen zijn nauwkeurige waarden voor zowel de totale doorsnede als voor de elastische differentiële doorsnede bij zo klein mogelijke hoek onontbeerlijk, in het bijzonder bij intermediaire botsingsenergieën.

In hoofdstuk II is beschreven op welke wijze totale doorsneden zijn gemeten voor energieën tussen 20 en 800 eV. Het bleek dat vroegere meetresultaten voor argon, krypton en xenon een nadere korrektie behoefden, vanwege een onjuiste drukbepaling. Deze trad aan het licht door gebruik te maken van een korte, in lengte instelbare botsingskamer. Hiermee was het geoorloofd om met hogere - en dus nauwkeuriger te bepalen - dichtheden van het botsingsgas te werken. Tevens is, door deze lengte te variëren, een grondige test uitgevoerd naar de 'effektieve' gasdruk. Eerst bij lengtes korter dan tweemaal de diameter van het intree-diafragma, trad een signifikante drukvermindering op, in afwijking van wat een komputermodel voor molekulaire effusie voorspelde. Deze informatie is van groot belang voor het absoluut maken van de differentiële doorsnede metingen, waar, ter wille van een hoog hoekoplossend vermogen, een korte botsingslengte is toegepast.

Hoofdstuk III beschrijft de opstelling voor de kleine hoekverstrooiingsmetingen. In detail worden de principes van een speciaal hiervoor ontwikkelde parallelle plaat analysator behandeld. Het bijzondere aan deze analysator zijn de gekromde in- en uitgangsspleten; met deze vorm wordt bewerkstelligd dat de elektronen, ongeacht hun strooihoek, tussen de platen parabolische banen doorlopen, die in lengte slechts afhangen van de energie van het elektron. Deze eigenschap maakt de analysator ook geschikt voor tweevoudig, dat wil zeggen zowel naar hoek als energie, differentiële doorsnede metingen. Met mikro-kanaalplaten over de uitgangsspleet is simultane detektie mogelijk over een hoekbereik van 10° rond de primaire bundelas. Dit hoofdstuk eindigt met een beschouwing gewijd aan een stelsel spheries gekromde electroden, geplaatst voor de ingangsspleet van de analysator. Door de elektronen eerst te vertragen in dit bolsymmetrische veld, wordt een hoger energie-oplossend vermogen bewerkstelligd.

Hoofdstuk IV behandelt de meetresultaten voor elastische verstrooiing aan de edelgassen bij botsingsenergieën tussen 20 en 100 eV. Een nauwkeurigheid van 8% kon gerealiseerd worden tot een minimum verstrooiingshoek van 1°. Om tot een zinvolle vergelijking met de theorie te komen, worden de diverse benaderingen, welke de bestaande theoretische modellen toepassen, eerst kritisch doorgelicht op hun mogelijke tekortkomingen in dit intermediaire energie-gebied. De beste overeenstemming werd gevonden met de R-matrix berekeningen van Fon, al vallen deze voor helium en neon bij toenemende botsingsenergie systematisch lager uit. Aangetoond wordt dat de door hem gebruikte 'pseudo-toestand' geen juiste beschrijving geeft voor de polarisatie en absorptie in deze gassen.

De metingen gaven een struktuur te zien in de elastische doorsnede van helium rond de drempelenergie voor enkelvoudige ionisatie, hetgeen door geen van de bestaande theorieën werd voorspeld. Zijn typische vorm en lokatie op de energie-as duidt op een cumulatief effect van 'cusps'. Deze storingen in het elastische botsingsproces treden op zodra een nieuw kanaal opengaat, waarlangs een deel van de inkomende flux kan wegstromen. Gezien het vooralsnog speculatieve karakter van deze interpretatie, worden suggesties aangedragen voor aanvullende metingen met hoger energie-oplossend vermogen.

In hoofdstuk V tenslotte worden de helium resultaten aangewend voor het testen van de dispersie-relatie. Hiermede kan de diskrepantie funktie, welke geheel voor rekening van exchange komt, bepaald worden; eerst boven 200 eV valt deze te verwaarlozen. Het feit dat ook hier weer struktuur gevonden wordt rond de ionisatie energie, duidt op een verhoogde kans op uitwisseling in dat gebied tussen het inkomende elektron en de atoom-elektronen. De theorie is evenwel (nog) niet in staat de aldus gevonden funktie noch zijn inverse eenduidig te relateren aan specifieke uitwisselingsprocessen. Gezien de problemen, welke zich wat dit betreft reeds voordoen bij het eenvoudigste systeem van atomair waterstof, valt het ernstig te betwijfelen of dispersie-relaties ooit korrekt geformuleerd zullen worden voor veel-elektron systemen.

STELLINGEN

behorende bij het proefschrift

SMALL ANGLE ELASTIC SCATTERING
OF ELECTRONS BY NOBLE GAS ATOMS

RENÉ W. WAGENAAR

Amsterdam, 15 februari 1984.

1

De konklusie van Dumbrajs en Martinis betreffende de analytiese struktuur van de voorwaartse elastiese uitwisselings-amplitude voor elektron-waterstof verstrooiing volgt niet uit de door deze auteurs naar voren gebrachte argumenten. Dit geldt reeds voor de tweede Born bijdrage tot deze amplitude.

O. Dumbrajs en M.Martinis, J.Phys.B:Atom. Molec. Phys. 15, 961 (1982).
Dit proefschrift, Hoofdstuk V.

2

De suggestie van Ebata et al., dat de $B^2\Pi, v=31$ toestand verantwoordelijk is voor de versterking van rotatielijnen in het 4-foton ionisatie-experiment van NO via de $A^2\Sigma, v=1$ toestand, is onjuist gezien de informatie verkregen uit het opmeten van de energie-verdeling van de hierbij vrijkomende elektronen.

D.Ebata, N.Mikami en M.Ito, J.Chem.Phys. 78, 1132 (1983).
J.Kimman, P.Kruit en M.J.van der Wiel, Chem. Phys. Lett. 88, 576 (1982).

3

Aangezien plasma-etsen van silicium hoofdzakelijk een verstuivingsproces blijkt te zijn, zal de door ionen-bombardement veroorzaakte schade de bruikbaarheid van deze techniek begrenzen. Het verdient daarom aanbeveling om 'zachtere' etsprocessen onder invloed van foton- of elektronenbombardement nader te onderzoeken.

R.A.Haring, A.Haring, F.W.Saris en A.E. de Vries, App.Phys. Lett. 41 (2), 174 (1982).
R.A.Haring, A.W. Kolfschoten en A.E. de Vries, presented at the 10th Int. Conf. Atomic Collisions in Solids, Bad Iburg (1983) and submitted for publication in the J.Appl.Phys.

4

Het feit dat Fon et al. met hun 'close-coupling' berekening geen aanwijzing vinden voor struktuur in de differentiële werkzame doorsnede voor elastiese verstrooiing van elektronen aan helium, is een rechtstreeks gevolg van het meenemen van slechts één pseudo-toestand voor het verdisconteren van zowel absorbtie als polarisatie-effecten.

W.C. Fon, K.A. Berrington en A. Hibbert, J.Phys. B: Atom. Molec.Phys. 14, 307 (1981).
Dit proefschrift, Hoofdstuk IV.

5

De argumenten welke Olson gebruikt om de ℓ-distributie in A^{q+}-H elektronvangst-processen te verklaren, zijn onvolledig, daar de invloed van de snelheid van het projectiel-ion buiten beschouwing gelaten wordt.

R.E.Olson, Phys.Rev. A 24, 1726 (1981).
V.A.Abramov, F.F. Baryshnikov en V.S. Lisitsa, JETP Lett. 27, 464 (1978).
Yu.S. Gordeev, D.Dijkkamp, A.C. Drentje en F.J.de Heer, Phys. Rev. Lett. 50, 1842 (1983).

6

Uit konsekwente toepassing van het Arrheniusmodel op de resultaten van Williams et al. volgt dat suiker bij kamertemperatuur in ongeveer 100 sekonden uiteen zal vallen.

B.W.Williams, A.P. Irse, H.Zmoza en R.J.Beuhler, J.Phys. Chem. 87, 2185 (1983).

7

De kans dat een polynoom in één variabele met gehele getallen als koëfficiënten, de eigenschap heeft dat de grootste gemene deler van zijn koëfficiënten groter is dan 1, is nul. De kans dat van zo'n polynoom alle waarden aangenomen in de gehele getallen, een grootste gemene deler groter dan 1 hebben, is evenwel ongeveer 28 procent.

8

Het wel en wee van het onderzoek aangaande de Einstein-Podolsky-Rosen paradox illustreert treffend, hoezeer de gedachtenvorming kan worden gehinderd door een onkrities hanteren van het begrip "ding" dan wel "lichaam", dat voortvloeit uit het te overheersende beeld van een natuurwetenschap-die-op-zoek-is-naar-de-bouwstenen-van-het-heelal.

A.Einstein, B.Podolsky en N.Rosen, Phys.Rev. 47, 777 (1935).
B.Hiley, New Scientist, 746 (1980).
B. d'Espagnat, Scientific American 241, nr. 5, 128 (1979).

9

Tegen het licht van de door de regering en parlement geclaimde zorgvuldigheid bij het nemen van beslissingen, welke grote sociale gevolgen in zich dragen, getuigt de keuze om energie-opwekking wèl, doch het krachtig stimuleren van de informatika-sektor nièt tot inzet van een Brede Maatschappelijke Diskussie te maken, van inkonsekwent beleid.

10

Sinds G.A.Bredero in 1617 in zijn boek "de Spaanse Brabander" Jerolimo Rodrigo over Amsterdam liet opmerken: "'t Is wel een schone stad, maar 't volksken is te vies", is er weinig veranderd.